

Evaluation of High Frequency Vibrator Response

By

Copyright 2012

Craig M. Hendrix

Submitted to the graduate degree program in Geology
and the Faculty of the Graduate School of the University of Kansas
In partial fulfillment of the requirements for the degree of
Master of Science

Advisory Committee:

Richard D. Miller, Chairperson

Georgios P. Tsoflias

J. Douglas Walker

Date Defended: May 4th, 2012

The Thesis Committee for Craig M. Hendrix certifies
That this is the approved Version of the following thesis:

Evaluation of High Frequency Vibrator Response

Advisory Committee:

Richard D. Miller, Chairperson

Georgios P. Tsoflis

J. Douglas Walker

Date Approved: May 11th, 2012

Abstract

Accurate analysis of the motion of a commercial high frequency hydraulic vibrator commonly used for near-surface applications demonstrated that the rigid body assumption of the weighted-sum approximation is not valid throughout the vibrator's operational frequencies. This study reveals significant response variability across the baseplate, which is dependent on accelerometer position with respect to radial location and internal baseplate structure. Consequently, the baseplate cannot be considered a point source of propagation, which complicates optimizing source operations to increase data fidelity. In an effort to optimize the source signature approximation to increase data fidelity, simultaneous acquisition of baseplate acceleration and pressure beneath the baseplate provided a means to directly compare the response of strategically placed accelerometers to the true ground force. This study concludes that the most representative approximation occurs when multiple accelerometers are positioned on the baseplate to average the baseplate motion. In addition, this study found that the IVI Minivib I is incapable of providing measurable seismic energy at frequencies over 200 Hz due to opposing baseplate and reaction mass phase. Based on this observation, it is clear the design of the baseplate needs to be modified by adding extra weight and rigidity to the driven structure. Increasing rigidity of the baseplate will reduce source generated harmonic distortion caused by baseplate flexure resulting in a more uniform response across the baseplate and a more accurate ground force approximation. Additionally, the opposing phase relationship between the baseplate and the reaction mass could be remediated by increasing the baseplate weight resulting in an increase in energy above 200 Hz.

Table of Contents

Title Page.....	i
Acceptance Page	ii
Abstract.....	iii
Table of Contents	iv
List of Figures	vi
List of Tables	viii
Acknowledgments	ix
1. Introduction	1
2. Background.....	4
2.1. Convolutional Model	4
2.2. Cross- Correlation vs. Deconvolution.....	5
2.3. Approximating Source Signatures	6
2.3.1. Weighted-sum Approximation	8
2.3.2. Limitations of the Weighted-sum Approximation for High Frequency Vibroseis	9
2.3.3. Flexural Rigidity Method	11
2.3.4. Limitations of the Flexural Rigidity Method.....	15
2.3.5. High Fidelity Vibroseis Seismic (HFVS) Method.....	16
2.3.6. Limitations of HFVS Method.....	17
3. Problem Statement	19
4. Equipment Setup	21
5. Methods: Part 1; Investigation of Baseplate Motion.....	25
5.1. Purpose Statement	25
5.2. Geologic Setting and Data Acquisition.....	26
5.2.1. Geologic Setting	27
5.2.2. Data Acquisition	29
5.3. Data Analysis	32
5.3.1. Comparison of Endevo Accelerometers and CRL Accelerometers	32
5.3.2. Sweep Repeatability.....	38
5.3.3. Response Variation due to Radial Position and Position with Respect to Baseplate Structure	39
5.3.4. Investigation of Baseplate Symmetry	45
5.3.5. Differences in Response Associated with Source Location	50
6. Discussion: Part 1; Investigation of Baseplate Motion	53
7. Conclusions: Part 1; Investigation of Baseplate Motion	58
8. Methods: Part 2; Optimizing Ground Force Approximation	60
8.1. Purpose Statement	60

8.2. Data Acquisition.....	60
8.3. Data Analysis	65
8.3.1. Sweep Repeatability.....	66
8.3.2. Evaluation of the Feedback Signal	67
8.3.3. Determination of Optimal Accelerometer Model	71
8.3.4. Optimal Accelerometer Baseplate Combination	74
9. Discussion: Part 2; Optimizing Ground Force Approximation.....	80
10. Conclusions: Part 2; Optimizing Ground Force Approximation	85
11. Final Conclusions.....	88
References.....	90
Appendix A.....	95
Appendix B	96
Appendix C	103

List of Figures

Figure 2.1. Mechanical model of hydraulic vibrator actuator	9
Figure 2.2. Mechanical ground impedance model.	9
Figure 4.1. Equipment configuration for recording CRL 966 accelerometers	22
Figure 4.2. Reaction mass accelerometer locations for all three accelerometer models.	23
Figure 4.3. Image of load cell plate.	24
Figure 5.1. Diagram of IVI Minivib I baseplate structure.	26
Figure 5.2. Generalized stratigraphy of Douglas Group	27
Figure 5.3. Map of source locations for Part 1 of survey	28
Figure 5.4. Location of reaction mass accelerometer.	30
Figure 5.5. Diagram of radial positions tested to evaluate baseplate symmetry	31
Figure 5.6. Image of accelerometer locations tested for response variability associated with baseplate structure.	33
Figure 5.7. Signal comparison of a) baseplate and b) reaction mass signals from the CRL 966 accelerometer and the Endevco 7703A-1100 accelerometer.	35
Figure 5.8. Difference of Endevco and CRL accelerometer correlation phase spectrum	35
Figure 5.9. Amplitude ratio of Endevco baseplate and reaction mass accelerometers with respect to corresponding CRL accelerometers.	36
Figure 5.10. Reaction mass and baseplate amplitude spectra comparison between Endevco and CRL accelerometers.	37
Figure 5.11. Signal plot of computed Endevco and CRL ground force	38
Figure 5.12. Absolute peak ground force of Endevco and CRL signals	38
Figure 5.13. Seismic display of source repeatability	39
Figure 5.14. Correlation of signals from varying radial position	41
Figure 5.15. Correlation phase plot of three off rib radial positions	42
Figure 5.16. Amplitude ratio of three radial positions with respect to radial position 1 located off reinforcing rib	42
Figure 5.17. Correlation of on and off rib accelerometers at each of the three radial positions for each source location in experiment 1	43
Figure 5.18. Phase difference between on and off rib accelerometers.	44
Figure 5.19. Amplitude difference between on and off rib accelerometers displayed in dB.	45
Figure 5.20. a) Mean and b) standard deviation of correlation coefficients between four quadrants for on rib accelerometer positions 1. c) Mean and d) standard deviation of correlation coefficients between four quadrants for off rib accelerometer positions	47
Figure 5.21. Mean correlation across baseplate for each of the three source locations	48
Figure 5.22. Comparison of quadrant response variability to source variability	48
Figure 5.23. Phase spectra of quadrant 3 correlated with quadrant 1 for each radial position located on rib at source location 1.	50
Figure 5.24. Amplitude spectrum difference plot of quadrant 3 from amplitude spectrum of quadrant 1 for each radial position located on rib at source location 1	50

Figure 5.25. Absolute peak force comparison of three source locations	51
Figure 5.26. Correlation phase between CRL reaction mass and baseplate signals for each source location	52
Figure 8.1. Source location for Part 2	61
Figure 8.2. Schematic of 8 different accelerometer positions tested for Part 2	62
Figure 8.3. Location of load cells beneath the baseplate.....	64
Figure 8.4. Unshifted accelerometer signals.....	66
Figure 8.5. a) Amplitude spectrum of Dytran ground force signal with amplifier noise circled in red. b) 5-10 Hz Low-cut filtered amplitude spectrum of Dytran ground force	67
Figure 8.6. Phase spectra of the Dytran and CRL ground force correlated with the true ground force.....	69
Figure 8.7. Amplitude difference between calculated Dytran and CRL ground force and the true ground force.....	70
Figure 8.8. Absolute peak force comparison of the Dytran and CRL ground force to the true ground force.....	70
Figure 8.9. Phase spectra of the Endevco and CRL ground force correlated with the true ground force.....	72
Figure 8.10. Amplitude difference between calculated Endevco and CRL ground force from the true ground force	73
Figure 8.11. Absolute peak force comparison of the Endevco and CRL ground force to the true ground.....	73
Figure 8.12. Mean correlation of ground force approximation calculated by a) using a single baseplate accelerometer and b) using a combination of four accelerometers located on the baseplate to their respective true ground force calculated by the Load Cell System	75
Figure 8.13. Phase spectra of the most representative ground force approximation and least representative ground force approximation using one CRL baseplate accelerometer correlated with respect to their respective true ground force.....	76
Figure 8.14. Amplitude spectra of the most representative ground force approximation and least representative ground force approximation using one CRL baseplate accelerometer with respect to the true ground force	77
Figure 8.15. Phase spectra of the most representative ground force approximation and least representative ground force approximation using four CRL baseplate accelerometers correlated with the true ground force.	77
Figure 8.16. Amplitude spectra of the most representative ground force approximation and least representative ground force approximation using four CRL baseplate accelerometers with respect to the true ground force	78
Figure 8.17. Absolute peak force comparison of the most and least representative ground force calculated using one CRL baseplate accelerometer to their respective true ground force.....	78
Figure 8.18. Absolute peak force comparison of the most and least representative ground force calculated using four CRL baseplate accelerometers to their respective true ground force	79

List of Tables

Table 5.1. Survey parameters for each experiment	30
Table 5.2. Correlation between Endevco ground force and CRL ground force signal for each source location.	37
Table 5.3. Mean and standard deviation of the correlation coefficients between the CRL reaction mass accelerometer signal and the synthetic sweep for each source location	39
Table 5.4. Correlation of stacked reaction mass signals of consecutive five sweeps for each source location	40
Table 8.1. Accelerometer location combinations using 4 baseplate accelerometers with each accelerometer's corresponding welded positions	63

Acknowledgments

First and foremost I would like to thank my advisor, Dr. Rick Miller, for all his help, guidance, and financial support throughout my graduate work. His immeasurable work ethic and knowledge in near surface geophysics has been an inspiration throughout my research. I would also like to thank my committee members, Dr. George Tsoflias and Dr. Doug Walker, for providing incredible guidance and insight while completing my research.

I would also like to acknowledge the effort and hard work of the Exploration Services staff at the KGS. Without the selfless and patient assistance of Shelby Peterie, Brett Bennett, and Brett Wedel during data acquisition, data analysis, and thesis revision, this project would not have been completed. Also, I thank John Sallas, John Wei, and the staff of Seismic Source Company, especially Vitaly Shevkunov, for their technical support during my research. Additionally, I am extremely grateful for my classmates for their friendship and help throughout the completion of my thesis.

Most of all, I am extremely grateful to have such a supportive group of family and friends, who have encouraged me through the toughest of times. Specifically, I would like to thank my Mom and Dad, Maria and Randall Hendrix, my brother, Ross Hendrix, and my loving girlfriend, Kim Fisher, whom I am forever grateful for. Lastly, the companionship of our dogs, Archie, Mia, and Cadence, helped me maintain a healthy perspective on life. I love you all, thanks for all support and added motivation.

1. Introduction

Since the unveiling of the vibroseis system (Crawford et al., 1960), the seismic vibrator has become the primary land seismic source for exploration applications (Baeten and Ziolkowski, 1990; Anstey, 1991). Recently, the use of hydraulic vibratory sources for near-surface application has increased because of its ability to expand resolution with minimal environmental impact (Miller et al., 2004; Pugin et al., 2009). Ideally, a controlled, broadband wavelet that is repeatable from shotpoint to shotpoint is produced using the vibroseis system (Chapman et al., 1981). If the source signature (vibrator output) is known, the technique has the capability to optimize resolution of the seismic waveform.

The source signature, however, is difficult to obtain due to nonlinear complexities introduced within the vibrator mechanical system and from the nonlinear ground response to the vibrator output. The nonlinear complexities within the vibroseis system have been observed, discussed, and theorized for petroleum applications with conventional vibrators (Sallas and Weber, 1982; Baeten and Ziolkowski, 1990; Walker, 1995; Lebedev and Beresnev, 2004). In contrast, there is less concern for fully optimizing source operations for near-surface applications. As a result, little research has been focused on nonlinearity within the vibroseis system for near-surface applications (Miller et al., 2009).

Analysis of the vibrator-earth response manifests two main complexities within the vibroseis system. First, nonlinear complexities within the vibrator's hydraulic system, baseplate flexure, and the ground response to force exerted by the vibrator baseplate generate harmonic distortion (Schrodt, 1987; Baeten and Ziolkowski, 1990; Wei, 2008a). The harmonic distortion creates correlated noise (harmonic ghosts) that is difficult to suppress during processing (Seriff and Kim, 1970; Li et al., 1995). Using an accurate measure of the source signal, deconvolution

will suppress harmonic distortion within data (van der Veen et al., 1999). Second, the determination of the source signal is non-trivial since the force is not distributed uniformly beneath the baseplate due to complex ground-baseplate coupling and nonlinearities introduced in the system from the ground's response to force exerted by the vibrator baseplate. The ground force, consequently, varies not only from groundpoint to groundpoint but also from sweep to sweep (Baeten, 1989; Ziolkowski, 2010).

Theoretically, cross-correlation with a synthetic (drive) sweep will ideally collapse the vibrogram to the reflectivity sequence convolved with a band-limited zero-phase Klauder wavelet. The synthetic sweep is the ideal sweep (drive signal) that represents the parameters designed to best meet the survey needs and is theoretically the same vector exerted upon the Earth's surface by the vibrator when delivering the sweep. The actual seismic signal (true ground force) delivered in the ground and propagated through the ground is not equal to the ideal sweep. The true ground force can be calculated by integrating the measured pressure function beneath the vibroseis baseplate (Mewhort et al., 2002):

$$T_{GF} = \int_A P(x, y) dx dy \quad (1)$$

where T_{GF} is the true ground force, $P(x, y)$ is the measured pressure function beneath the vibroseis baseplate, and A is the area of the baseplate. This approach is impractical for production surveys, however, because of the cost of the technology and the significant amount of time required to calibrate pressure sensors (Wei et al., 2010; Ziolkowski, 2010). The far-field particle velocity source response is equal to the time derivative of the true ground force (Aki and Richards, 1980). Although this has been proven, ground force is most commonly used as a feedback signal for correlation.

It is well-known that deconvolution with the true source signature produces a far more representative seismic image than the cross-correlation with the ideal sweep (Ghose, 2002). An estimation of the true ground force is, therefore, used to deconvolve the data. Traditionally, the weighted-sum approximation of ground force proposed by Sallas (1984) is a widely accepted approach. The weighted-sum approximation assumes that the baseplate and ground are perfectly coupled and the vibrator baseplate acts as a rigid body. As the drive frequency of the vibrator increases, the rigid body assumption is generally violated (Sallas et al., 1985; Baeten and Ziolkowski, 1990). Consequently for high frequency data, the need for a more accurate representation of true ground force, which includes nonlinearities within the system, is necessary to remove nonlinear distortion within the correlated seismogram. Although impossible to obtain because infinite rigidity is unattainable, the ideal vibrator system for high frequency applications would be relatively lightweight, equipped with an infinitely rigid baseplate and capable of producing ultra-broadband energy.

Since the ground force approximation is used to produce the correlated seismogram, the accuracy of the ground force approximation will ultimately determine the fidelity of the data. An alternative approach first proposed by Allen et al. (1996) called the High Fidelity Vibroseis Seismic (HFVS) method is almost exclusively used for petroleum applications. This method employs inverse filtering by spectral division to eliminate the dependency between the fidelity of correlated seismic record and the accuracy of approximated source signature (Allen et al., 1996). Since the nonlinearity within the system increases with high frequency data (Lebedev and Beresnev, 2004; Sallas, 2010; Wei, 2010), the use of the HFVS method in near-surface applications could produce significant gains in data resolution.

2. Background

2.1. Convolutional Model

A seismic trace can be described by a simple, one dimensional, plane wave, linear convolutional model. The convolutional model is the fundamental basis for most seismic interpretation (Liner, 2004). It states that all seismic traces are the result of convolving the source wavelet, $w(t)$, with the earth's reflectivity sequence. Essentially, the earth acts as a complex filter on the seismic wavelet. The convolutional model can be described by the equation (Yilmaz, 2001):

$$x(t) = w(t) * e(t) + n(t) \quad (2)$$

where $x(t)$ is the seismic trace, $w(t)$ is the source wavelet, $*$ is the convolution operator, $e(t)$ is the earth reflectivity sequence and $n(t)$ is noise. In order to describe the seismic trace by the convolutional model, five assumptions must be made (Yilmaz, 2001):

1. the earth is made up of horizontal layers of constant velocity;
2. the source generates a compressional plane wave that impinges on layer boundaries at normal incidence;
3. the source waveform does not change as it travels through the subsurface (it is stationary);
4. the source waveform is known;
5. there is no a priori knowledge of noise; as a result, the noise component, $n(t)$, is assumed to be negligible;

From these assumptions, the convolution model equation can be reduced to (Yilmaz, 2001):

$$x(t) = w(t) * e(t) \quad (3)$$

This is the traditional model for describing a seismic trace. However, these assumptions are not all satisfied in reality, especially for high frequency seismic data. Consequently, increasing data resolution for near-surface applications can be extremely challenging.

2.2. Cross- Correlation vs. Deconvolution

Traditionally, two methods have been used the most to collapse the sweep to a source wavelet for vibroseis data. The first and most commonly used method involves cross-correlating the recorded signal with a synthetic vibroseis sweep (the ideal sweep) as defined by the sweep parameters defined in the survey. Since the recorded signal is the convolution of the earth reflectivity sequence with the sweep assuming a perfect transfer function (ideal case), cross-correlation using the ideal sweep will collapse the sweep to a band-limited zero-phase Klauder wavelet at impedance contrasts. The cross-correlation method can be expressed by (Yilmaz, 1987):

$$x_{cc}(t) = e(t) * s(t) \star s(t) = e(t) * k(t) \quad (4)$$

where $x_{cc}(t)$ is the recorded seismic trace, $e(t)$ is the earth reflectivity sequence, $s(t)$ is the sweep, $*$ is the convolution operator, \star is the cross-correlation operator, $k(t)$ is the Klauder wavelet, and all values are time dependent. This process acts as a filter for frequencies that are outside the bandwidth of the sweep (Brittle et al, 2001). Therefore, cross-correlation is desirable whenever there is a high level of noise outside the bandwidth of the sweep (Anstey, 1964). Since cross-correlation measures the similarity between two waveforms, it is extremely sensitive to phase variations between two waveforms (Yilmaz, 1987). Intrinsically, the ideal sweep does not equal the actual sweep. Therefore, cross-correlation does not yield optimum data.

Alternatively the second method, frequency domain vibroseis deconvolution is used to remove the seismic wavelet (time variable sweep) from the recorded signal. This process uses

the same convolution model as cross-correlation, but is performed in the frequency domain (Brittle et al., 2001). In the frequency domain, convolution is equal to multiplication. The equation can be written as:

$$X(f) = E(f)S(f) \quad (5)$$

where $X(f)$ is the recorded seismic trace, $E(f)$ is the reflectivity sequence (earth filter), and $S(f)$ is the sweep. Dividing through by the sweep gives:

$$E(f) = X(f) / S(f) \quad (6)$$

In the ideal noise free case with a well-known source wavelet, deconvolution will produce the earth reflectivity sequence (Brittle et al., 2001; Ghose, 2002). Vibroseis deconvolution is the optimal processing technique when the signal to noise ratio is high and the true energy can be measured. It will produce a superior image of the subsurface when compared to cross-correlation because the sweep is removed from the recorded signal leaving the earth reflectivity sequence. In theory, the optimal vibroseis source wavelet removal technique to optimize signal to noise ratio (i.e. resolution) is deconvolution of the recorded signal with the true ground force.

2.3. Approximating Source Signatures

Accurate approximation of the seismic source signature is pivotal in correlating high resolution vibroseis reflection data. When the source signature is known, the vibroseis technique has the ability to optimize the resolution of the seismic waveform (van der Veen et al., 1999). The source signature, however, is difficult to obtain due to nonlinear delivery of energy to the ground and ground response to the vibrator sweep. Accurate ground force approximation will result in significant gains in resolution compared to correlation with the synthetic. Ongoing research analyzing high frequency hydraulic vibrator-earth response in an effort to increase

fidelity of data attempts to address problems within the vibroseis system (Rademacker, 2006; Rice, 2009).

The vibroseis-earth interaction can be described by multiple models. Two different models describing the vibroseis-earth interaction based on the distributions of traction and displacement directly underneath the vibroseis baseplate are discussed. The distributions of traction and displacement are dependent on the elastic properties of the earth and the model of the seismic vibrator (Beaten, 1989). Two methods for approximating the true ground force derived from these models will, therefore, be examined: the weighted-sum approximation and the flexural rigidity approximation.

Both models assume that the ground and the baseplate are perfectly coupled throughout the duration of the sweep. In reality, the baseplate is not perfectly coupled to the ground; full decoupling of the baseplate-ground contact is controlled by the vibrator hold-down weight and drive energy (Wei et al., 2010). Although full decoupling is prevented with the hold-down weight, the hold-down force is not uniformly distributed across the baseplate. This results in partial decoupling, which occurs when the local dynamic force is greater than the local hold-down force (Wei et al., 2010). Also in reality, the ground medium is nonhomogeneous and nonlinear resulting in coupling issues across the baseplate (Sallas, 2010).

Contrary to vibroseis theory, both methods use the approximated ground force signal to deconvolve the raw seismogram. Miller and Pursey (1954) and Aki and Richards (1980) have shown that the P-wave far-field particle velocity source response is a time derivative of true ground force and therefore the time derivative of ground force should be used to deconvolve raw vibroseis data. Although this has been well established, the correlated seismogram for near-surface applications will only be as good as the source signature approximation. Consequently,

using the time derivative of a poor ground force approximation will not result in significant gains in resolution for near-surface applications. When using one vibrator, the far-field is much less than 100 m (Ziolkowski, 2010). Although this generalization may be true in most cases, variability in the near-surface material makes it difficult to generalize the depth at which the seismic waveform acts as a far-field signature. Thus for high frequency near-surface applications, using the time derivative of ground force for correlation rather than the ground force maybe site dependent.

2.3.1. Weighted-sum Approximation

The weighted-sum approximation proposed by Sallas (1984) was developed from a one-dimensional mechanical vibrator model (Figure 2.1) and is almost universally used as the feedback signal in the closed-looped vibroseis system. The weighted-sum approximation uses a baseplate model which assumes uniform displacement across the baseplate (the baseplate acts as a rigid body), and the bending forces of the baseplate are negligible (Saragiotis et al., 2010). This model does not account for the ground response (elasticity of the near-surface soil) directly below the baseplate related to the force exerted by the baseplate (Figure 2.2). In addition, this method also assumes that the far-field particle displacement is proportional to the ground force (Beaten, 1989).

Simplifying the equations of motion for the vibrator (Appendix A), the weighted-sum ground force approximation can be calculated by (Sallas, 1984):

$$-F_g = M_b \ddot{x}_b + M_r \ddot{x}_r \quad (7)$$

where F_g is ground force, M_b is the mass of the baseplate, \ddot{x}_b is the baseplate acceleration, M_r is the mass of the reaction mass, and \ddot{x}_r is the reaction mass acceleration. The accelerometer signals located on the baseplate, \ddot{x}_b , and on the reaction mass, \ddot{x}_r , are recorded during each vibroseis

sweep. Baseplate mass and the reaction mass are two known constants, which depend on the seismic vibrator used in the survey.

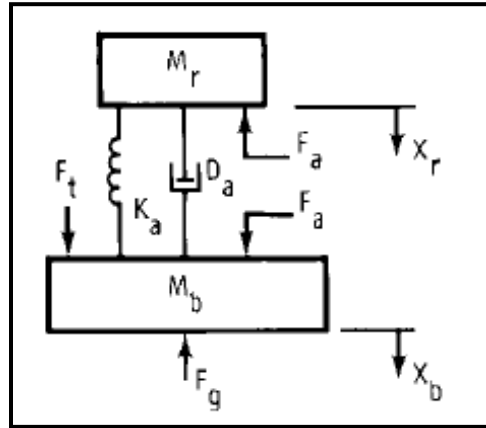


Figure 2.1. Mechanical model of hydraulic vibrator actuator (Sallas, 1984). The variables in this figure are defined as: F_g = Ground force (N), F_a = Actuator force (N), F_t = Dynamic force exerted by the vehicle frame on baseplate due to vehicle vibration (N), D_a = Dashpot constant for actuator (N s/m), K_a = Actuator spring constant (N/m), M_r = Mass of reaction mass (kg), M_b = Mass of baseplate (kg), x_r = reaction mass displacement (m), and x_b = baseplate displacement (m).

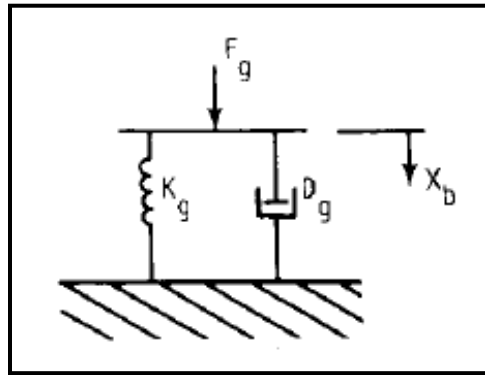


Figure 2.2. Mechanical ground impedance model (Sallas, 1984). The variables in this figure are defined as: F_g = ground force (N), D_g = Ground damping coefficient (N s/m), K_g = Ground spring constant (N/m), and x_b = baseplate displacement (m).

2.3.2. Limitations of the Weighted-sum Approximation for High Frequency Vibroseis

Although the weighted-sum approximation is the industry standard, there are limitations with this method. Beaten and Ziokowski (1990) determined the limitations of correlating with the weighted-sum approximation:

- 1) The weighted-sum signal will not equal the pilot sweep due to noise in the source equipment and inaccuracies in the feedback system used during acquisition.
- 2) The baseplate does not act as a rigid body.

Although noise within the source equipment can never be completely removed, it can be reduced. Previous work at the Kansas Geological Survey (KGS) by Rademacker (2006) focused on reducing source noise associated with the telemetry system used for signal transmission, noise from the accelerometers, and the vibrator engine noise. It was concluded that low noise accelerometers recorded on a dedicated Geometrics 24-bit A/D seismographs reduced noise considerably compared to the standard factory accelerometers transmitted via business radio band carrier.

The main limitation of the weighted-sum approximation for high frequency data arises from the baseplate model. The baseplate model assumes that the displacement underneath the baseplate is uniform. A study by van der Veen et al. (1999) concluded that using the weighted-sum method to calculate ground force was valid for a portable vibrator with a permanent magnet (66 kg) acting as a reaction mass that is connected by a spring to a baseplate (3.5 kg) for up to 500 Hz because the baseplate was significantly smaller than the reaction mass. Although this may be true for the case of a small vibratory system, studies by Allen et al. (1998) and Wei (2008a) establish that the weighted-sum approximation only represents true ground force for a narrow bandwidth dependent on the baseplate rigidity and near-surface conditions beneath the baseplate, and is increasingly inaccurate as the frequency increases. When the vibrator is driven at high frequencies (>150 Hz), the baseplate begins to flex and the rigid body assumption is invalid (Sallas et al., 1985; Beaten, 1989; Allen et al., 1998; Lebedev and Beresnev, 2004;

Sargiotis et al., 2010). Flexing of the baseplate will result in amplitude and phase variations in turn altering the transmitted seismic energy.

2.3.3. Flexural Rigidity Method

It has been shown that the flexural rigidity method for approximating ground force proposed by Baeten and Ziolkowski (1990) provides a more accurate approximation of the true ground force, especially for frequencies above 100 Hz (Baeten, 1989). Since the focus of this study is to optimize the resolution for high frequency reflection data, this method was investigated.

Unlike the weighted-sum approximation, the flexural rigidity method generates a non-uniform distribution of traction and displacement. The baseplate model used in the flexural rigidity method incorporates the flexure of the baseplate when subjected to the force of a dynamic load, but does not incorporate the elasticity of the foundation on which the plate is vibrating. To employ the flexural rigidity method, an approximation based on classical plate theory describing the plate deformation is derived using the stiffness (flexural rigidity) of the baseplate, and the surface density of the baseplate mass.

The vibrators used by the KGS are manufactured by Industrial Vehicles International (IVI) located in Tulsa, Oklahoma. High frequency data are routinely collected by the KGS with one of two IVI vibrators: the Minivib I or the Minivib II. Both vibrators are equipped with circular non-uniform plates that vary in thickness. Minivib I has a smaller baseplate than Minivib II and has the ability to collect higher frequency data.

Although the baseplates are circular on the IVI mini vibrators, the Cartesian coordinate system will be used for simplicity. Baeten (1989), furthermore, solves the governing plate equation for a uniformly thick infinite plate, h . For this reason, the use of the Cartesian

coordinate system is most convenient. Similarly, the plate equation can be derived for circular plates using the polar coordinate system.

The distributions of traction and displacement of the baseplate is investigated using classical plate theory. Using the assumptions of classical plate theory (Appendix B), the deflection of a uniformly thick isotropic (uniform elastic properties) baseplate subjected to a dynamic load can be described by the equation (Rao, 2007; Chakraverty, 2008):

$$D \left\{ \frac{\partial^4 w(x,y,t)}{\partial x^4} + 2 \frac{\partial^4 w(x,y,t)}{\partial x^2 \partial y^2} + \frac{\partial^4 w(x,y,t)}{\partial y^4} \right\} + \rho h \frac{\partial^2 w(x,y,t)}{\partial t^2} = p(x,y,t) \quad (8)$$

where h is the plate thickness, and ρ is the density of the baseplate, D is the flexural rigidity of the plate (plate stiffness), $w(x,y,t)$ is the deflection of the plate, and $p(x,y,t)$ is the pressure applied to the vibrator baseplate. During a sweep, the total pressure applied to the baseplate is the sum of the traction at the earth's surface and the pressure applied at the top of the baseplate (Equation B.7) (Baeten, 1989).

To solve equation (8), the solution must simultaneously satisfy all prescribed boundary conditions on the cylindrical surface (edge of baseplate) for the vibrator baseplate problem. The fixed edge, the simply supported edge, and the free edge are boundary conditions defined by the fastening or supporting conditions present at the edge of the baseplate (Ventsel and Krauthammer, 2001). For each individual boundary, one of the three conditions must be satisfied. Since the baseplate vibrates freely on the Earth's surface, a free edge boundary condition (Equation B.8) for all boundaries must be fulfilled in the solution to the problem.

It is important to note that equation (8), subjected to the boundary conditions cannot be solved analytically. For that reason, Baeten (1989) approximates a solution to the problem using a Green's function by considering an infinite plate of uniform thickness, h , subjected to a point load in the Fourier domain (Equation B.10). A Green's function is a type of function used to

solve a nonhomogeneous differential equation subject to specific boundary conditions (Duffy, 2001). Using the Green's function, the displacement of the baseplate can be calculated by spatially convolving the Green's function (Equation B.11) with the pressure applied to the baseplate (Equation B.7) (Baeten, 1989; Duffy, 2001):

$$W(k_x, k_y) = \iint_{SF} \{P^{applied}(k'_x, k'_y) + T_s(k'_x, k'_y)\} G^{plate}(k_x - k'_x, k_y - k'_y) dk'_x dk'_y \quad (9)$$

where (k_x, k_y) is the observation position in the Fourier domain and (k'_x, k'_y) is the position of integration in the Fourier domain.

Baeten (1989) shows that the solution (Equation B.11) to equation (8) can be simplified by assuming the Green's function is constant across the baseplate. This is similar to assuming uniform displacement across the baseplate. If the plate is infinitely stiff, assuming the Green's function is constant corresponds to uniform displacement across the baseplate. The constant Green's function assumption is true when (Baeten, 1989):

1. the frequency of vibration and mass densities of the baseplate are low;
2. the flexural rigidity of the plate is large;

$$D \gg \sigma \omega^2 r^4, \quad (10)$$

where σ is the mass density of the baseplate, ω is the angular frequency, and r is the baseplate radius. Since the vibrator baseplate is designed to be extremely stiff, the Green's function for displacement is approximately constant across the baseplate and the equation (9) can be simplified (Baeten, 1989) to:

$$W(k_x, k_y) = W = -\frac{1}{8i\omega\sqrt{\sigma D}} \iint_{SF} \{T_s(k'_x, k'_y) + P^{applied}(k'_x, k'_y)\} dk'_x dk'_y \quad (11)$$

To approximate the ground force with the flexural rigidity baseplate model, the baseplate motion must be expressed in terms of acceleration. Taking the second derivative of equation (11) at the center of the baseplate yields (Baeten, 1989):

$$A_b^c(k_x, k_y) = -\frac{i\omega}{8\sqrt{\sigma D}} \left\{ \iint_{s_F} T_s(k'_x, k'_y) - M_r A_r \right\} \quad (12)$$

where $A_b^c(k_x, k_y)$ is the measured acceleration at the center of the baseplate, M_r is the mass of the reaction mass, A_r is the measured acceleration of the reaction mass. The calculated acceleration using the simplified flexural rigidity method is in close agreement to the exact flexural rigidity method (Baeten, 1989). Consequently, the simplified flexural rigidity method can be used to approximate the ground force signal from measurements of acceleration on the baseplate and on the reaction mass.

Baeten (1989) compared the measured acceleration of the baseplate to the predicted acceleration calculated using the flexural rigidity method. The results showed that the two signals differed in phase approximately 90° over the sweep frequency bandwidth. To correct for this phase shift, the Green's function is multiplied by a factor of i , which corresponds to a 90 degree phase shift. This method is referred to as the phase-corrected flexural rigidity method (Baeten, 1989).

Solving for the traction underneath the baseplate in equation (12), the phase-corrected flexural rigidity method approximates the ground force signal with the expression:

$$F^G = - \iint_{s_F} T_s(k_x, k_y) dk_x dk_y = \left[\frac{8\sqrt{\sigma D}}{\omega} A_b(k_x^c, k_y^c) - M_r A_r \right] \quad (13)$$

where F^G is the approximated ground force, and $A_b(k_x^c, k_y^c)$ is the acceleration measured at the center of the baseplate.

Equation (13) approximates the ground force incorporating the baseplate rigidity. Since baseplate flexure increases as the sweep frequency increases, this method should provide a more accurate approximation of ground force for higher frequency data, thus, increasing the data resolution.

2.3.4. Limitations of the Flexural Rigidity Method

Despite the fact that the phase-corrected flexural rigidity method proposed by Baeten (1989) provides significant improvements when approximating high frequency source signatures, there are still limitations that arise from using this method. Initially, it was derived and developed using the Prakla Seismos VVDA vibrator (total weight $\approx 31,000$ lbs), which is significantly larger than Minivib I (total weight $\approx 11,500$ lbs) and Minivib II (total weight $\approx 14,000$ lbs). Since this method is not widely used in industry, it has not been applied to many seismic vibrators. Consequently, this approximation may be vibrator specific.

It has been previously noted by Sallas (2010) that the distribution of traction underneath the baseplate and distribution of mass on the baseplate is not uniform. Consequently, the assumption that the mass is distributed uniformly across the baseplate is invalid. Furthermore, the baseplate is rarely on a flat surface. As a result, the boundary conditions for the problem change from groundpoint to groundpoint violating the analytical solution.

Two other limiting factors arise from the derivation and solution to the equation. First, the approximation is derived by solving the plate equation for a uniformly thick, isotropic plate. The seismic vibrators used at the KGS are both equipped with baseplates that vary in thickness. As a result of the variable thickness, the flexural rigidity of the baseplate changes in the radial direction. This introduces a more complex governing equation of motion, which cannot be simplified analytically to a practical ground force approximation. For this reason, an average flexural rigidity for the baseplate must be used in the phase-corrected flexural rigidity approximation. Second, the approximation of the ground force is calculated using the accelerations of the baseplate at the center of the plate. The location of the baseplate accelerometer on Minivib I and Minivib II is not located at the center of the plate. As a result, the

measured acceleration will not be equal to the acceleration at the center of the baseplate. These additional variations may decrease the accuracy of the phase-corrected flexural rigidity signal resulting in a source signature approximation that will not optimize high frequency data and therefore, resolution for Minivib I and Minivib II.

2.3.5. High Fidelity Vibroseis Seismic (HFVS) Method

An alternative method proposed by Allen (1996) called the High Fidelity Vibroseis Seismic method (HFVS) uses inverse filtering by spectral division to remove the unknown applied force. The method was developed by recognizing that the measured vibrator motion is related to the true vibrator motion by a minimum phase transfer function in the frequency domain (Allen, 1996):

$$G_m(f) = G_t(f) \cdot T(f) \quad (14)$$

where $G_m(f)$ is the measured vibrator motion (known), $G_t(f)$ is the true vibrator motion (unknown), and $T(f)$ is a minimum phase, causal, linear transfer function (unknown) .

From the vibroseis convolution model, the time derivative of the true vibrator signal is multiplied by the impulse response of the earth in the frequency domain (Miller and Pursey, 1954; Aki and Richards, 1980). Therefore, an uncorrelated seismogram is represented by:

$$U(f) = i\omega \cdot G_t(f) \cdot E(f) \quad (15)$$

where $U(f)$ is the uncorrelated measured seismic data, $i\omega$ is the time derivative, and $E(f)$ is the earth reflectivity sequence.

This method differs from conventional practice because an estimate of the actual signal is not used to correlate the data. Alternatively, the data is divided by the minimum phase relative of the actual signal (measured motion) in the frequency domain (Allen, 1996). Before inverse

filtering, white noise must be added to $G_m(f)$ to stabilize the inverse operation. Using equations (14) and (15), inverse filtering by spectral division is represented by:

$$\frac{U(f)}{G_m(f)} = \frac{i\omega \cdot G_t(f)}{G_t(f) \cdot T(f)} \cdot E(f) \quad (16)$$

Consequently, this removes the true vibrator signal from the equation. Therefore, equation (16) can be reduced to

$$\frac{U(f)}{G_m(f)} = \frac{i\omega}{T(f)} \cdot E(f) \quad (17)$$

From the properties of minimum phase functions, the time derivative and the reciprocal of a minimum phase function are also minimum phase (Allen, 1996; Yilmaz, 2001). Through minimum phase deconvolution, the seismogram can be further processed to eliminate $\frac{i\omega}{T(f)}$ and recover the earth's reflectivity sequence.

2.3.6. Limitations of HFVS Method

The limitations of HFVS processing stem from the assumptions underlying deconvolution and from inverse filtering by spectral division. In previous research by Rice (2009), correlation of near-surface seismic reflection data by the ground force signal has not shown significant improvements when compared to traditional cross-correlation with the ideal signal (synthetic). Such a result may be explained by the theoretical assumptions underlying deconvolution which are not all valid for shallow data (Steeple and Miller, 1998). First, the assumption that the source waveform is static and does not change as it travels through the subsurface is invalid. Vertical and lateral variability of near-surface material properties preferentially attenuate the high frequency component of the source waveform (Steeple and Miller, 1998). Second, near-surface seismic reflection data sets generally target/capture a small number of horizons. With only a small number of reflective horizons, the earth is not

representative of an infinite reflectivity series (Steeple and Miller, 1998). Lastly, shallow seismic data generally has a low signal to noise ratio. Noise is magnified by the process of deconvolution leaving little true signal to correlate (Bickel, 1982; Brittle et al., 2001).

Inverse filtering through spectral division can become problematic when the measured signal is small at any point within the frequency bandwidth (Krohn, 2008). When this occurs, the inverse filter will apply large gain and amplify noise. If the signal is zero at any frequency, the inverse becomes unstable. In practice, white noise is added to stabilize the inverse. This process is called pre-whitening the data. When the data is pre-whitened, the added noise can alter the shape of the signal as well as the signal phase resulting in a mixed phase signal (Bickel, 1982). Applying minimum phase deconvolution to a mixed phase signal will result in less than optimum results.

3. Problem Statement

Although deconvolving the unprocessed vibroseis records with an accurate source signature should always produce superior data quality compared to cross-correlation with the synthetic sweep (van der Veen et al., 1999; Ghose, 2002; Wei, 2008), previous work at the KGS by Rice (2009) using the IVI Minivib I did not support these findings. Empirical results from the KGS study concluded that no significant gains in data fidelity can be obtained by deconvolving with the weighted-sum ground force approximation due to the inaccuracy of the current ground force approximation. The current weighted-sum approximation of ground force is calculated using one reaction mass accelerometer and one baseplate accelerometer located approximately 35 cm from the center of the baseplate. For conventional seismic vibrators, the ground force approximation becomes increasingly inaccurate as the frequency of the sweep increases above > 100 Hz because the rigid body assumption is violated due to baseplate flexure (Sallas et al., 1985; Beaten, 1989; Allen et al., 1998; Lebedev and Beresnev, 2004; Sargiotis et al., 2010). The motion of the baseplate must fully be investigated to determine the validity of the rigid body assumption for high frequency data. Additionally, collecting acceleration from a single point on the baseplate can vary due to the non-rigidity of the driven structure and the near-surface condition beneath the baseplate (Wei, 2009; Sallas, 2010). Analyzing the response variability across the vibroseis baseplate on varying near surface conditions will help determine optimal location(s) to measure baseplate acceleration. Comparing various ground force approximations to the true ground force (collected by the Load Cell System) will determine the most representative ground force approximation.

The IVI Minivib I can generate energy from 10 to 550 Hz, but the highest frequency historically recoverable by the KGS using this source has been approximately 300 Hz.

Comparing the spectral characteristics of the accelerometer signals and analyzing the true ground force will help determine why these higher frequencies produced by the IVI Minivib I are not recoverable.

4. Equipment Setup

Five Columbia Research Laboratories (CRL) 966 magnetic mount accelerometers were used to determine the optimal locations for an augmented weighted-sum calculation of ground force, to investigate if the baseplate motion is symmetric throughout each sweep, and to analyze the modal characteristics of the baseplate. The CRL 966 model was selected over Endevco model 7703A-1000 accelerometers, currently used by the KGS, because it does not need an external charge amplifier to boost its signal, and it is readily available from Seismic Source Company (SSC). Additionally, the magnetic mounts were ideal for this application because the accelerometers could be quickly moved to different locations on the baseplate. Although Geometrics seismographs were not used to record the CRL accelerometer signals in this study, a sensitivity of 10 mV/g was selected to assure a low-level differential accelerometer signal that can be recorded with Geometrics Geode seismographs. The CRL accelerometers use a different recording system than currently used by the KGS. The accelerometer array includes a SSC 24 channel accelerometer interface box connected to the Seismic Source DAQ III seismograph that transmits the data to a computer via Ethernet (Figure 4.1).

Two Endevco accelerometers, one located on the reaction mass and one located on the baseplate, were used to acquire additional signals necessary to calculate a weighted-sum ground force. Previous research established that the Endevco accelerometers provided improved signal to noise ratio when compared to the Dytran 3184 accelerometers, which are used as the open-loop feedback signal for the vibrator control system (Rademacker, 2006). In addition, the signals were collected to compare with the CRL accelerometers for signal characteristic assurance and to correlate consecutive sweeps for analysis of the baseplate motion using numerous accelerometer locations. An accelerometer sensitivity of 3 mV/g was selected to insure compatibility with

Geometrics Geode seismographs. A laptop computer inside the Minivib received the signals from a Geometrics seismograph and stored the 24-bit individual accelerometer traces.

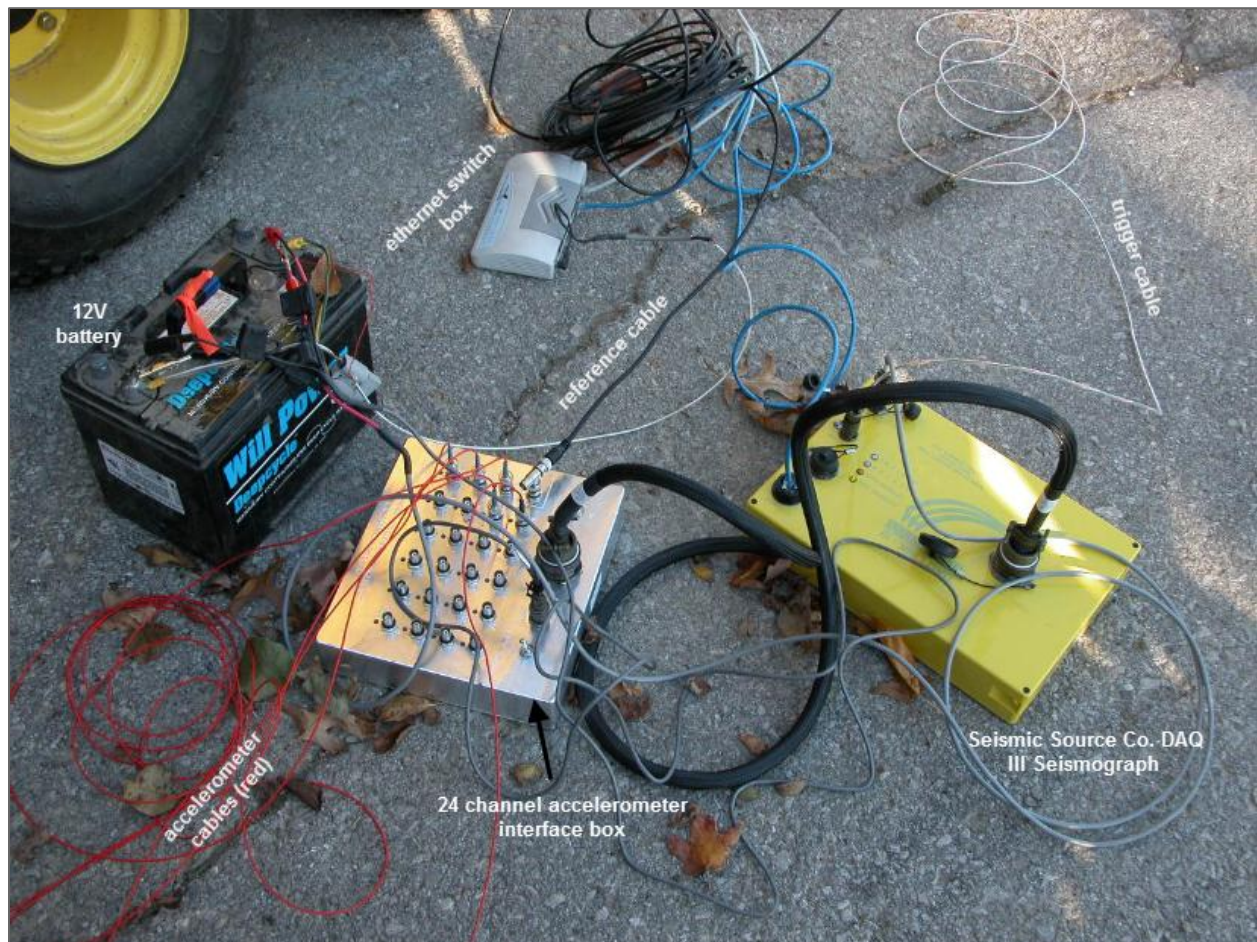


Figure 4.1. Equipment configuration for recording CRL 966 magnetic mount accelerometers

During the second part of the survey, the Dytran 3184 accelerometer signals from the vibrator control system were collected to allow comparison of the ground force feedback signal to both weighted-sum approximations calculated from the Endevco and the CRL accelerometers (Figure 4.2). Through these comparisons, the accuracy of the vibrator quality control feedback signal can be investigated.

A system of load cells consisting of three tiles, each containing three load cells, was used in the second part of the survey to measure the true ground force. The Load Cell System was

placed beneath the baseplate to dynamically measure the true ground force applied to the Earth by the Minivib (Shan et al., 2009). This SCC system was made up of by individual load cells on each plate with a capacity of 25,000 lbs. As a result, the system capacity was 225,000 lbs.

Individual load cell sensors convert force into an electrical signal and send the signals through an interface box to the Seismic Source DAQ III seismograph (Figure 4.3). True ground force is calculated by summing all individual electrical signals.



Figure 4.2. Reaction mass accelerometer locations for all three accelerometer models: Dytran model 3184 (≈ 100 mV/g sensitivity), Endevco model 7703A-1000 (3 mV/g sensitivity), and CRL magnetic model model 966 (10 mV/g sensitivity).

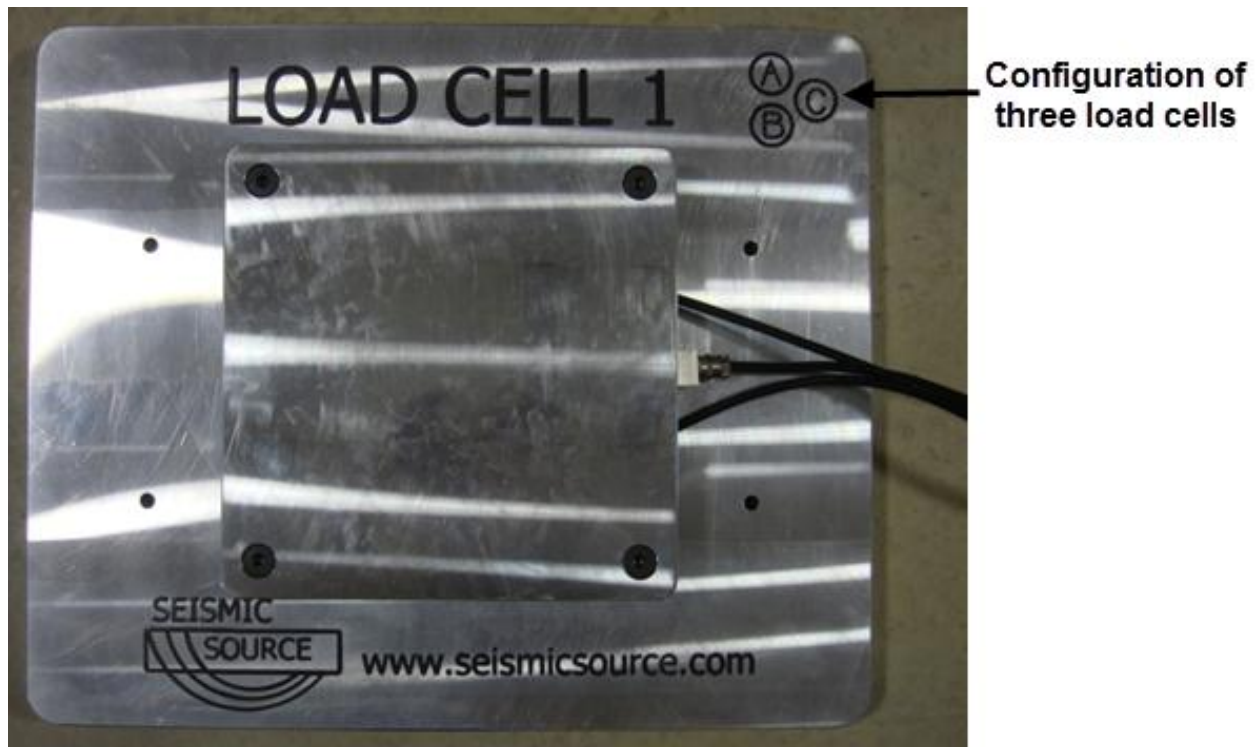


Figure 4.3. Image of load cell plate, diagram in top right corner depicts the configuration of three load cell sensors (Modified from Seismic Source Co.).

5. Methods: Part 1; Investigation of Baseplate Motion

5.1. Purpose Statement

A suite of experiments were developed to examine the motion of the IVI Minivib I baseplate throughout the sweep. The baseplate motion must fully be investigated to produce an optimal approximation of the source signature for the IVI Minivib I. Ideally, the baseplate should have a uniform response across its surface, which theoretically equates to an infinitely rigid plate acting as a point source of wave propagation. Variations in phase and amplitude response across the baseplate must be evaluated since an infinitely stiff driven structure is unattainable. The IVI Minivib I is equipped with a symmetric dome-shaped circular baseplate, which varies in thickness in the radial direction. Amplitude and phase variations associated with accelerometer radial position were investigated to ascertain the dependence of ground response to baseplate geometry.

The baseplate interior structure consists of 24 radial ribs that radiate out of the center of the baseplate reinforcing the upper dome structure of the plate which connects to the edge of the baseplate. A circumferential rib is located approximately 10 cm from the edge of the baseplate (Figure 5.1). These ribs present structural complication to achieving a uniform response. Theoretically, the ribs will generate a non-uniform distribution of rigidity across the baseplate.

As the frequency increases, the baseplate is more likely to flex generating asymmetric baseplate motion (Lebedev and Beresnev, 2005; Sallas, 2010; Wei, 2010). The response variability due to the accelerometer position with respect to location of reinforcement ribs was analyzed. Based on the internal baseplate structure, the experiment was designed to investigate the change in baseplate motion in the radial direction, the change in baseplate motion associated

with reinforcement ribs and to determine whether the baseplate motion is symmetric throughout the duration of the sweep.

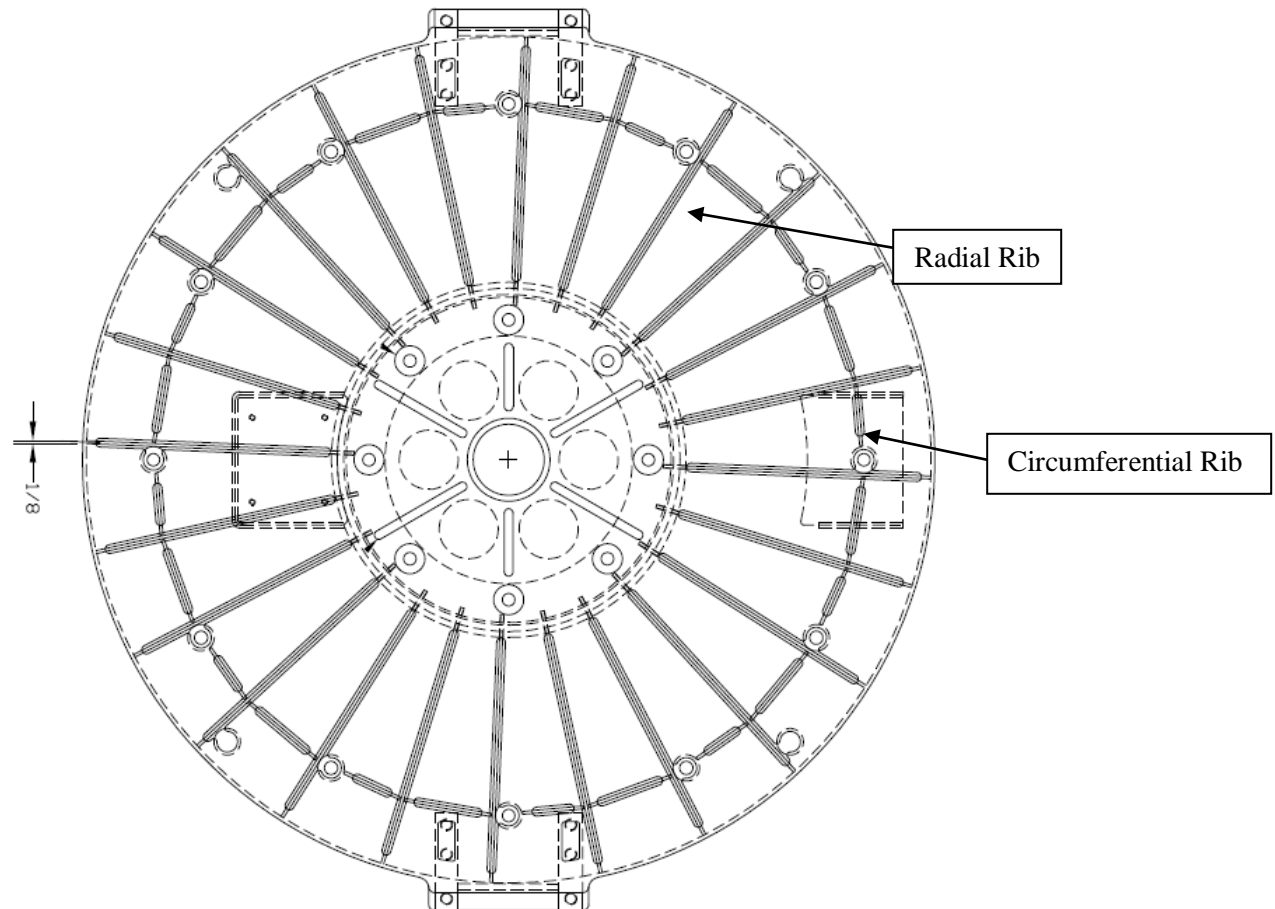


Figure 5.1. Diagram of IVI Minivib I baseplate structure: 24 radial reinforcement ribs, 1 circumferential reinforcement rib (view from bottom of baseplate).

5.2. Geologic Setting and Data Acquisition

High-frequency vibroseis data was acquired using the IVI Minivib I at three source locations around the Kansas Geological Survey located at the University of Kansas west campus in Lawrence, Kansas.

5.2.1. Geologic Setting

Three test sites were all within 200 m of each other, all with the Lawrence Formation representing bedrock (Figure 5.2). Each site consisted of different overburden providing different near-surface conditions from a mechanical perspective (Figure 5.3).

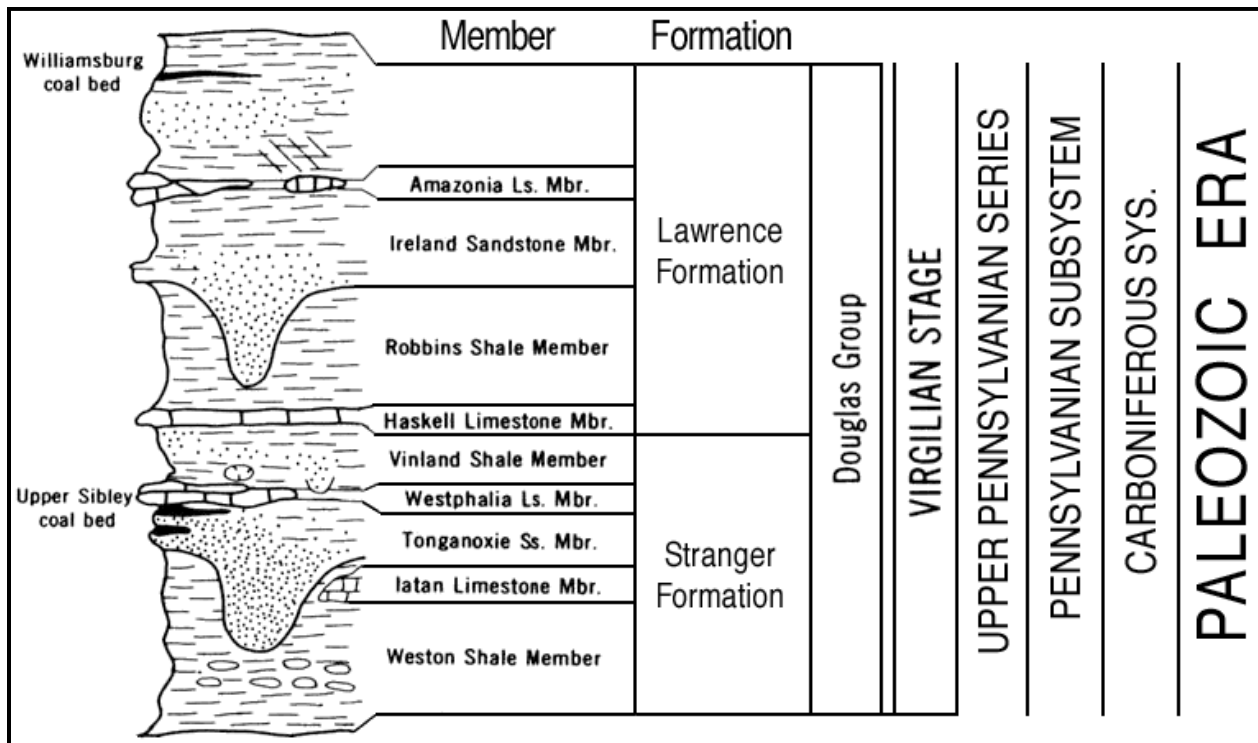


Figure 5.2. Generalized stratigraphy of Douglas Group (Zeller, 1968)

Source location 1 was located on a flat concrete driveway in front of the Kansas Geological Survey “core barn”. Approximately 2 m of the Robbins Shale member lies directly beneath the concrete driveway. An outcrop of the Haskell Limestone member is present approximately 20 m south of source location 1. The flat concrete source location was the most rigid near-surface of the three tested source locations. Source location 2 (\approx 20 m north of the Kansas Geological Survey) was located on a thin layer of soil overlaying approximately 3 m of the Robbins Shale member of the Lawrence Shale Formation. In Douglas County, KS, the Martin and Vinland soils are smectite rich soils from weathered shales found in the near-surface

(Dickey et al., 1977). Source location 3 (north of the pond) was located on irregular alluvial outwash. Two days prior to data collection a rain event occurred leaving a semi-saturated irregular surface to test the vibrator baseplate motion.

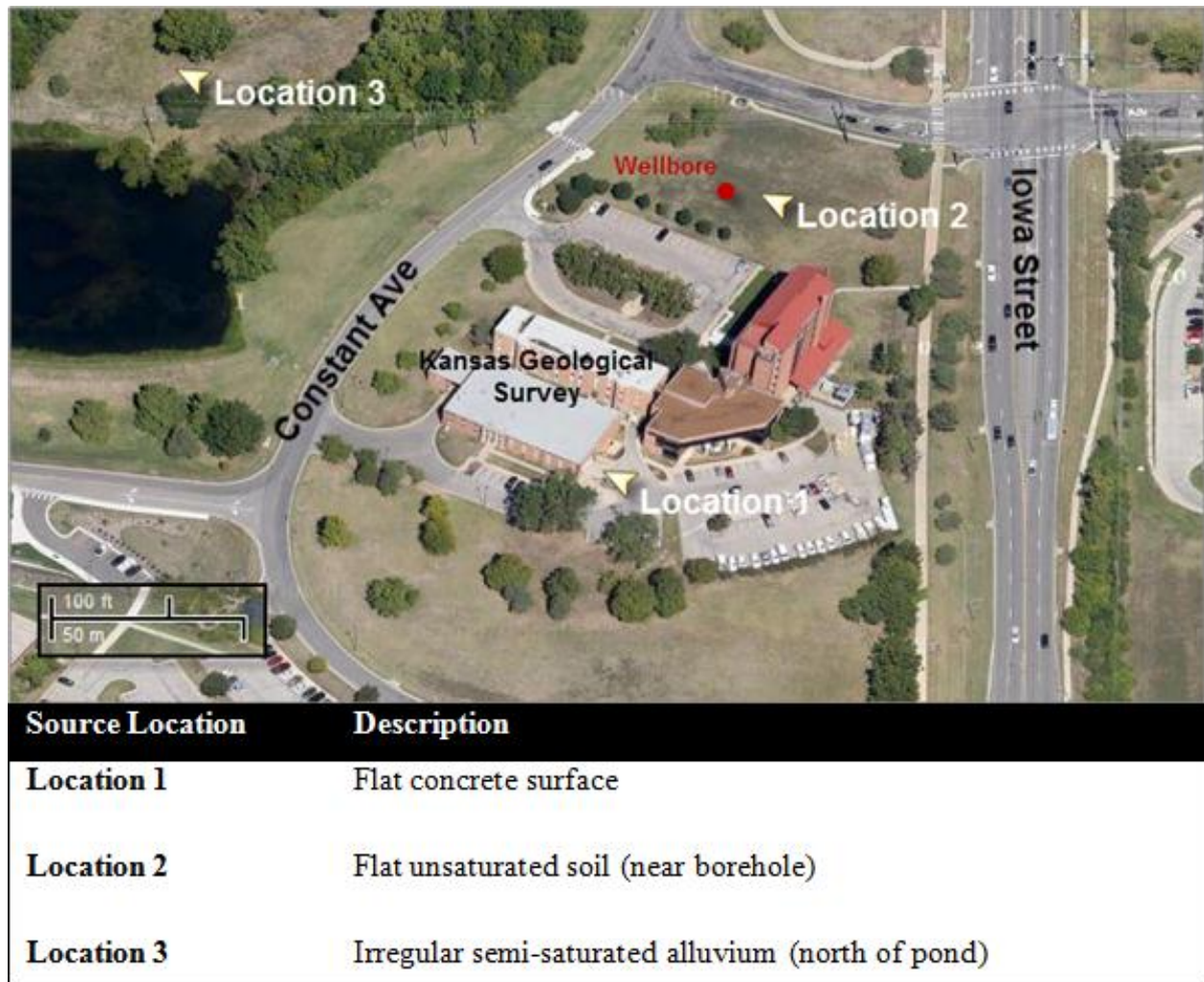


Figure 5.3. Map of source locations for Part 1 of survey (modified from Google Earth)

The Lawrence Shale is an interval within the Douglas Group and was deposited in the Upper Carboniferous period. The Lawrence Shale Formation is subdivided into five members: the Haskell Limestone, the Robbins Shale, the Ireland Sandstone, the Amazonia Limestone and an unnamed discontinuous shale member containing Williamsburg coal bed (Zeller, 1968). The Haskell Limestone member is a blueish-gray fine grained oolitic limestone that varies from 0.5

m to 1.5 m in thickness. The Robbins shale member is a clay-rich grey marine shale that varies from 0 m to 4 m in thickness in Douglas County, KS (O’Conner, 1960).

5.2.2. Data Acquisition

The IVI Minivib I generated a five-second linear upsweep with a frequency range of 30-400 Hz for all sweeps at source location 1 (Table 5.1). A sweep frequency of 30-450 Hz was used for all shots at subsequent locations to determine if the Minivib I was capable of imparting signal at frequencies greater than 400 Hz into the ground.

At each of the source locations, the Endevco 7703A-1000 accelerometer response was compared with the response of the CRL 966 accelerometers. For this comparison, one CRL magnetic mount accelerometer was placed beside both the Endevco reaction mass accelerometer and the Endevco baseplate accelerometer located at approximately 35.5 cm from the center of the baseplate. The Endevco accelerometers are mounted directly to the seismic vibrator on a flat surface allowing accurate calculation of ground force. Five sweeps were recorded separately at each source location.

Five CRL 966 magnetic mount accelerometers were used to analyze the motion of the baseplate. One accelerometer remained on the vibrator reaction mass throughout the experiment (Figure 5.4). The baseplate was divided into four quadrants to determine if the motion of the baseplate was symmetric (Figure 5.5). One of the four remaining accelerometers was placed directly on top of the baseplate in each of the four quadrants. For each source location, three radial positions were tested in each quadrant: 17.75 cm, 26.67 cm, and 35.5 cm from the center of the baseplate. At each radial position, five sweeps were collected separately with the accelerometers located on a reinforcement rib. Then, data was recollected in the same fashion with the accelerometers located off of a reinforcement rib (Figure 5.5).

Table 5.1. Survey parameters for each experiment

	Experiment 1- Source Location 1	Experiment 1- Source Location 2	Experiment 1- Source Location 3	Experiment 2
Source	Minivib I	Minivib I	Minivib I	Minivib I
Frequency Range	30-400 Hz	30-450 Hz	30-450 Hz	30-450 Hz
Sweep Length	5 sec	5 sec	5 sec	5 sec
Listening Time	1 sec	1 sec	1 sec	1 sec
Sampling Rate	0.5 ms	0.5 ms	0.5 ms	0.5 ms
Front Taper	0.5 sec	0.5 sec	0.5 sec	0.5 sec
Back Taper	0.25 sec	0.25 sec	0.25 sec	0.25 sec
Vibrator Force Output	7000 lbs	7000 lbs	7000 lbs	7000 lbs
% Force Correction	20%	20%	20%	20%

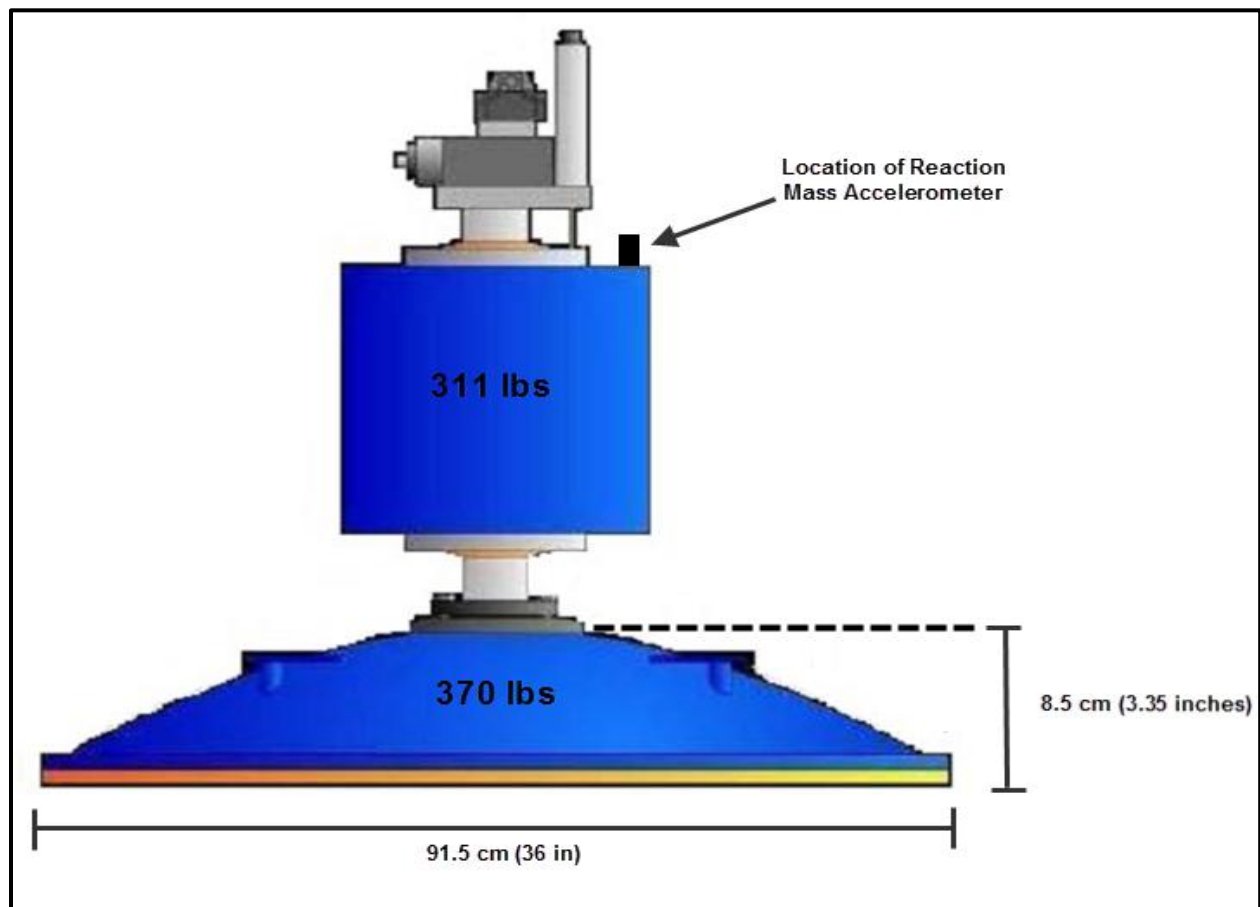
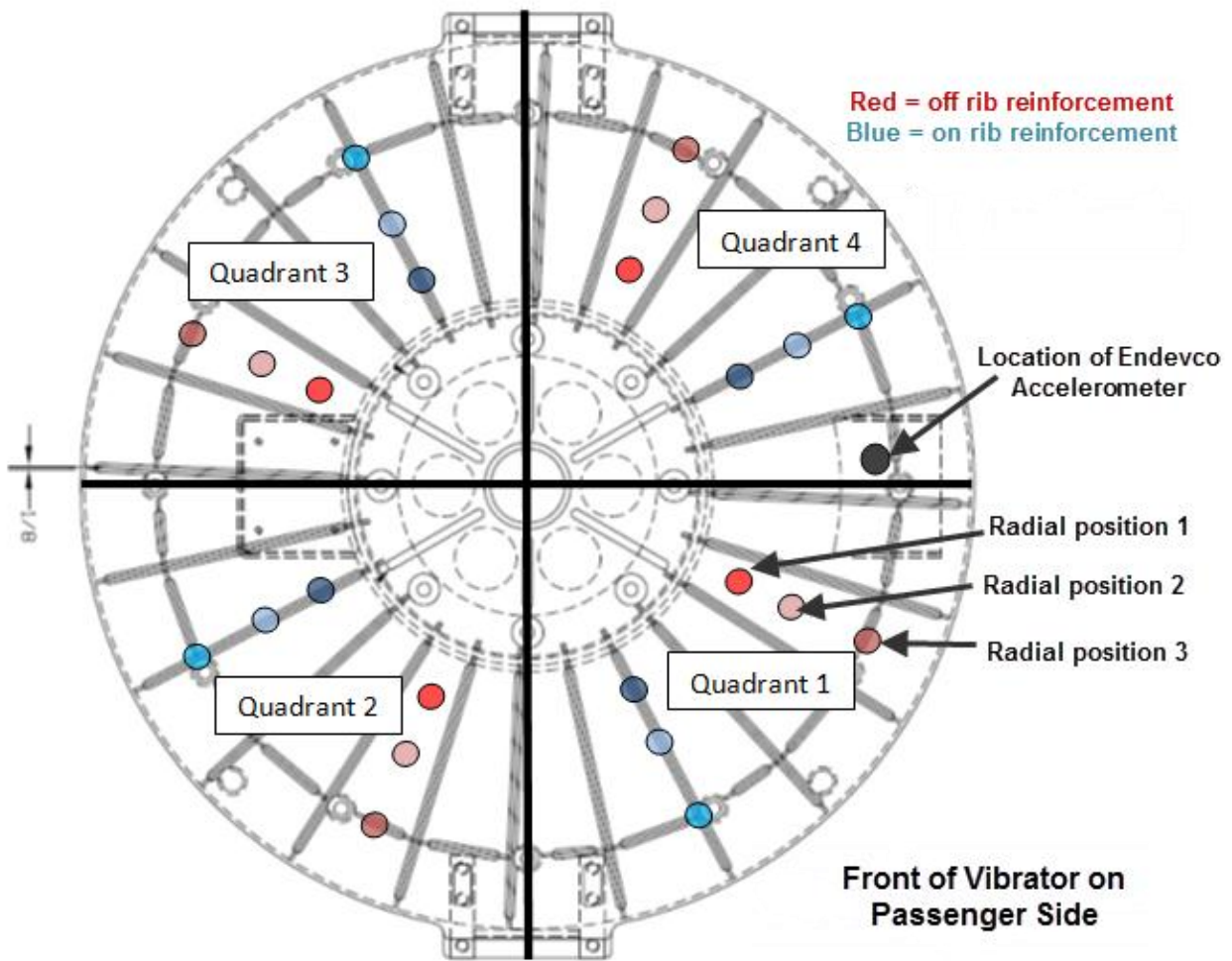


Figure 5.4. Location of reaction mass accelerometer



Accelerometer radial location	Distance from center of baseplate	Approximate radial distance between accelerometer locations
Position 1	17.75 cm	9 cm
Position 2	26.67 cm	9 cm
Position 3	35.5 cm	18 cm

Figure 5.5. Diagram displaying three radial positions on reinforcement ribs and off reinforcement ribs in all 4 quadrants.

Next, accelerometers were positioned in quadrant 1 to determine the change in accelerometer response associated with radial accelerometer location and baseplate structure.

Five sweeps were collected separately with accelerometers positioned at radial position 1 and 2

with corresponding off reinforcement rib and on reinforcement rib locations (Figure 5.6). This experiment was repeated with the accelerometers at radial positions 2 and 3.

It is important to note that this part of the experiment was not designed to approximate ground force. Given that the accelerometers were placed directly on the baseplate, they were off vertical by $\approx 15^\circ$ maximum. Off vertical signals differ from signals that are completely vertical by cosine of the angle (Sill and Seller, 2006). If the baseplate acceleration signals collected were used to calculate ground force, the ground force calculation would include an angular discrepancy associated with off vertical signals. For the purpose of this study, placing the accelerometers directly on the baseplate was adequate.

5.3. Data Analysis

Three source locations with differing material properties, surface terrain, and water saturation provided a variety of near-surface conditions that were tested to examine the motion of the IVI Minivib I baseplate throughout the duration of a sweep. At each source location, tests were conducted to compare the signal response and spectral characteristics of the Endevco 7300-1100A accelerometers, currently used by the KGS, to the CRL 966 accelerometers. Additionally, tests were conducted using an array of CRL accelerometers to investigate the change in accelerometer response associated with the radial position and location of the accelerometer in respect to baseplate structure, and to establish whether the baseplate acts as a symmetric body about the baseplate origin throughout the sweep.

5.3.1. Comparison of Endevco Accelerometers and CRL Accelerometers

The CRL 966 accelerometers were directly compared to the Endevco accelerometer to determine any phase and amplitude variability associated with differences in signal conditioning

between the two models. The two accelerometer models were positioned side-by-side on the reaction mass and the baseplate, and collected simultaneously at each source location to compare variations in phase, amplitude, and absolute peak force.

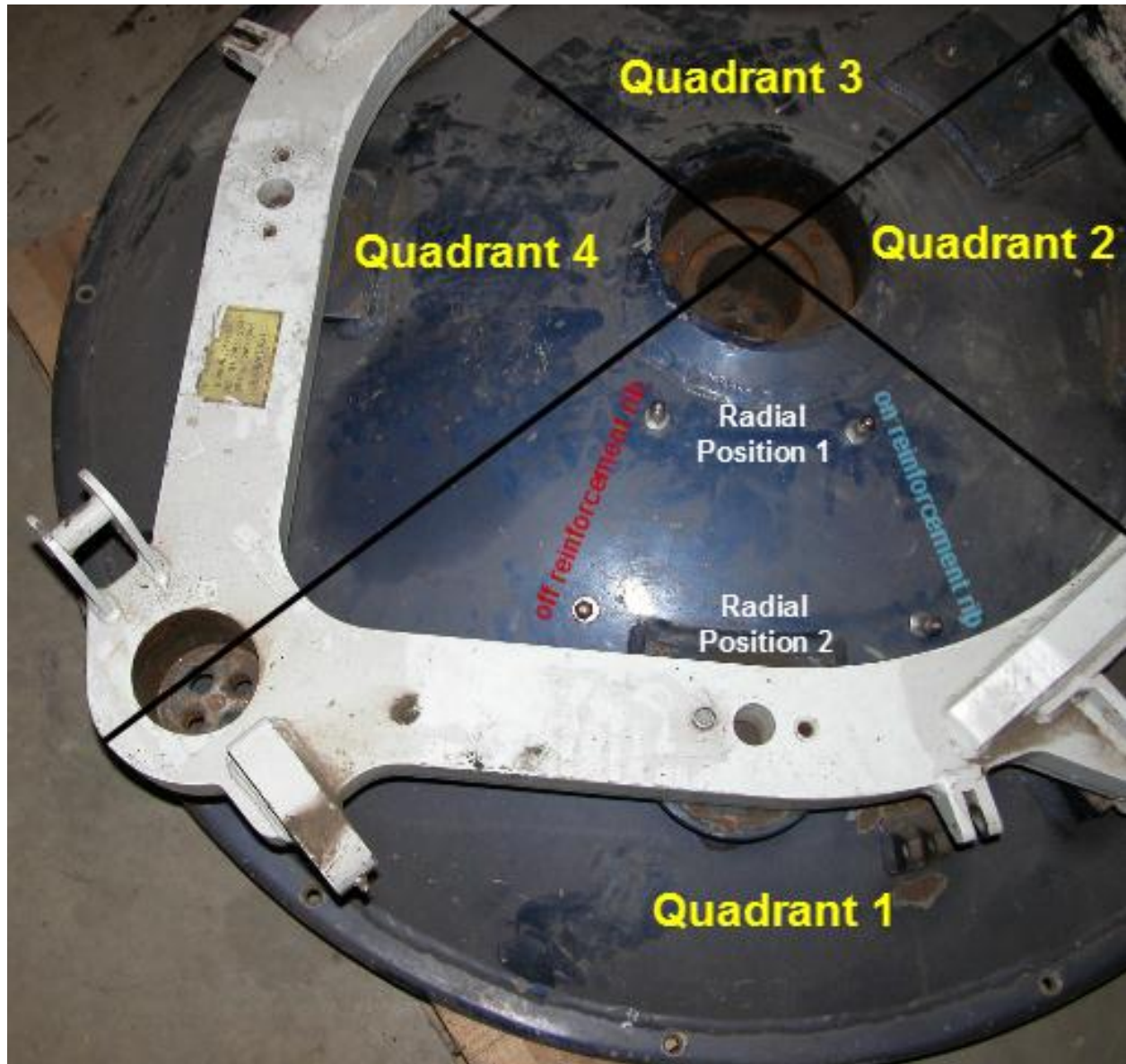


Figure 5.6. Accelerometers located in quadrant 1 at radial positions 1 and 2 collecting data from off reinforcement rib and on reinforcement rib simultaneously

The baseplate and reaction mass signals from each accelerometer model (Figure 5.7) were cross-correlated in the time domain. Cross-correlation of the two accelerometer traces results in a correlation function that contains information regarding the phase difference between

the two signals (Witteaman, 2006). In the time domain, each correlation function was windowed using a Blackman window filter to smoothly attenuate the signal at both ends of the time series minimizing edge effects that result in spectral leakage in the Fourier spectrum (Kay and Marple, 1981). The selection of the blackman window filter was based on its ability to reduce edge effects minimizing spectral leakage (Chassaing and Reay, 2011). The difference in phase between the baseplate and the reaction mass signals for each accelerometer model can be plotted in the frequency domain (correlation phase spectrum). Transforming the windowed cross-correlated signals using the fast Fourier Transform (FFT) (Brigham and Morrow, 1967) is a transform approximation commonly used for computing the discrete fourier transform of a sampled signal. In the frequency domain, the phase of the correlated signal is calculated by taking the inverse tangent of the imaginary part divided by the real part of the complex signal. A 21-point moving average filter was applied to each of correlation phase spectrum for plotting purposes. To show difference between the two accelerometer models, the Endevco correlation phase was subtracted from the CRL correlation phase (Figure 5.8). Both accelerometer models display almost identical phase differences between their respective reaction mass and baseplate signals for all three source locations.

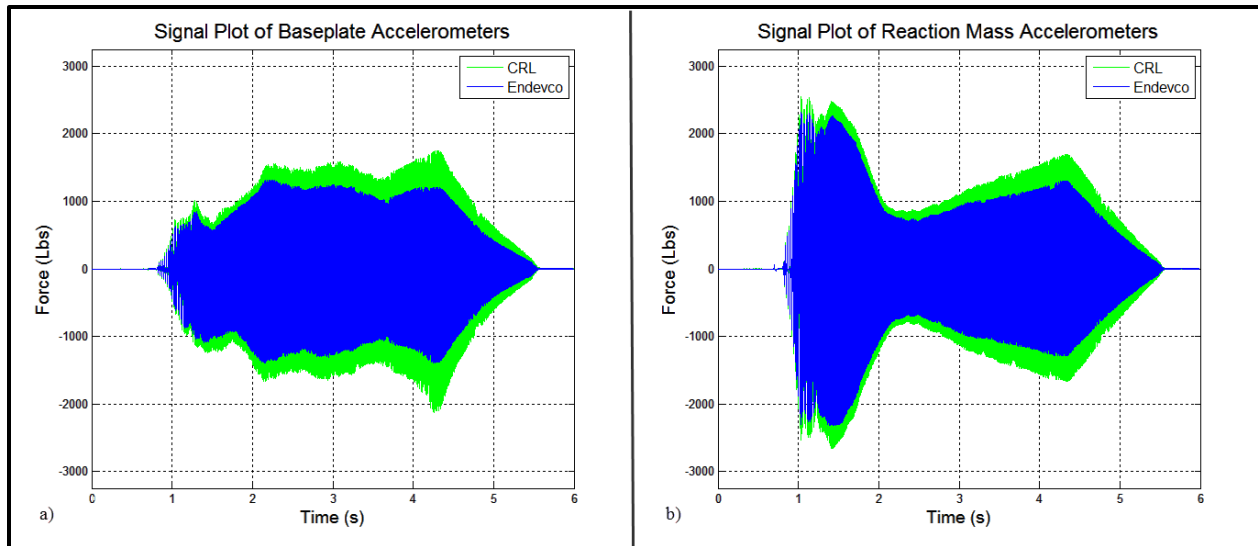


Figure 5.7. Comparison of a) baseplate and b) reaction mass signals from the CRL 966 magnetic mount accelerometer and the Endevco 7703A-1100 accelerometer for source location 1.

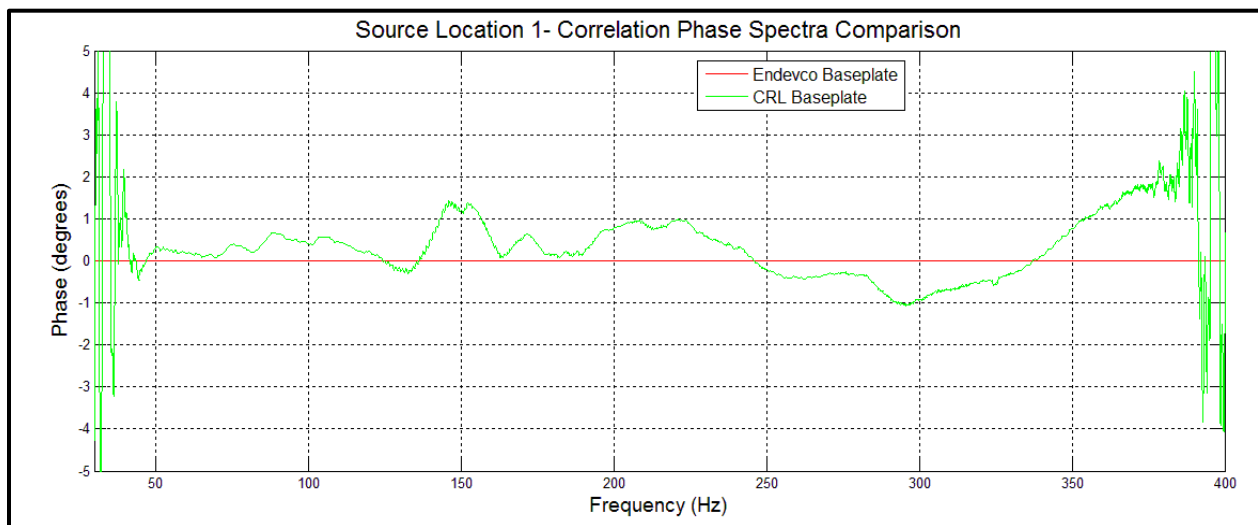


Figure 5.8. Difference of Endevco and CRL accelerometer phase spectrum correlated to each model's respective reaction mass signal.

The differences in amplitude spectra of the two accelerometer models was investigated. Using MATLAB, each signal was transformed to the frequency domain using the FFT. In the frequency domain, each signal was split into its corresponding imaginary and real components. Amplitude was calculated in the frequency domain by computing the modulus of the complex signal (Equation 18):

$$A_x(f) = \sqrt{X_r(f)^2 + X_i(f)^2} \quad (18)$$

where $A_x(f)$ is the amplitude of signal X, $X_r(f)$ is the real component of signal X, and $X_i(f)$ is the imaginary component of signal X. The difference in amplitude of the baseplate and reaction mass signal for the Endevco accelerometer amplitude spectrum with respect to the corresponding CRL amplitude spectrum is given by (Equation 19):

$$A_{db} = 20 * \log_{10}(A_{End}/A_{CRL}) \quad (19)$$

where A_{db} is the amplitude ratio expressed in decibels, A_{End} is the calculated amplitude of the Endevco accelerometer, and A_{CRL} is the calculated amplitude of the CRL accelerometer. A 21-point moving average filter was applied to each amplitude spectrum for plotting purposes (Figure 5.9). The amplitude difference between the Endevco and CRL accelerometers were similar for each of the three source locations. Although an amplitude difference exists between the two accelerometer models, the normalized amplitude spectrum of each baseplate and reaction mass traces for each accelerometer model is almost identical across the sweep frequency range (Figure 5.10).

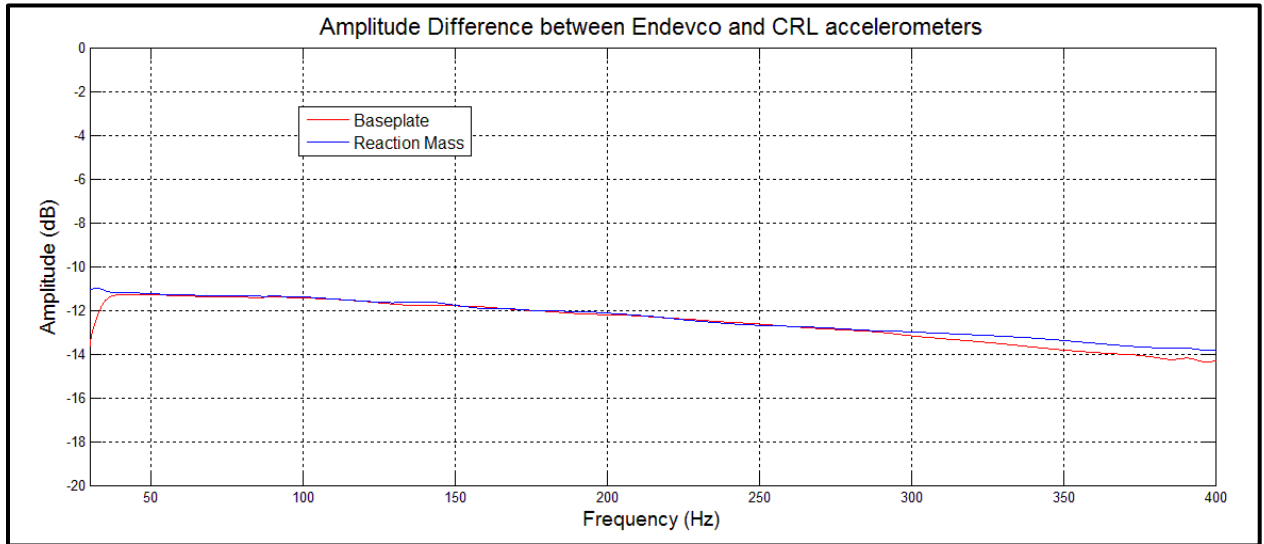


Figure 5.9. Amplitude ratio of Endevco baseplate and reaction mass accelerometers with respect to corresponding CRL accelerometers for source location 1.

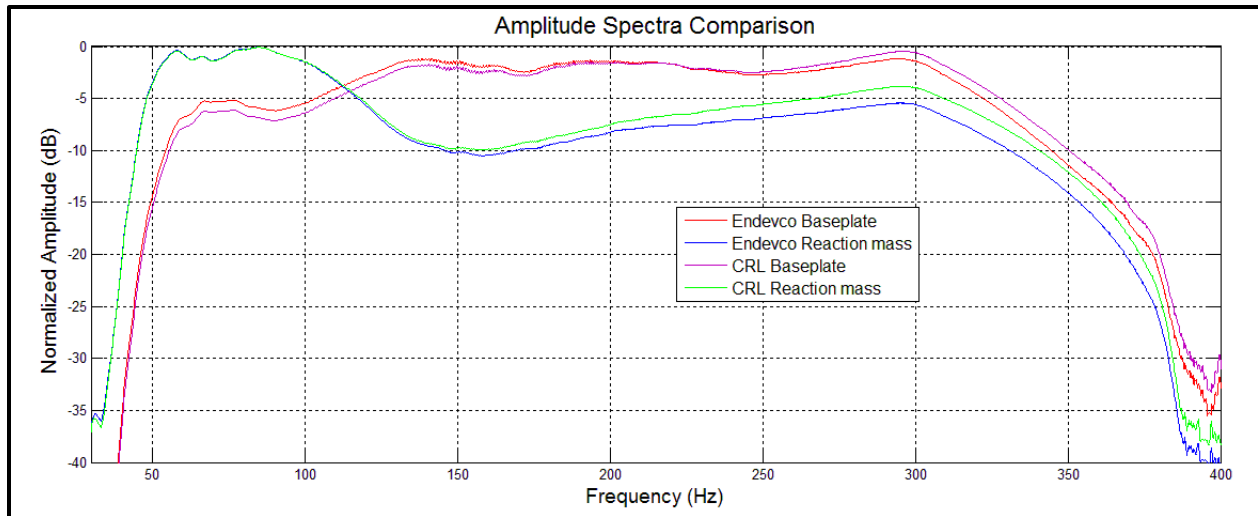


Figure 5.10. Reaction mass and baseplate amplitude spectra comparison between Endevco and CRL accelerometers for source location 1.

At each of the three source locations, ground force was computed using the weighted-sum of the stacked reaction mass and baseplate signals (Equation 7). The resulting ground force traces were cross-correlated to establish a quantitative comparison (Table 5.2). For each of the three source locations, the ground force signals calculated using the output from each accelerometer model were extremely similar (correlation coefficient > 97.0%).

Table 5.2. Correlation between Endevco ground force and CRL ground force signal for each source location.

Source Location		Correlation Coefficient, ρ
1	Endevco ground force ★ CRL ground force	0.9874
	Endevco ground force ★ CRL ground force	0.9870
	Endevco ground force ★ CRL ground force	0.9740

Absolute peak force is represented by the amplitude envelope of the ground force trace (Lerwill, 1981). The amplitude envelope is defined as the absolute value of the complex trace, given by the Hilbert transform of the time-domain signal trace (Costain and Çoruh, 2004). The use of lb-force as a unit of measurement is an industry standard in seismic acquisition; therefore, results are given in lb-force. For each of the three source locations the trend was near identical;

therefore, to avoid redundancy only the absolute peak force comparison of ground force signals calculated from each accelerometer model from source location 1 (Figure 5.11 and Figure 5.12) is displayed.

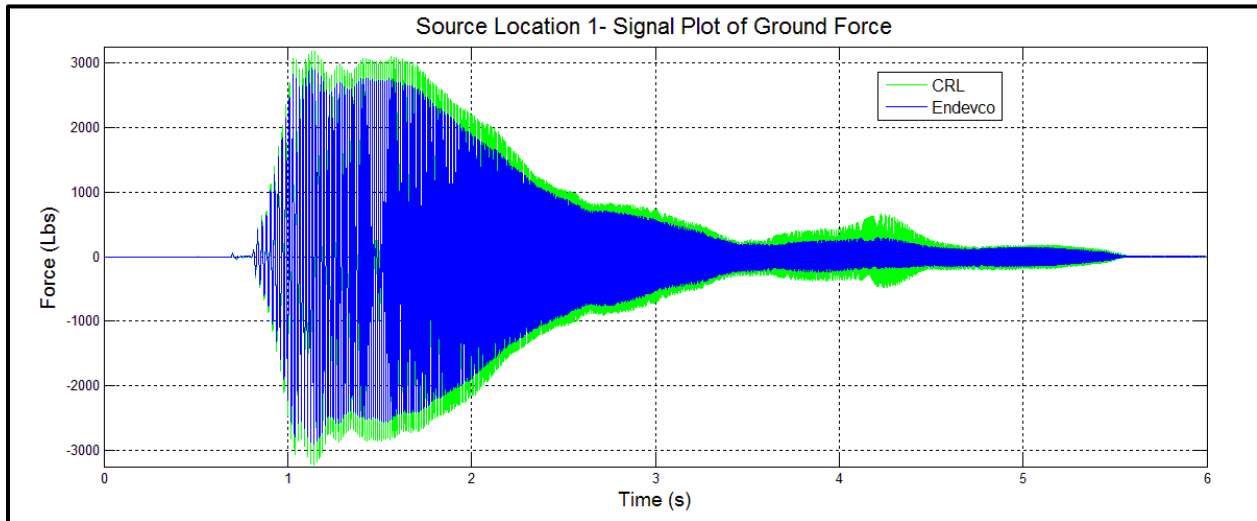


Figure 5.11. Signal plot of computed Endevco and CRL ground force for source location 1

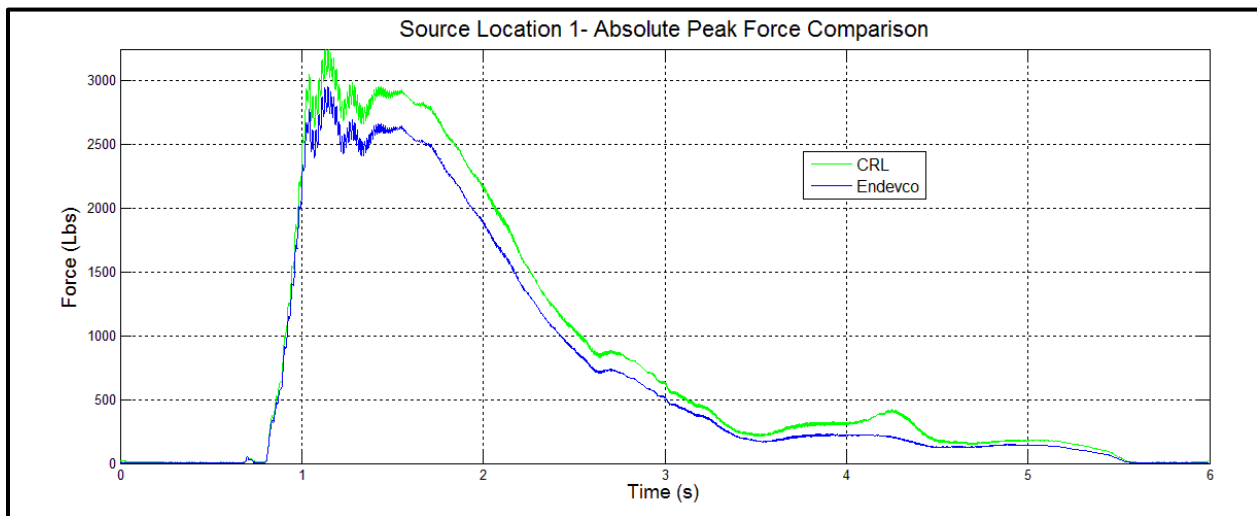


Figure 5.12. Absolute peak ground force of Endevco and CRL signals for source location 1

5.3.2. Sweep Repeatability

To determine the relative consistency of the vibrator output for each source location, the CRL reaction mass accelerometer response for all sweeps in *Part I* was cross-correlated with the ideal signal (synthetic sweep) (Figure 5.13). The standard deviation of the correlation

coefficients was calculated for each source location (Table 5.3). Since the standard deviation is small ($\approx 1\%$) for each source location, the vibrator sweeps acquired at the same shot station can be considered repeatable. Therefore, each radial position was evaluated after stacking the corresponding five individual sweeps, increasing the signal-to-noise ratio for each position.

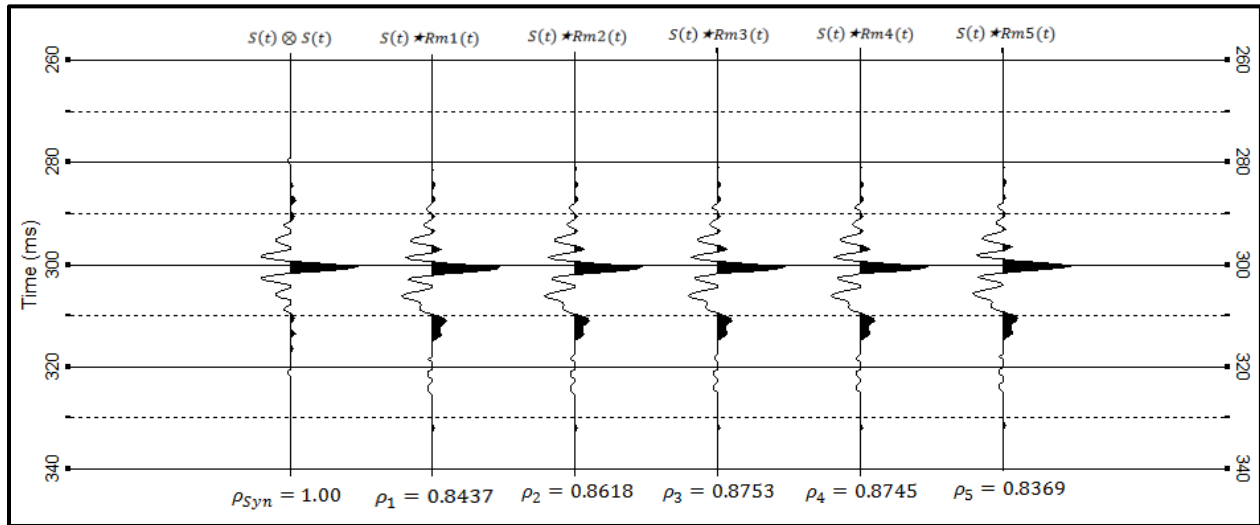


Figure 5.13. Autocorrelation of the synthetic sweep, $S(t) \otimes S(t)$, and correlation of synthetic with reaction mass, $S(t) \star R_{mi}(t)$, for each of the five sweeps when accelerometers are located at radial position 1 on rib (ρ = maximum correlation coefficient). Wavelets are bulk static shifted to 300 ms to easily display differences from the Klauder wavelet (autocorrelation of synthetic).

Table 5.3. Mean and standard deviation of the correlation coefficients between the CRL reaction mass accelerometer signal and the synthetic sweep for each source location

Source Location	Mean Correlation Coefficient, ρ_{mean}	Standard Deviation, σ_{total}
1	0.8632	0.0098
2	0.8369	0.0110
3	0.8483	0.0102

5.3.3. Response Variation due to Radial Position and Position with Respect to Baseplate Structure

At each radial position, accelerometer signals were collected with an accelerometer located on top of a reinforcement rib (on rib) and between reinforcement ribs (off rib). The CRL

reaction mass signal for the first set was correlated to the second set to ensure the consecutive sets of sweeps were comparable at each source location (Table 5.4). Since the correlation coefficients were almost identical ($> 99.8\%$) for each source location, it can be concluded that the baseplate traces from the consecutive sweep sets could be correlated to each other, and any observed response variations were associated with accelerometer position as opposed to sweep repeatability.

Table 5.4. Correlation of stacked reaction mass signals of consecutive five sweeps for each source location

Reaction Mass Correlation		Correlation Coefficient, ρ
SL 1		
Reaction Mass Signal 1 ★ Reaction Mass Signal 2		0.9983
SL 2		
Reaction Mass Signal 1 ★ Reaction Mass Signal 2		0.9986
SL 3		
Reaction Mass Signal 1 ★ Reaction Mass Signal 2		0.9999

Baseplate accelerometers in each radial position were cross-correlated with one another for both on and off rib accelerometer locations (Figure 5.5). The correlation coefficient between radial position 1 and radial position 3 displayed the least similarity. The correlation of accelerometers located at consecutive positions displayed the most similar correlation coefficients. Comparable results were obtained at each of the three source locations (Figure 5.14).

To determine the differences in baseplate accelerometer signals, phase and amplitude differences between the three radial positions were calculated for both on and off rib positions at each source location. Correlation phase plots were calculated by correlating each of the three radial positions to radial position 1 for each of the three accelerometer positions (Figure 5.15). To compare the amplitude differences associated with accelerometer radial positions, the

amplitude spectrum was calculated with respect to radial position 1 off rib at source location 1 (Equation 20):

$$A_{i_{db}} = 20 * \log_{10}(A_{RP_i}/A_{RP_1}) \quad \text{for } i = 1,2,3 \quad (20)$$

where i represents the radial position, $A_{i_{db}}$ is the amplitude ratio of radial position i expressed in decibels, A_{RP_i} is the calculated amplitude of accelerometer located at radial position i , and A_{RP_1} is the calculated amplitude of the accelerometer located at radial position 1 (Figure 5.16). This procedure was repeated for on and off rib radial positions at each source location (Figures C.1-C.10).

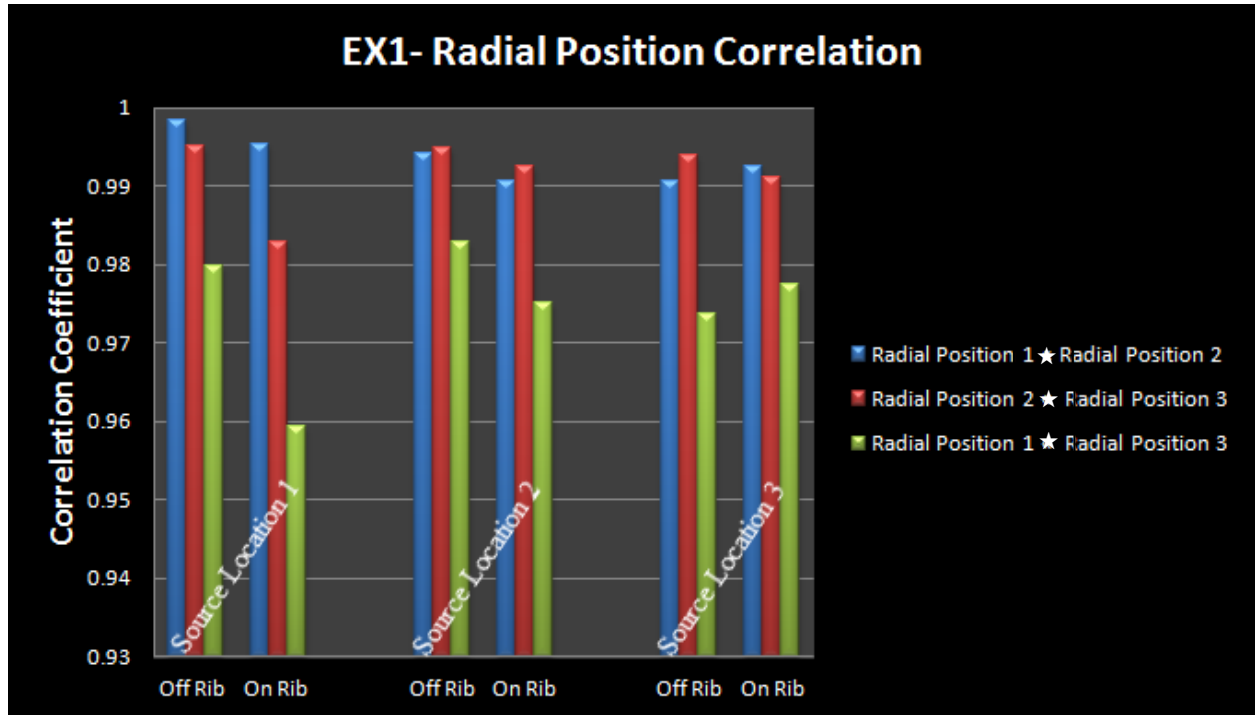


Figure 5.14. Correlation of signals from varying radial position for each source location in experiment 1.

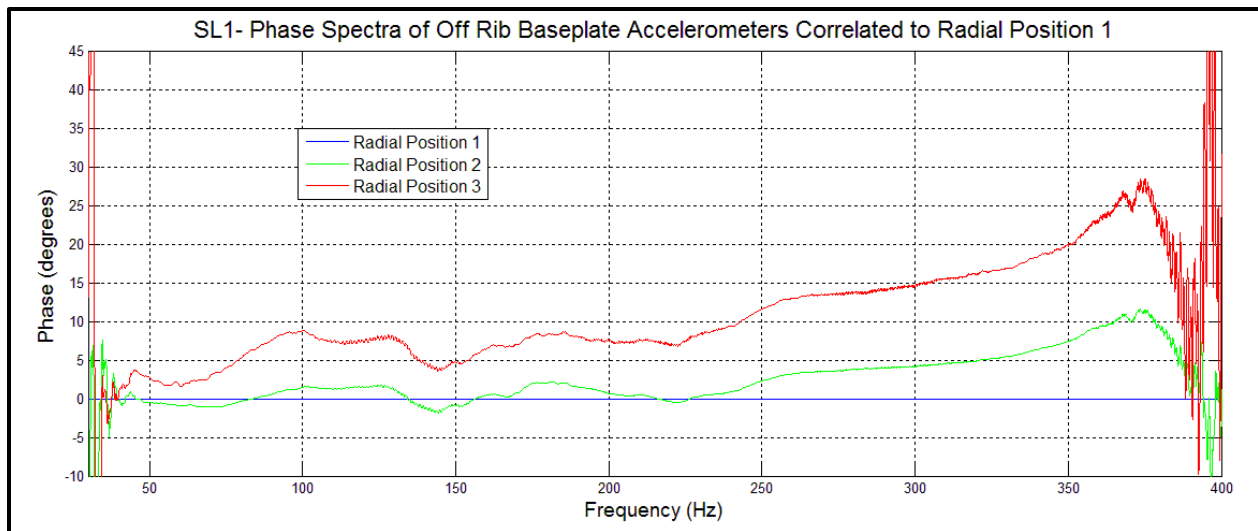


Figure 5.15. phase spectra of three off rib radial positions correlated to radial position 1 at source location 1.

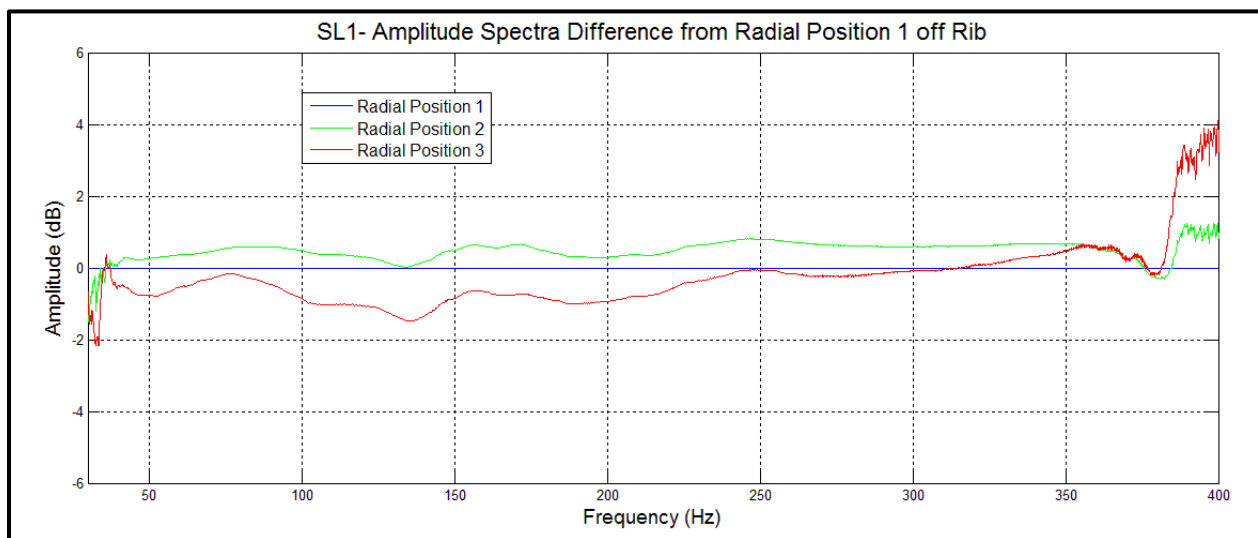


Figure 5.16. Amplitude ratio of three radial positions with respect to radial position 1 located off rib reinforcement for source location 1.

Additionally, the signal response differences associated with baseplate structure were examined by cross-correlating accelerometer response of each on and off rib radial position's (Figure 5.17). This analysis provided a quantitative measure of accelerometer response variability with respect to internal baseplate structure and a qualitative measure of accelerometer response variability related to radial accelerometer location.

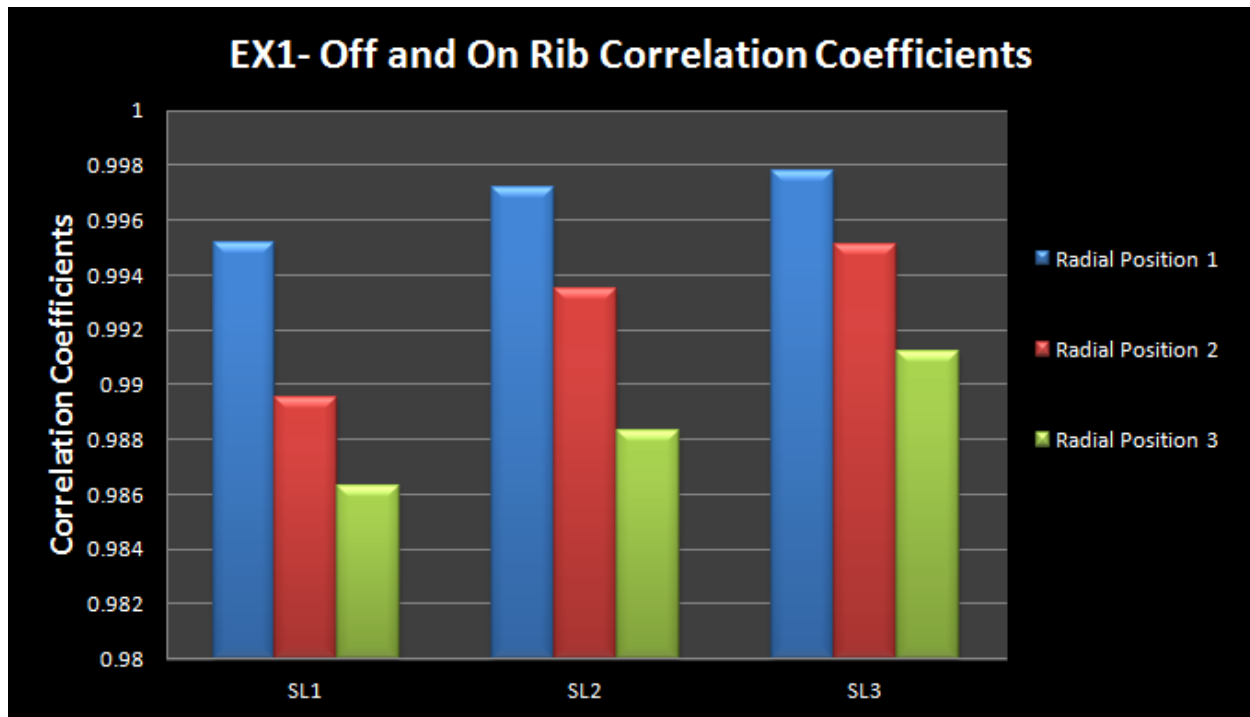


Figure 5.17. Correlation of on and off rib accelerometers at each of the three radial positions for each source location in experiment 1.

The response between on and off reinforcing ribs was very similar (correlation coefficients $> 98.5\%$) at each radial position for all source locations. However at each source location, the correlation between on and off rib accelerometers decreased with increasing distance from the center of the baseplate by up to 1%.

The differences in phase and amplitude between on and off rib accelerometer locations were calculated for each of the three radial positions. The correlation phase spectra was calculated for the off rib accelerometer with respect to the accelerometer located at the equivalent on rib radial positions for source location 1 (Figure 5.18). This procedure was repeated for source locations 2 and 3 (Figures C.11 and C.12).

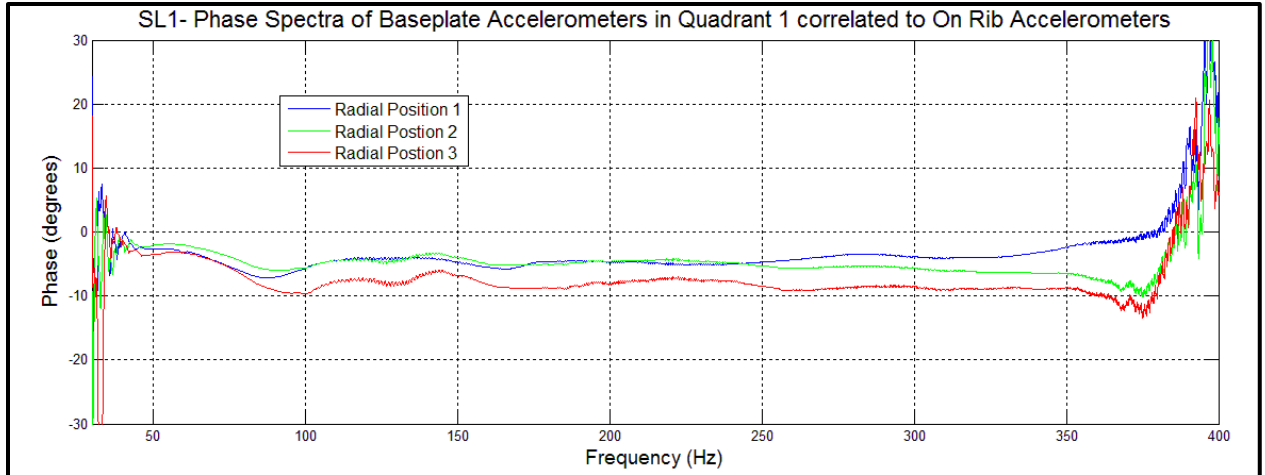


Figure 5.18. Phase difference between on and off rib accelerometers for each of the three radial positions at source location 1.

The phase variation between on and off rib accelerometers was fairly uniform throughout the sweep for source location 1. The variation between on and off rib accelerometers seems to depend on the frequency of the sweep at source location 2 and 3. Each of the phase plots show different trends at each of the three source locations. Variations in phase between on and off rib accelerometers increases for accelerometers located further away from the center of the baseplate for all source locations.

One approach to identify amplitude variations associated with differential rigidity in the internal baseplate structure is to calculate the amplitude spectrum of each accelerometer signal for the off rib accelerometer with respect to the accelerometer at the equivalent on rib radial position for each source location 1 (Figure 5.19, Figure C.13, and Figure C.14) (Equation 21):

$$A_{i_{db}} = 20 * \log_{10}(A_{off_i}/A_{on_i}) \quad \text{for } i = 1,2,3 \quad (21)$$

where i represents the radial position, $A_{i_{db}}$ is the amplitude ratio of off rib versus on reinforcing rib for radial position i expressed in decibels, A_{off_i} is the calculated amplitude of the off rib accelerometer located at radial position i , and A_{on_i} is the calculated amplitude of the on rib accelerometer located at radial position i .

The amplitude variation between on and off rib accelerometers for each source location depends on the radial position of the accelerometers and is between ± 2 dB. Although the amplitude variations between on and off rib responses is not significant, it is important to note that a difference in amplitude does exist at all source locations, and the amplitude difference increases with increased radial distance from the center of the baseplate.

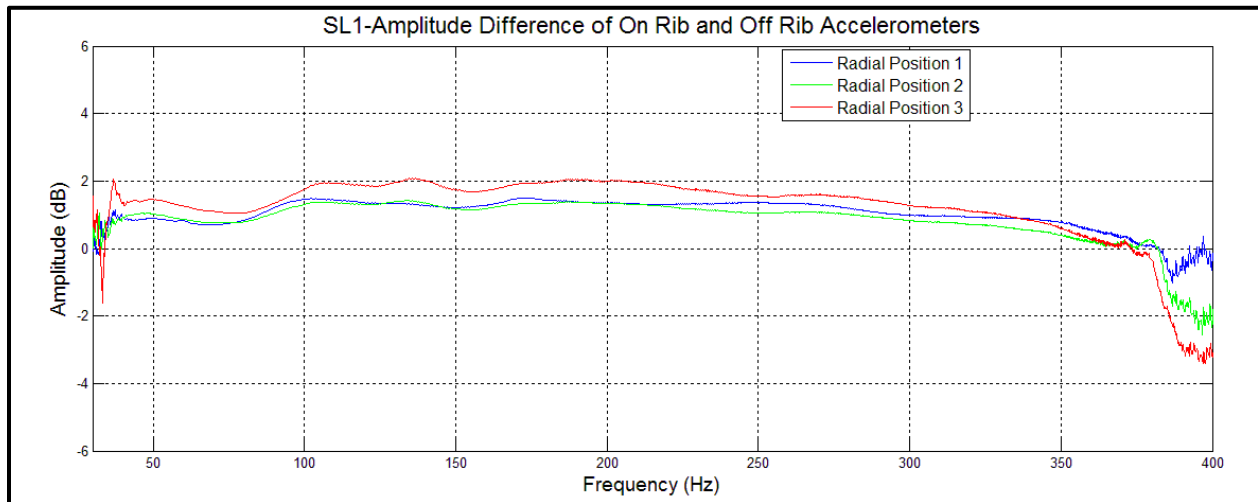


Figure 5.19. Amplitude difference between on and off rib accelerometers for each of the three radial positions at source location 1 displayed in dB.

5.3.4. Investigation of Baseplate Symmetry

Accelerometer data were acquired at each of the three radial positions both on and off internal rib reinforcement structures at each of the baseplate quadrants described in *Methods: Part 1*. Accelerometer signals acquired at equivalent positions in each quadrant were cross-correlated to establish a quantitative measure of similarity between the four quadrants and therefore overall baseplate consistency. A total of six correlations were performed for each of the accelerometer positions. A mean and standard deviation was computed for the correlations from the six accelerometer positions at all source locations (Figure 5.20). The mean correlation between the four quadrants decreased as the accelerometer position increased in distance away from the center of the baseplate for both on and off rib accelerometer positions at each of the

three source locations. The baseplate accelerometer located in quadrant 1 for off rib radial position 1 at source location 3 was loose during acquisition resulting in a low mean correlation coefficient. The correlation between the 4 quadrants decreased and variability between the correlations increased as the overall thickness of the baseplate decreased from center to rim.

To investigate whether the baseplate symmetry is dependent on source location, a mean correlation across the baseplate (using all correlations across the baseplate) was calculated for each source location. Additionally, the total standard deviation of the baseplate correlations was obtained for each source location. By comparing the mean correlation coefficient and corresponding standard deviation for each source location, it could be established that the baseplate symmetry is dependent on source location (Figure 5.21). The more rigid the near-surface conditions (source location 1- concrete) the larger the mean correlation across the baseplate. The largest variabilities were associated with loose near-surface conditions (source location 3- irregular semi-saturated alluvium) and the most asymmetric behavior across the baseplate.

To determine if the variability between accelerometer responses located in separate quadrants fell within the range of variability observed in the sweep for each source location, the standard deviation of baseplate quadrant correlations was compared to standard deviation of the sweep repeatability (Figure 5.22). The variability across the baseplate fell within the range of source variability for source location 1, which was collected on the most rigid and uniform near-surface conditions. The variability across the baseplate increased as the near-surface conditions become less rigid and the terrain became more irregular. For both source locations 2 and 3, the variability across the baseplate fell outside the source variability range. Therefore, the baseplate

has the ability to act symmetrically but that reaction depends on near-surface conditions directly beneath the baseplate.

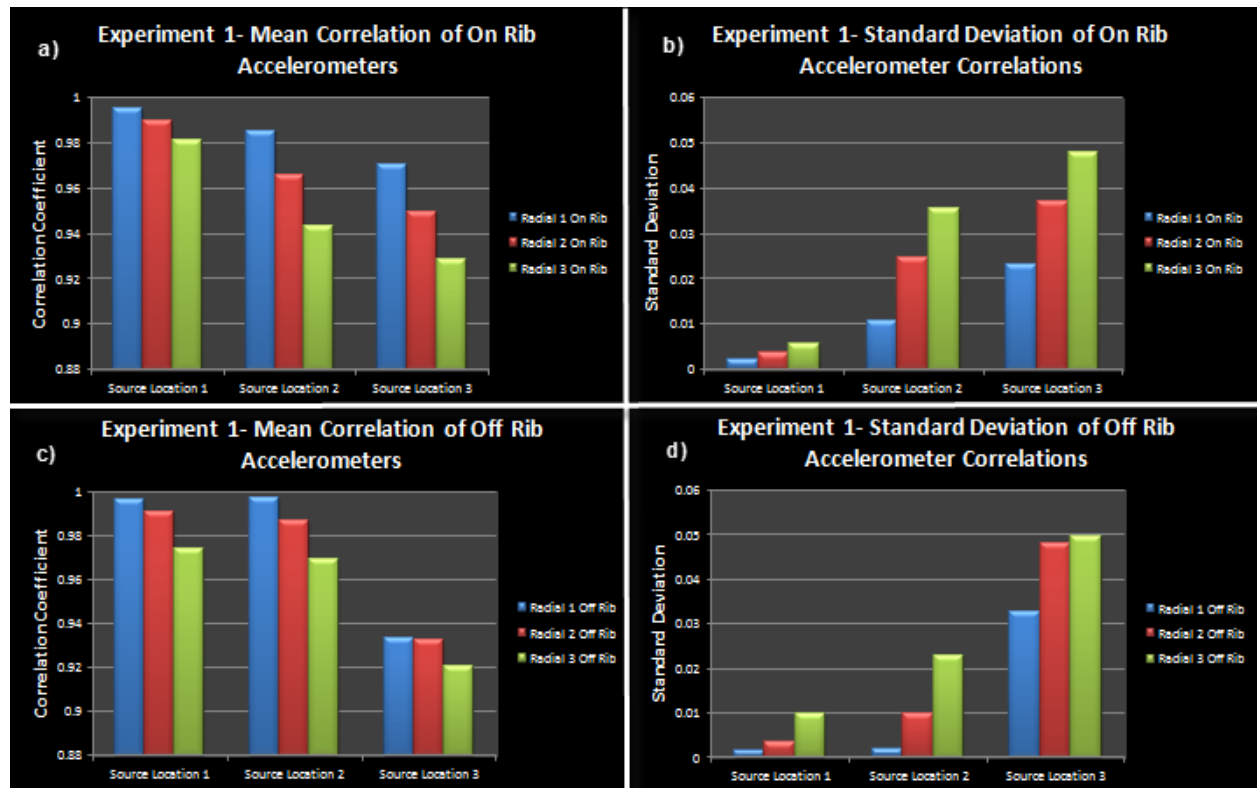


Figure 5.20. a) Mean and b) standard deviation of correlation coefficients between four quadrants for on rib accelerometer positions at each source location in experiment 1. c) Mean and d) standard deviation of correlation coefficients between four quadrants for off rib accelerometer positions at each source location in experiment 1.

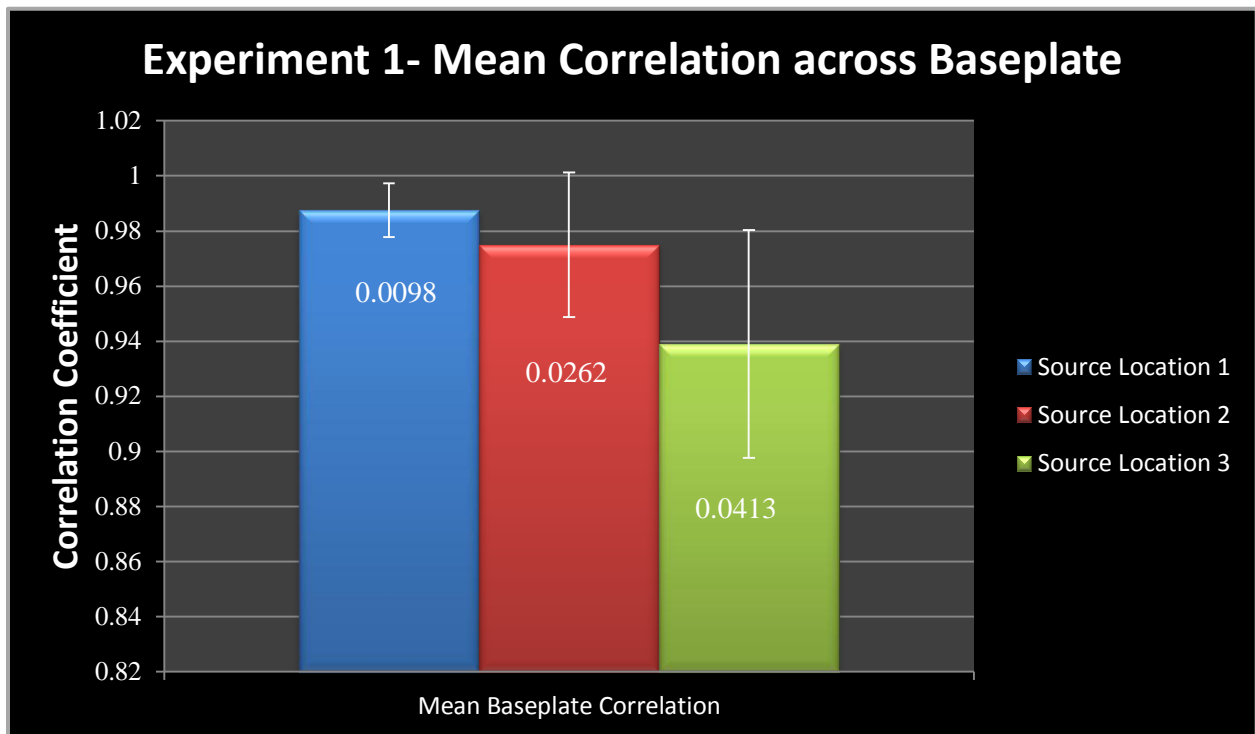


Figure 5.21. Mean correlation across baseplate for each of the three source locations. Standard deviation posted and displayed as error bars for each source location.

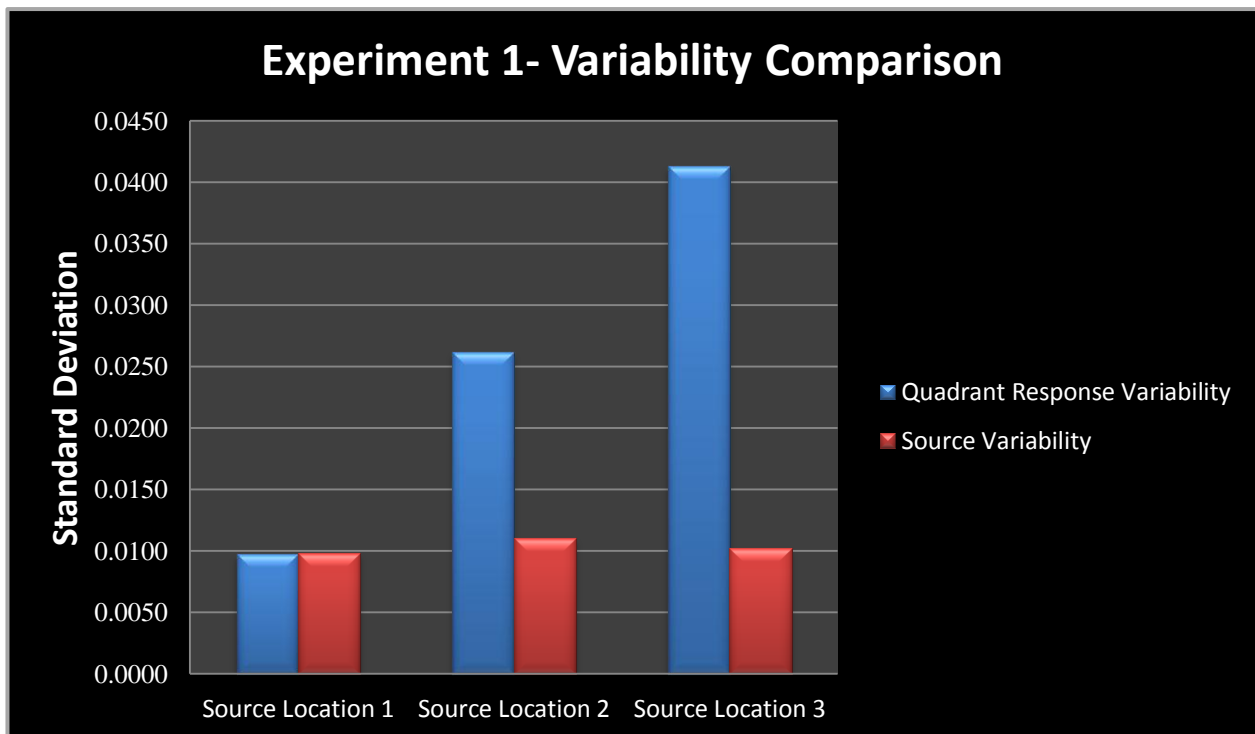


Figure 5.22. Comparison of quadrant response variability to source variability for each source location in experiment 1.

The correlation phase spectra were calculated for each on rib accelerometer position in quadrant 3 with respect to quadrant 1 to determine the phase difference for source location 1 (Figure 5.23). This procedure was repeated for source locations 2 and 3 (Figures C.15 and C.16). Correlation of the amplitude spectra of the accelerometer response were computed to identify any amplitude differences and their relative size in each quadrant with respect to quadrant 1 for source location 1, (Equation 22):

$$A_{i_{db}} = 20 * \log_{10}(A_{Q_i}/A_{Q_1}) \quad \text{for } i = 1,2,3,4 \quad (22)$$

where i represents the quadrant of accelerometer, $A_{i_{db}}$ is the amplitude ratio of quadrant i over quadrant 1 expressed in decibels, A_{Q_i} is the calculated amplitude of quadrant i , and A_{Q_1} is the calculated amplitude of quadrant 1. Amplitude and phase calculations were filtered using a 21-point moving average for plotting purposes (Figure 5.24). This procedure was repeated for source locations 2 and 3 (Figures C.17 and C.18). Differences in phase and amplitude between separate quadrants are present between each of the 4 quadrants at all source locations. The quadrants do not respond identically and therefore the baseplate exhibits asymmetric behavior throughout the duration of the sweep. Variations in phase and amplitude between the two quadrants confirm the baseplate's asymmetric response. At source location 3, the baseplate displays the greatest asymmetric behavior mainly due to the irregular surface beneath the baseplate. For each of the three source locations, the phase and amplitude differences are greater towards the edge of the baseplate where it is least rigid.

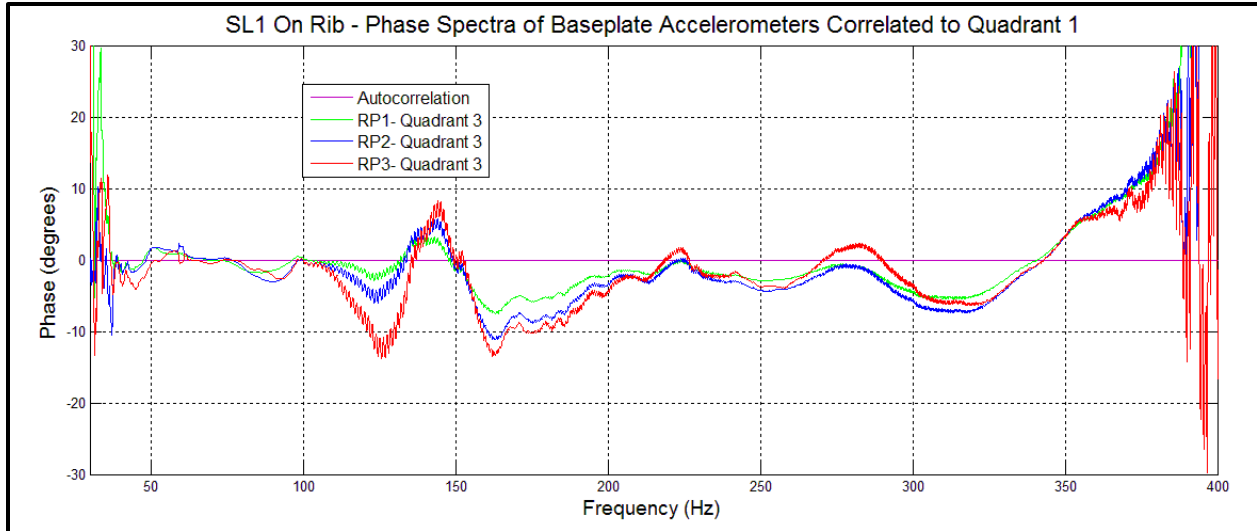


Figure 5.23. Phase spectra of quadrant 3 correlated with quadrant 1 for each radial position located on rib at source location 1.

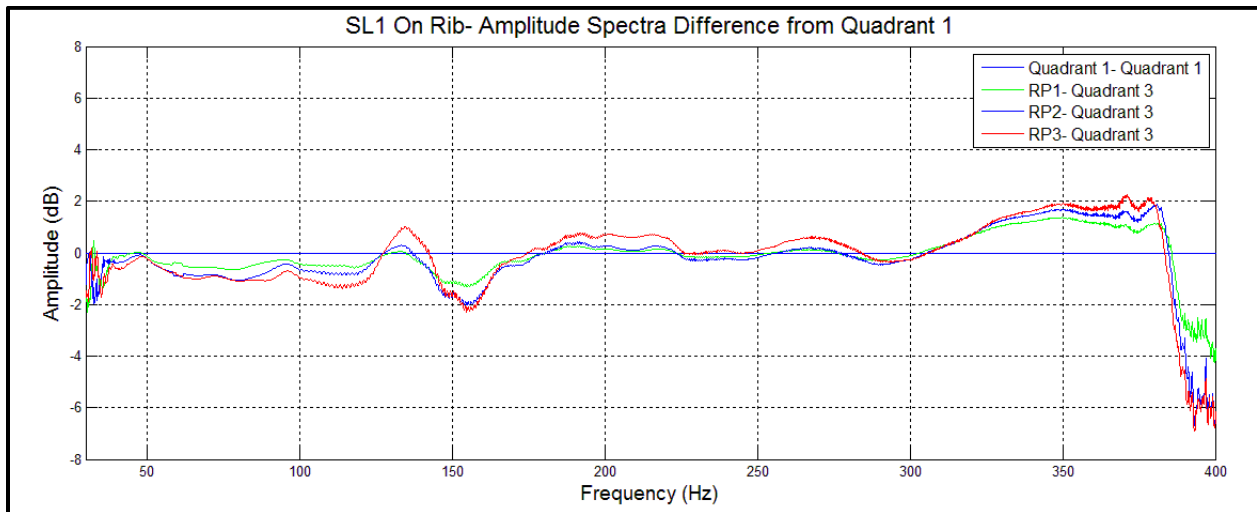


Figure 5.24. Amplitude spectrum difference plot of quadrant 3 from the amplitude spectrum of quadrant 1 for each radial position located on rib at source location 1.

5.3.5. Differences in Response Associated with Source Location

Theory suggests the vibroseis source signature will vary depending on the near-surface conditions located directly beneath the baseplate (Baeten, 1989; Sallas, 2010; Ziolkowski, 2010; Wei et al., 2011). To illustrate the changes of source signature related to varying near-surface conditions, analysis of the baseplate motion was done at three source locations. The three source locations were selected to provide variable surface terrain and near-surface rigidity. The absolute

peak ground force was calculated using the CRL accelerometer placed directly next to the Endevco accelerometers for each source location (Figure 5.25). Although the frequency range of the sweep was different between source location 1 and source locations 2 and 3, the change in frequency dwell-time, Δt , between the two sweeps is $< .002$ seconds and considered negligible for this comparison.

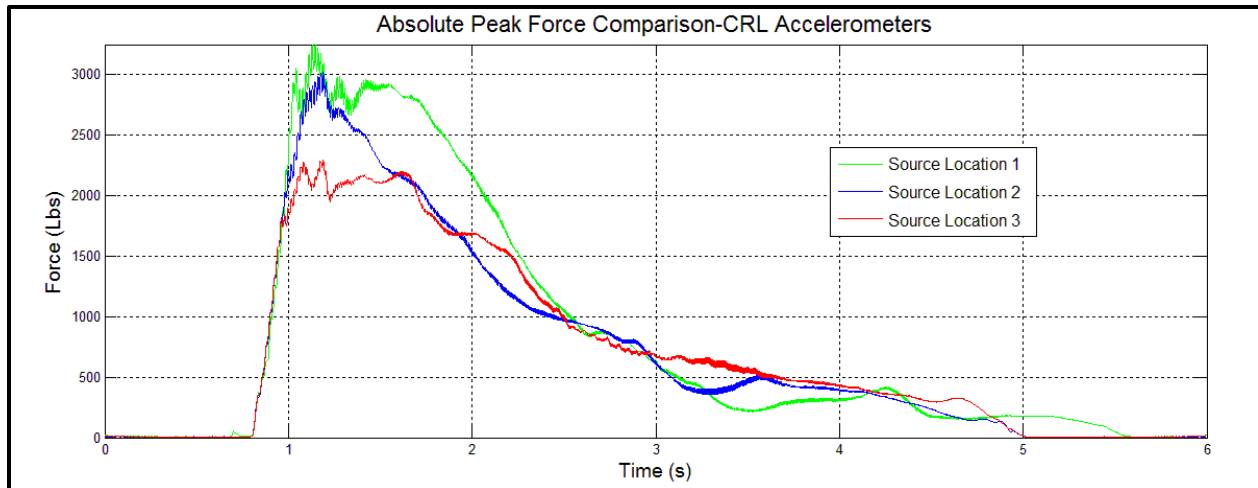


Figure 5.25. Absolute peak force comparison of three source locations calculated from CRL accelerometers. Source location 1 sweep parameters 5 second linear upsweep ranging from 30-400 Hz, Source Locations 2 and 3 sweep parameters- 5 second linear upsweep ranging from 30-450 Hz

Rigid near-surface conditions (source location 1- concrete) produced the largest absolute peak force. Each of the three source locations failed to output adequate energy for measuring force past 200 Hz. Each baseplate accelerometer signal was correlated to the respective reaction mass signal for each source location. The correlation phase spectra were calculated for the CRL accelerometers with respect to the signal recorded by the reaction mass accelerometer at each of the three source locations (Figure 5.26). The baseplate is approximately 160 degrees out of phase with the reaction mass at 200 Hz at the all three source locations.

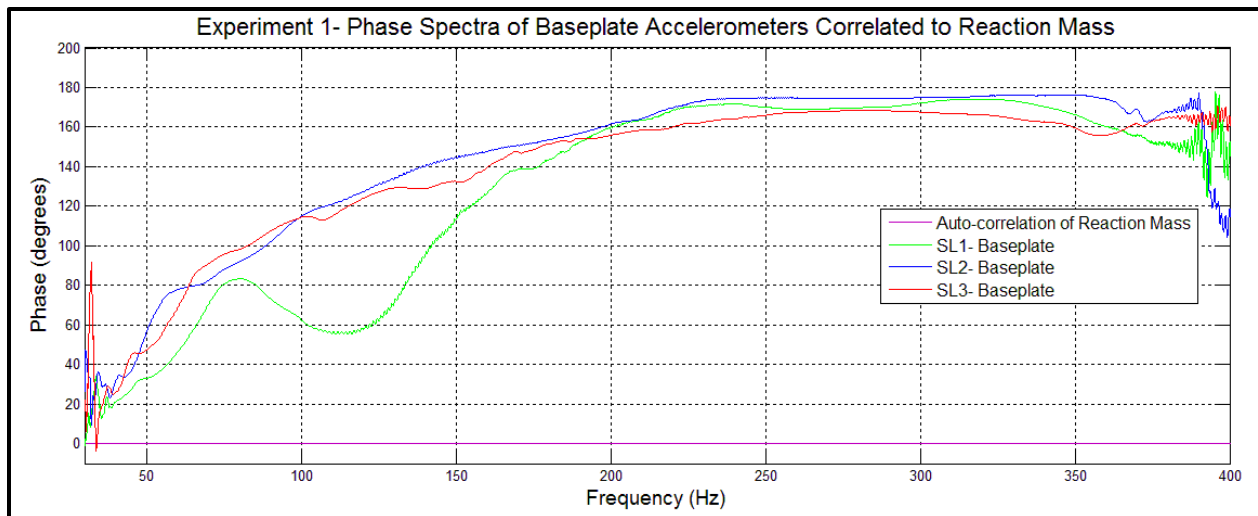


Figure 5.26. Correlation phase between CRL reaction mass and baseplate signals for each source location.

Variations in phase and amplitude were present between the four baseplate quadrants at each source location. The most uniform accelerometer response across the baseplate occurs on the uniform concrete surface (source location 1). Phase and amplitude variations increased at accelerometer locations positioned near the edge of the baseplate at all locations. Changes in accelerometer positions with respect to baseplate structure (on rib vs. off rib) resulted in smaller variations in phase and amplitude than changes in radial accelerometer position. Differences in response associated with baseplate structure were similar for each of the three source locations. Although each of the three source location exhibited similar trends, the source location with the least symmetric baseplate response (source location 3) displayed the highest correlations between on and off rib accelerometers at each of the three radial positions (Figure 5.17).

6. Discussion: Part 1; Investigation of Baseplate Motion

The baseplate did not react symmetrically during the sweep at any of the three source locations. Since all four accelerometers were placed at the same relative radial position in the 4 defined quadrants, changes in phase and amplitude between the 4 quadrants is most likely associated with asymmetric motion of the baseplate. For source location 1, the greatest variations in phase and amplitude occurred between 120-180 Hz (Figures 5.23 and 5.24). The abrupt changes in phase and amplitude within the frequency range of 120-180 Hz across the baseplate can be attributed to a resonant frequency between the baseplate and the ground at this particular source location (Schrodt, 1987). For source locations 2 and 3, when driven at high frequencies (> 200 Hz), the differences in phase across the baseplate increased (Figures C.15 and C.16) especially for accelerometers positioned towards the edge of the plate. Since the baseplate varies in thickness radially, this result is expected and directly attributed to the thinning of the baseplate at the edge of the plate. From the formula for flexural rigidity (Eq. B.4), rigidity is dependent on the thickness of the baseplate. The rigidity of the IVI Minivib I baseplate decreases with increasing distance from the center of the baseplate. When driven at higher frequencies (>200 Hz), baseplate flexure is most severe resulting in phase and amplitude variation across the baseplate (Sallas, 2010; Wei, 2010). Also, the external shell of the baseplate is equipped with weldments used to measure the baseplate motion for calculating ground force. These weldments could also be contributing to differential rigidity across the baseplate. Therefore, phase and amplitude differences across the plate could be in part attributed to an increase in baseplate flexure near the rim/edge.

There appears to be a connection between source terrain and asymmetric baseplate motion. Variability across the baseplate increased for less rigid and uneven surface terrain

(Figure 5.22). The baseplate response is adversely affected by rugged terrain because the vibrator baseplate is subjected to irregular baseplate flexure, creating an unpredictable distribution of pressure beneath the baseplate (Solodov, 1998; Levedev and Beresnev, 2004; Wei, 2010). Non-uniform distribution of pressure manifests areas of partial decoupling underneath the baseplate generating additional harmonic distortion (Wei, 2010). Since the least response variability across the baseplate occurred on a relatively flat rigid surface (concrete), it appears likely that a non-uniform contact with the baseplate and the ground contributed in part to response variability between the 4 baseplate quadrants at source locations 2 and 3.

When constrained to the response variability within a single quadrant, the greatest changes in phase and amplitude were observed between the three radial positions on the baseplate (Figures 5.15 and 5.16). The correlation coefficient between radial position 1 and radial position 3 possess the least similarity as a result of the two times larger distance between successive accelerometer positions (Figure 5.5). Response variability associated with radial accelerometer position is attributed to the baseplate's differential rigidity distribution. It is well known that accelerometer response will vary considerably across the surface of the baseplate (Levedev and Beresnev, 2005; Wei, 2009; Sallas, 2010; Wei et al., 2011).

Amplitude differences were greater between radial position 1 and radial position 3 most likely due to the change in baseplate thickness. However, the angle at which the accelerometers were off-vertical increased with the distance away from the center of the baseplate. Radial position 1 was $\approx 5^\circ$ off vertical and radial position 3 was $\approx 15^\circ$ off-vertical. The accelerometer response differs from a vertical accelerometer by cosine of the angle (Sill and Seller, 1999) and therefore, the amplitude response difference between the two accelerometer signals can be calculated by:

$$\Delta A_{dB} = 20 * \log_{10}(\cos_{RP1}(\alpha)) - 20 * \log_{10}(\cos_{RP3}(\beta)) \quad (23)$$

where ΔA_{dB} is the amplitude change associated with the angular difference between radial position 1 and radial position 3, α is the angle at which the accelerometer located at radial position 1 is off-vertical ($\approx 5^\circ$), and β is the angle at which the accelerometer located at radial position 3 is off-vertical ($\approx 15^\circ$). From this calculation, the maximum amplitude difference associated with increasing off-vertical accelerometer angle was ≈ 0.27 dB. As a result, the amplitude response variability can be attributed to variability in baseplate rigidity due to a decrease in baseplate thickness. The amplitude difference between the three radial position were minimal (< 2 dB) in comparison to phase variations.

Accelerometer response varied with on and off rib placement of baseplate accelerometers for each of the three source locations (Figure 5.17). These variations were minimal when compared to response variation associated with radial accelerometer position. As expected, the differences in phase and amplitude between on and off rib placement were greater towards the edge of the plate (Figures 5.18 and 5.19). From the internal baseplate structure (Figure 5.5), it is apparent that the circumferential distance between on and off rib accelerometers increased as the radial position of the accelerometer increased. This may explain the decrease in correlation coefficient between on and off rib accelerometer positions with increasing radial accelerometer position.

The baseplate and reaction mass signals became approximately 160 degrees out of phase at 200 Hz at each source location (Figure 5.26). Consequently at frequencies greater than 200 Hz, the accelerometer signals from the baseplate and reaction mass destructively interfere with each other when calculating ground force using the weighted-sum approximation. Since the baseplate weight and the reaction mass weight of the IVI Minivib I are similar, the resulting

force output at frequencies greater than 200 Hz is less than $1/6^{\text{th}}$ the maximum vibrator output and converge to zero force as the frequency of the sweep increases. In the time domain, this relationship results in minimal correlateable signal after 3 seconds into the sweep. Although the IVI Minivib I is advertised to produce “the broadest broadband available” spanning the frequency range of 10 to 550 Hz, the vibrator does not output any correlatable energy past 300 Hz.

As expected, the near-surface conditions significantly affected the vibrator output (Figure 5.25). Source location 1 produced the greatest maximum peak ground force because it represented the most rigid and level surface of the three tested locations. Although the vibrator produced the greatest peak force on the rigid surface, the approximate source signature at the rigid surface is more likely to contain harmonic distortion due to decoupling when compared to an even semi-elastic surface (Walters, 2009; Schrod, 1987; Reust, 1995). On a flat rigid surface, the vibrator hold-down weight provides a force that prevents the baseplate from completely decoupling, but due to baseplate flexure the local dynamic force can become greater than the local hold-down force resulting in partial decoupling (Wei et al., 2010). Harmonic distortion is not easily processed out of correlated data because strong harmonics have the ability to overprint the fundamental signal producing harmonic ghosts within the data (Schrod, 1987; Baetan and Ziolkowski, 1990; Wei, 2008a). For upsweeps, harmonic energy produces a distortion in the correlated records that appears as a forerunning noise train at each reflective interface characterized by oscillations about the fundamental frequency of the radiated signal (Seriff and Kim, 1970; Espey, 1988). However, upsweeps should be used to avoid interference between late reflections and the distortion signals from strong early events (Seriff and Kim, 1970; Li et al., 1995).

Many acquisition and pre-processing techniques have been developed to reduce the harmonic energy present in the correlated vibroseis data with varying degrees of effectiveness (Rietsch, 1981; Schrodt, 1987; Li et al., 1995). Ideally, deconvolving the raw data with an accurate ground force approximation will remove the harmonic energy because the harmonic energy is contained within the source signature (Li, 1997; van der Veen et al., 1999). Because of this, it is strongly advised to collect each accelerometer trace and uncorrelated raw seismic separately during acquisition.

As previously stated, the IVI Minivib I generated a non-uniform response most likely attributed to inadequate baseplate rigidity especially towards the edge/rim of the baseplate. Baseplate flexure produces source generated harmonic energy that is not representative of energy being transferred into the ground and therefore, source generated harmonic distortion will decrease the accuracy of the ground force approximation (van der Veen et al., 1999; Saragiotis et al., 2010; Wei, 2010). Increasing the baseplate rigidity will reduce the effect of source generated harmonic distortion. Theoretically, increasing the baseplate rigidity for the IVI System can be obtained by designing a new uniformly thick baseplate with a smaller diameter.

7. Conclusions: Part 1; Investigation of Baseplate Motion

The IVI Minivib I baseplate responds non-uniformly and unpredictably across the baseplate surface to the reaction mass drive energy. Asymmetric baseplate motion about the origin of the baseplate is apparent towards the edge of the plate where the baseplate is the least rigid. Consequently, the most cylindrically symmetric baseplate response is seen towards the center of the baseplate. When the baseplate is subjected to flexure vibrations, the placement of the baseplate accelerometer at different locations on the plate will produce different ground force approximations (Levedev and Beresnev, 2005; Wei, 2009; Sallas, 2010; Wei et al., 2011). The magnitude of response variability increased with increasing sweep frequencies due to baseplate flexure (Sallas, 2010; Wei, 2010). Furthermore, the baseplate response becomes increasingly asymmetric relative to the origin of the baseplate when subjected to near-surface conditions which contribute to poor source coupling. Therefore, the IVI Minivib I baseplate does not act a point source for generation of seismic energy. When subjected to baseplate flexure, the baseplate moves differently in response to ground- related nonlinearities resulting in an inaccurate ground-force approximation at high frequencies due to harmonic distortion (Wei, 2008a).

Although the response is non-uniform across the baseplate due to baseplate flexure, optimal accelerometer locations can be determined by examining the approximate ground force to the true vibrator output (Wei, 2009). It is most likely that placement of multiple accelerometers will be necessary to average the baseplate motion and more closely measure true baseplate motion. Averaging the baseplate motion with multiple accelerometers, should

effectively measure differences in response across the baseplate due to differing near-surface conditions.

The design of the IVI Minivib I manifests two major complications true to recording device motion and therefore the source wavelet: (1) when driven at high frequencies, the baseplate experiences flexure causing a non-uniform distribution of pressure underneath the baseplate resulting in harmonic energy being present within the ground force estimation; (2) The baseplate and reaction mass approach 180 degrees out of phase at 200 Hz resulting in minimal ground force output to the ground. Although the first major complications has been shown for conventional seismic vibrators (Levedev and Beresnev, 2005; Sallas, 2010; Wei, 2010), this result has not been observed for commercial high frequency seismic vibrators. To reduce the affects of baseplate flexure, the rigidity of the baseplate must be increased to improve the vibrator output for high frequency applications. The weighted-sum approximation will inherently be limited to some degree by the rigid body assumption since an infinitely stiff baseplate is unattainable. Additionally, a more rigid baseplate could greatly minimize complication (2). Increasing the weight of the baseplate is another measure that may mititigate complication (2). By increasing the weight of the baseplate, the forces produced by the baseplate and reaction mass will not completely cancel each other in the ground force approximation when using the weighted-sum method.

8. Methods: Part 2; Optimizing Ground Force Approximation

8.1. Purpose Statement

An experiment was designed to determine the optimum accelerometer model for collecting the true source signature, to determine the optimal number and location of baseplate accelerometers to most accurately estimate the ground force output using the weighted-sum approximation, and to evaluate the quality control system and associated feedback signal for the IVI Minivib I. For conventional exploration seismic vibrators, the weighted-sum approximation tends to overestimate the true ground force at high frequencies (> 150 Hz) (Baeten and Ziolkowski, 1990; Allen et al., 1998; Sallas, 2010). Also, it has been shown that the weighted-sum approximation using one baseplate accelerometer and one mass accelerometer is a poor representation of true ground force delivered to the ground by a seismic vibrator. A better approximation can be achieved by using measurements from multiple accelerometers on the vibrator baseplate for calculating an augmented weighted-sum (Sallas, 2010; Wei, 2010). By collecting the distribution of pressure beneath the baseplate using the Load Cell System simultaneously with an array of accelerometers, this experiment will identify a better approximation for the energy delivered into the ground by the Minivib I.

8.2. Data Acquisition

Data acquisition occurred north of the Lawrence, KS offices of the Kansas Geological Survey and approximately 6 m (20 ft) away from a 122 m (400 ft) deep test wellbore (Figure 8.1). Data from this experiment was only collected at one source location, which corresponded to source location 2 in *Methods: Part 1*. Although the source location was located near three roads, traffic noise should not degrade the data collected in this experiment. The IVI Minivib I source generated a 5 second linear upsweep with a frequency range of 30-450 Hz (Table 5.1). Signals

from all three model accelerometers were collected during each sweep to compare ground force spectral characteristics. In addition, these signal's spectral characteristics and approximate ground force signals were compared to true ground force collected by the Load Cell System during each sweep.



Figure 8.1. Source location for Part 2

Five CRL magnetic mount accelerometers were used in this study. One accelerometer was positioned on the vibrator reaction mass throughout the survey. Fifteen different locations were tested on 8 different baseplate positions (Figure 8.2). Both the number of active accelerometers and the position of the active accelerometers were varied to create the fifteen tested locations. For each different accelerometer location, data was recorded as the Minivib generated 3 five-second linear upsweeps with a frequency range of 30-450 Hz. All three accelerometer signals and load cell signals were collected during each sweep.

Two of the fifteen CRL accelerometer locations occupied on the baseplate coincided with the Endevco baseplate accelerometer location and the Dytran baseplate accelerometer location. These locations were tested to allow direct comparison of the signal characteristics from each of the models. In addition, it allowed a direct comparison of the weighted-sum estimate from each of the three accelerometer models to the true ground force calculated by the load cells.

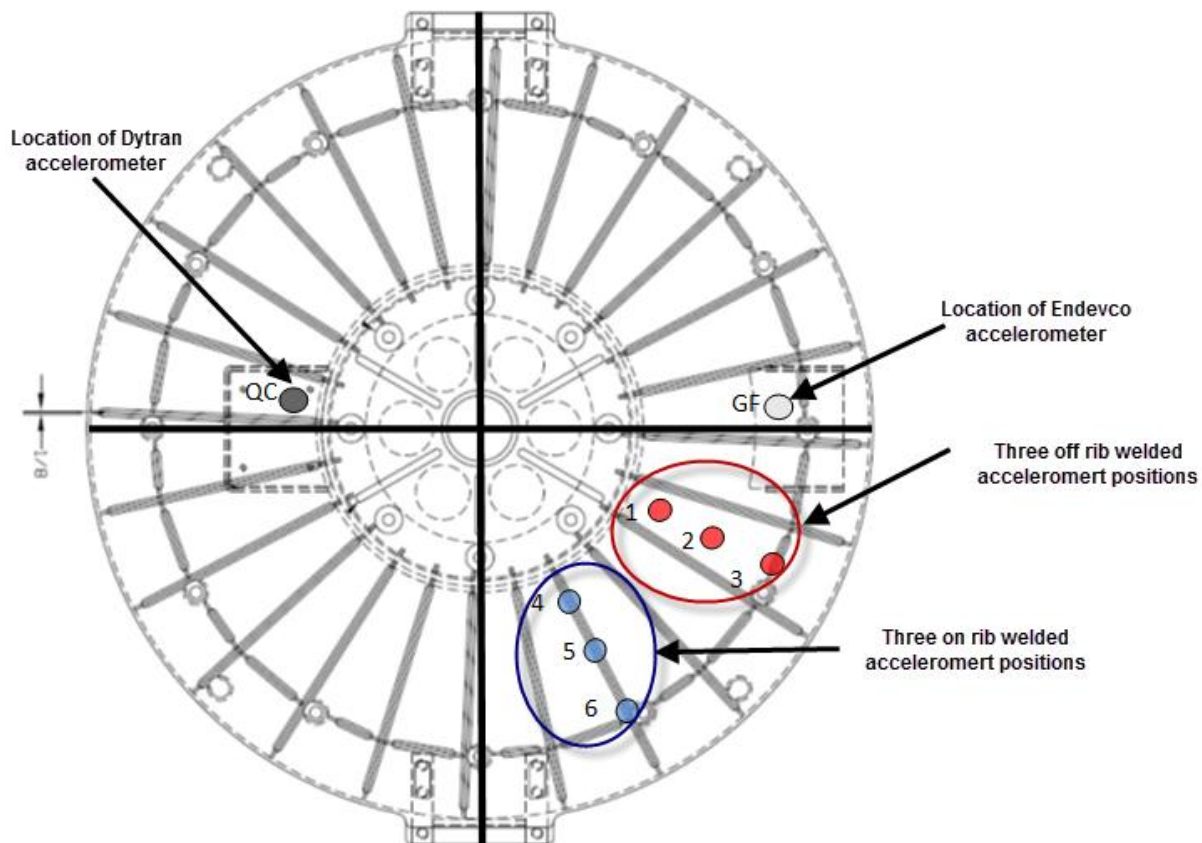


Figure 8.2. Schematic of 8 different accelerometer positions tested. GF corresponds to the location of the Endevco accelerometer position currently used by KGS to calculate ground force. QC corresponds to location of Dytran accelerometer that is used by IVI vibrator quality control.

Six additional accelerometer positions were welded onto the baseplate to test for the optimum ground force calculation. They were located in quadrant 1 of the baseplate and corresponded to the on and off reinforcement rib locations in each of the three radial positions occupied during part one of this study. Six of the fifteen locations were tested by placing a single

CRL accelerometer at each of the six welded plate locations. The remaining 7 locations used all four accelerometers placed on specific combinations of the six welded plate positions (Table 8.1).

Table 8.1: Accelerometer location combinations using 4 baseplate accelerometers with each accelerometer's corresponding welded positions

Location combinations using 4 baseplate accelerometers		Welded positions
	1	1, 2, 3, 5
	2	1, 2, 4, 6
	3	1, 2, 5, 6
	4	1, 3, 4, 6
	5	1, 3, 5, 6
	6	2, 3, 4, 6
	7	2, 4, 5, 6

An augmented weighted-sum ground force was calculated using the four CRL baseplate accelerometers and the CRL reaction mass accelerometer for each combination of locations. Each augmented weighted-sum was compared to the true ground force measured by the load cells. The location combinations were selected based on accelerometer performance seen in *Part I* of the survey.

The load cell plates were strategically positioned so the maximum number of individual load cell sensors were underneath the vibrator baseplate (Figure 8.3). Six load cell signals were collected during acquisition. Sensors A and B on load cell 1 and Sensor C on load cell 3 were not functioning properly; therefore, they were not acquired. The true ground force signal, which is calculated by integrating the pressures beneath the vibroseis baseplate, was collected during each sweep to evaluate differences between the true ground force and the three ground force approximations calculated using the different accelerometer models (Mewhort et al., 2002).

Downhole geophone data was collected simultaneously during each sweep with the load cell data and the accelerometer data. The downhole geophone was initially placed 50 ft from the surface. After all 15 combinations were collected, the downhole geophone was incremented 50 ft and all data was recollected until the depth reached 400 ft. Data was collected to compare the response with both approximate and true ground force calculations and to determine at which depth the subsurface responds as a homogenous elastic body. After acquisition, it was determined that the downhole data was not suitable for this application due to the low signal strength. The signal strength was low due to equipment malfunction related to the downhole geophone being partially disconnected from the takeout cable.

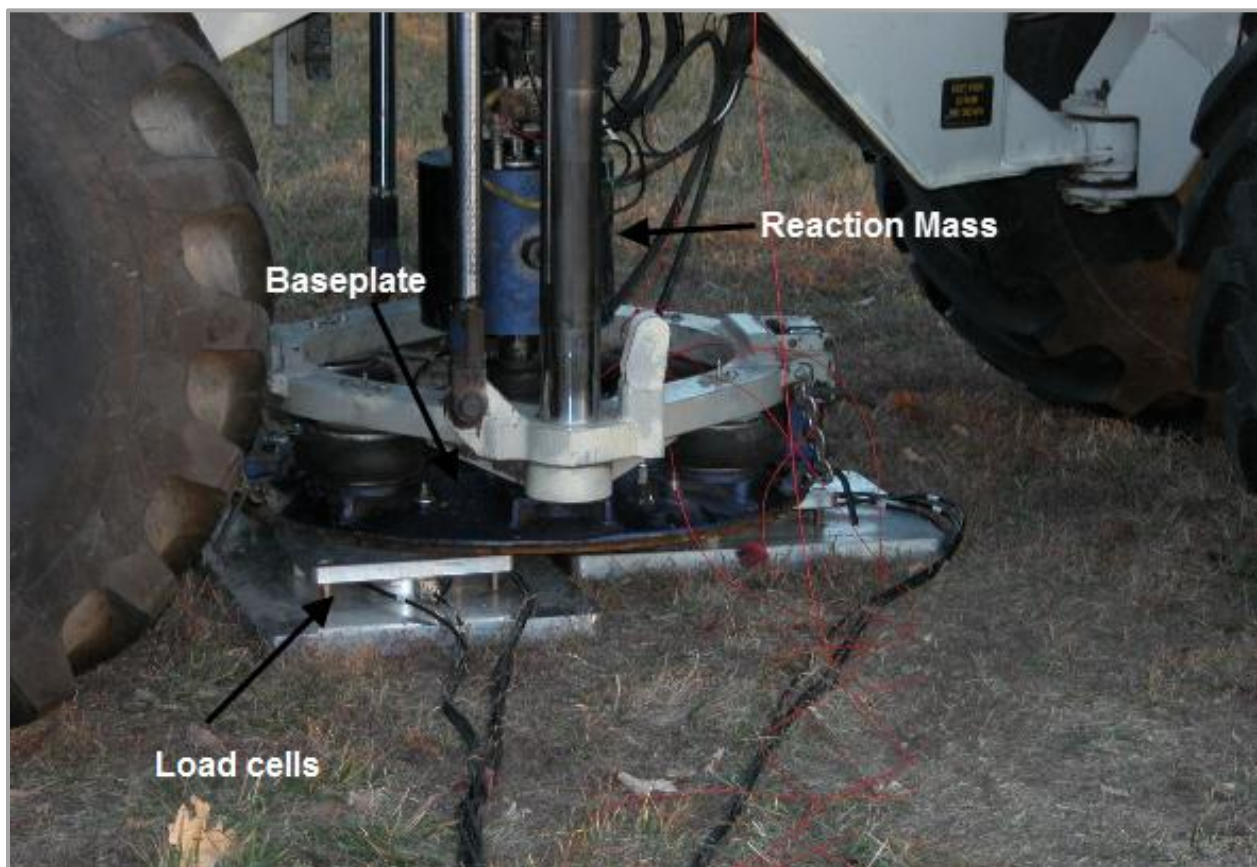


Figure 8.3. Location of load cells beneath the baseplate

8.3. Data Analysis

Simultaneous collection of baseplate and mass accelerometer data and Load Cell System data allowed direct comparison of approximate source signatures with actual measured ground force. The Load Cell System measures the direct force output by integrating the pressure beneath the vibrator baseplate. These comparisons were key to establishing an optimum position(s) and location(s) of baseplate accelerometer(s) to most closely approximate ground force (Sallas, 2010). However, when using the Load Cell System, the contact area between the load cells and the baseplate does not equal the area of the baseplate. As a result, the coupling between the baseplate and the ground surface becomes a point load at each load cell resulting in a resonance frequency that does not exist if the contact area is equal to the baseplate area (Wei et al., 2010). Furthermore, the performance of the IVI vibrator quality control system was analyzed permitting the selection of an optimum accelerometer model.

Although triggered at the same time during acquisition, each of the three accelerometer data sets were recorded on separate systems and therefore resulted in a time-lag between each of the signals. It was necessary to shift time zero to compensate for inherent lags in the recorded energy allowing a quantitative measure of similarity between the accelerometer signals (Figure 8.4). For both the Endevco and Dytran accelerometer models, their reaction mass, baseplate, and ground force signals were shifted to their respective CRL equivalent. The proper shift was dictated by the maximum correlation coefficient between the two signals. This shift was determined by cross-correlating the time-lagged signals for each record and applying the time shift that resulted in the maximum correlation coefficient. This shift equates to the time between the maximum correlation value and time-zero.

All spectral analysis plots were initially filtered using a 21-point moving average and due to lack of sufficient amplitude > 380 Hz, a frequency range of 30-400 Hz for display purposes was used.

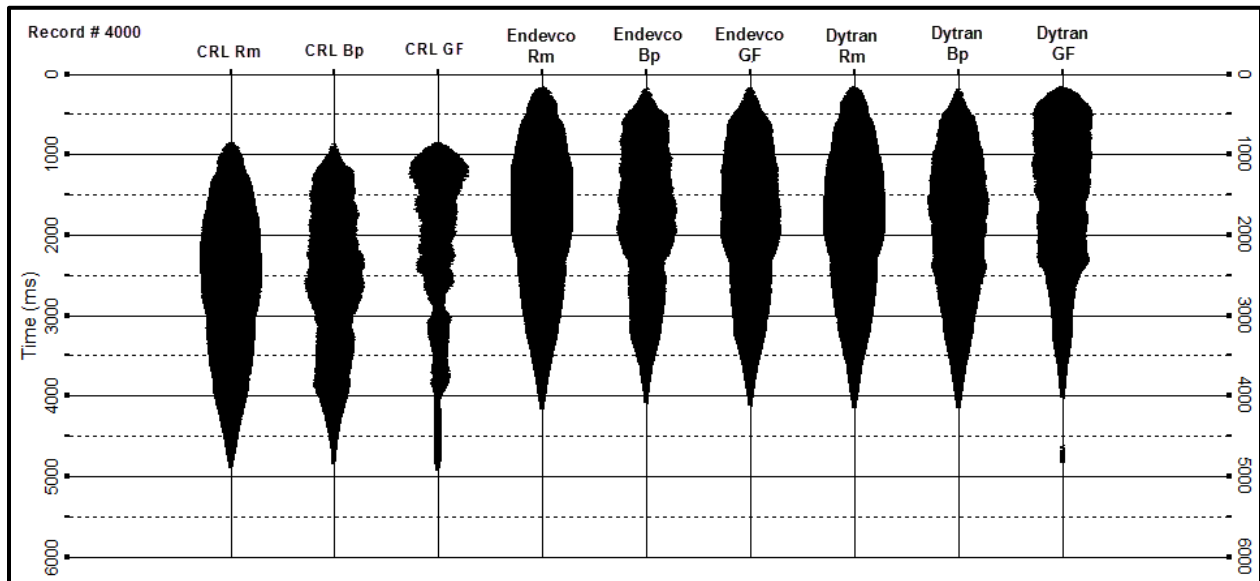


Figure 8.4. Unshifted accelerometer signals with corresponding calculated ground force traces for stacked Record # 4000.

8.3.1. Sweep Repeatability

Sweep repeatability is a critical metric for evaluation vibrator performance and effectiveness of the method at a particular site. The CRL accelerometer response for the reaction mass was cross-correlated with the ideal signal (synthetic sweep) to determine the consistency of the vibrator output. The standard deviation of the correlation coefficients was small ($\approx 1\%$). It is reasonable to suggest the vibrator sweeps acquired for this experiment were repeatable. Each of the 15 CRL baseplate accelerometer locations, therefore, was evaluated after stacking their corresponding three individual sweeps, increasing the signal-to-noise ratio for each tested accelerometer location.

8.3.2. Evaluation of the Feedback Signal

The accuracy and quality of the feedback signal for the IVI Minivib I was evaluated by studying the computed ground force using the weighted-sum of the stacked Dytran reaction mass and baseplate signals (Equation 7). Amplifier noise and a DC-bias was present on each ground force trace recorded by the IVI vibrator control system. The ground force recorded by the factory control system does not accurately represent the ground force signal and required trace conditioning by filtering the ground force traces with a 5-10 Hz low-cut filter (Figure 8.5).

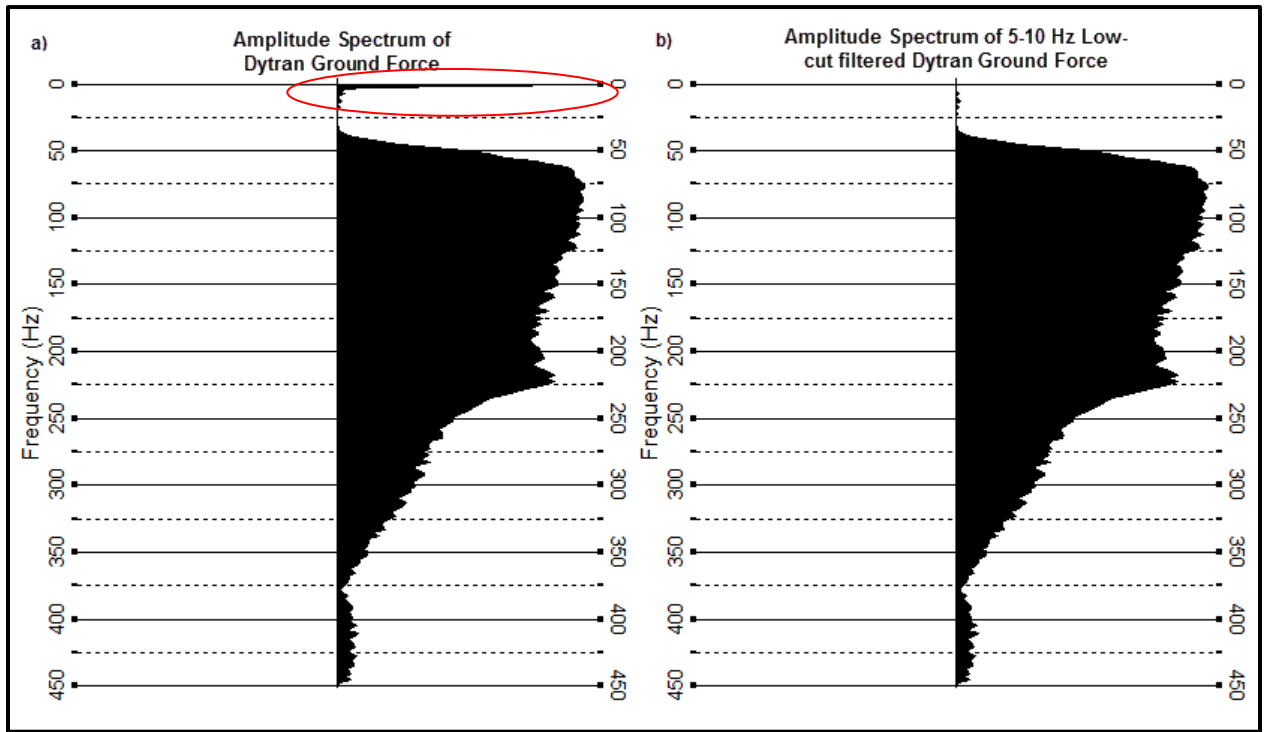


Figure 8.5. a) Amplitude spectrum of Dytran ground force signal with amplifier noise circled in red. b) 5-10 Hz Low-cut filtered amplitude spectrum of Dytran ground force.

The true ground force (measured by the Load Cell System) was calculated using the six individual load cell signals located underneath the baseplate (Equation 24):

$$TGF = (LC_1 + LC_2 + LC_3 + LC_4 + LC_5 + LC_6) \cdot C_{LC} \cdot S_{LC} \quad (24)$$

where TGF is the true ground force (lb-force), LC_i is the individual load cell signal (volts, V), C_{LC} is capacity of each load cell (g-force, g), and S_{LC} is the reciprocal of the accelerometer

sensitivity (g/V). True ground force traces were calculated for all stacked records collected in experiment 2.

Variability of true ground force measurements collected by the Load Cell System must be examined to evaluate the factory feedback signal and to optimize the source signature approximation. Each true ground force trace was cross-correlated with the first stacked record to determine the consistency of the Load Cell System. The standard deviation of the correlation coefficients was $\approx 1\%$ and therefore it is reasonable to optimize source operations using the true ground force signals.

The Dytran ground force traces were cross-correlated with the corresponding true ground force traces. The mean of the correlation coefficients between the true ground force trace and the Dytran ground force trace was 88% with a standard deviation of 4.19 %.

A total of 8 stacked records were collected with a single CRL baseplate accelerometer positioned directly beside the factory Dytran baseplate accelerometer. The ground force outputs from the Dytran and CRL accelerometers were correlated with the corresponding true ground force to establish a quantitative measure of similarity between the respective ground force traces and the true ground force. The mean and standard deviation of the maximum correlation coefficients for each accelerometer model was computed to compare the accuracy and precision of each model. The mean correlation between the CRL ground force and the true ground force was 97.6%, which was $\approx 9\%$ greater than the mean correlation between the Dytran ground force and the true ground force. Additionally, the correlations between the CRL ground force and the true ground force had a standard deviation of 0.2% and the correlations between the Dytran ground force and the true ground force had a standard deviation of 4%.

The correlation phase spectrum (Figure 8.6) of the Dytran and CRL ground force signals was compared to the phase of the true ground force. The amplitude spectrum of each approximated ground force signal was also contrasted with the true ground force (Equation 25):

$$A_{GF_i db} = 20 * \log_{10}(A_{GF_i}/A_{TGF}) \quad \text{for } i = 1, 2, 3 \quad (25)$$

where i represents the accelerometer model (1 = CRL, 2= Dytran, 3 = Endevco), $A_{GF_i db}$ is the amplitude ratio of the approximate ground force over true ground force expressed in decibels, A_{GF_i} is the calculated amplitude of the ground force for accelerometer model i , and A_{TGF} is the calculated amplitude of the true ground force (Figure 8.7). In addition, the absolute peak force of both ground force signals was compared to the absolute peak force of the true ground force collected using the Load Cell System (Figure 8.8).

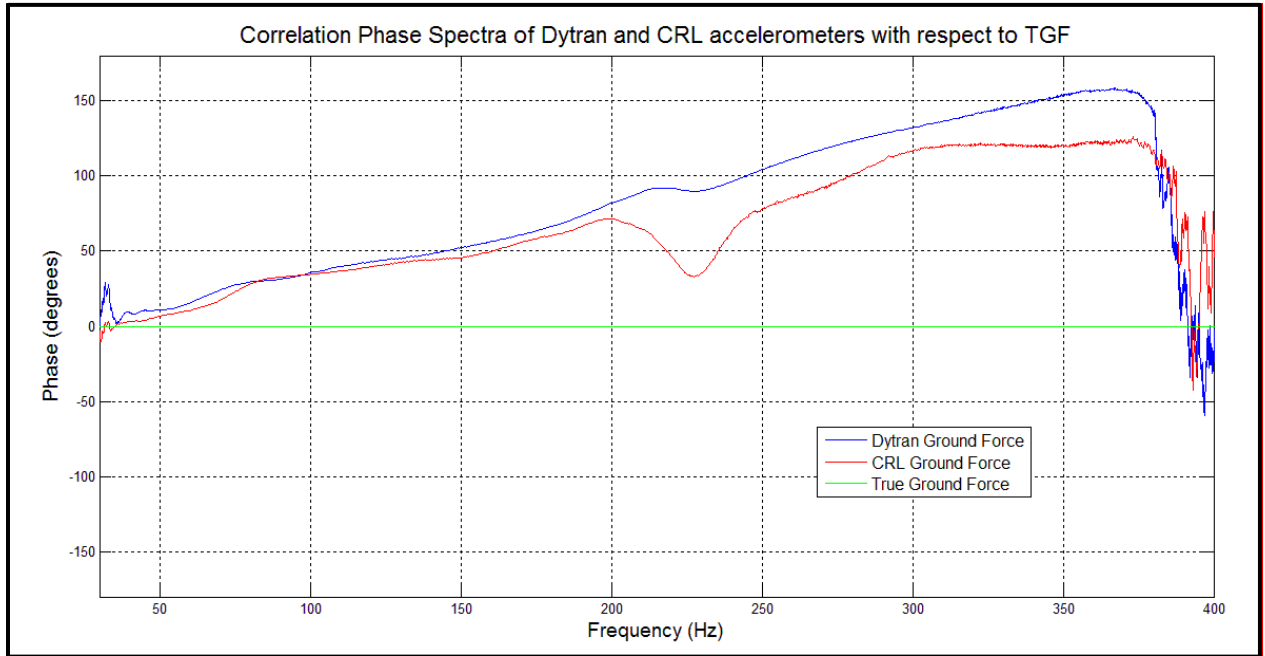


Figure 8.6. Phase spectra of the Dytran and CRL ground force correlated with the true ground force.

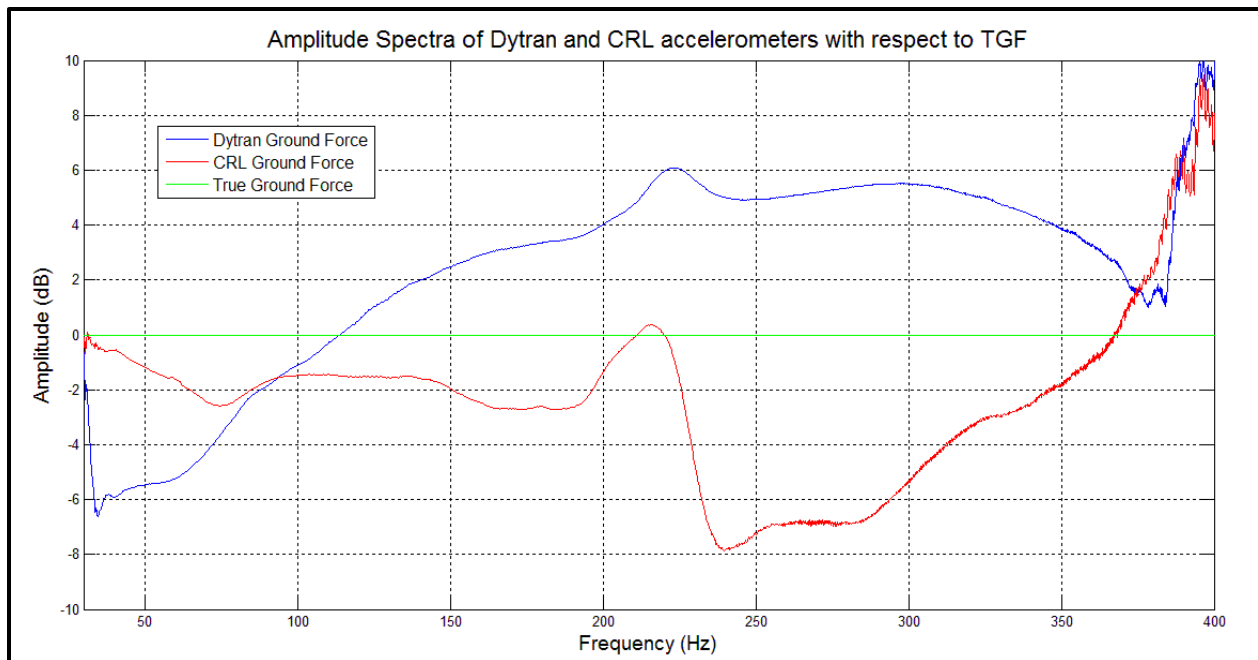


Figure 8.7. Amplitude difference between calculated Dytran and CRL ground force and the true ground force displayed in dB.

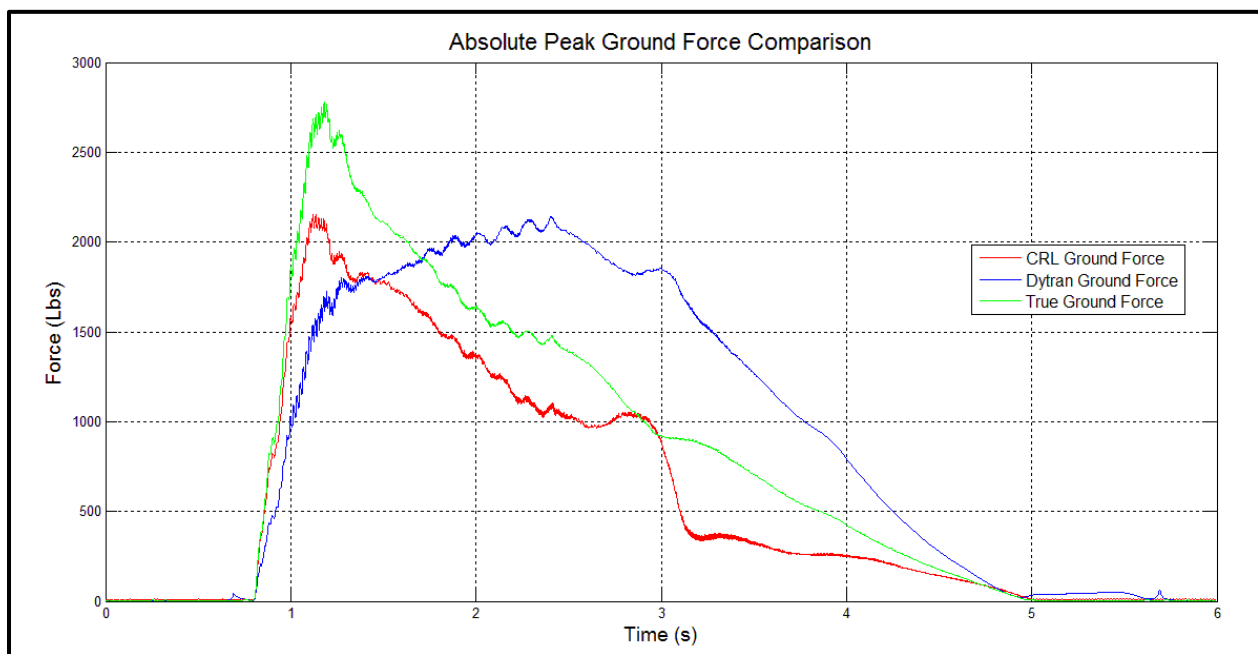


Figure 8.8. Absolute peak force comparison of the Dytran and CRL ground force to the true ground force.

8.3.3. Determination of Optimal Accelerometer Model

Maximum correlations were calculated between the Dytran and the true ground force to establish how well the factory equipment performed, but Rademacker (2006) established that from a signal to noise perspective the Dytran accelerometer model is inferior to the Endevco accelerometer model. Therefore in an effort to determine the optimal accelerometer model for calculating ground force, the CRL accelerometers were compared to the Endevco accelerometers.

For the sweeps at which the accelerometers were positioned side-by-side, each model's calculated ground force was cross-correlated with the corresponding true ground force trace to determine which accelerometer model produced the most representative ground force output. The mean and standard deviation of each of the maximum correlation coefficients were computed. The mean correlation between the Endevco ground force and the true ground force was 91%, which was only 0.9% greater than the mean correlation between the CRL ground force and the true ground force. However, the standard deviation of correlations between the Endevco ground force and the true ground force was 1.6%, which was 60% less than the standard deviation of the CRL ground force and true ground force correlations. Unfortunately, only 4 records were available to make a direct comparison between the CRL and the Endevco model due to an equipment malfunction related to the Endevco accelerometer cable being partially disconnected from the accelerometer.

Although a spectral comparison between the Endevco and CRL accelerometer with respect to each other has been completed in *Data Analysis: Part 1*, the correlation phase spectra (Figure 8.9) and amplitude spectra (Figure 8.10, Eq. 25) of each accelerometer model's respective ground force trace was computed and compared to the true ground force to determine

which ground force approximation best estimates the phase and amplitude of the true ground force. Additionally, the absolute peak force of each ground force trace, calculated by each accelerometer models, was compared to the absolute peak force of the Load Cell System (Figure 8.11).

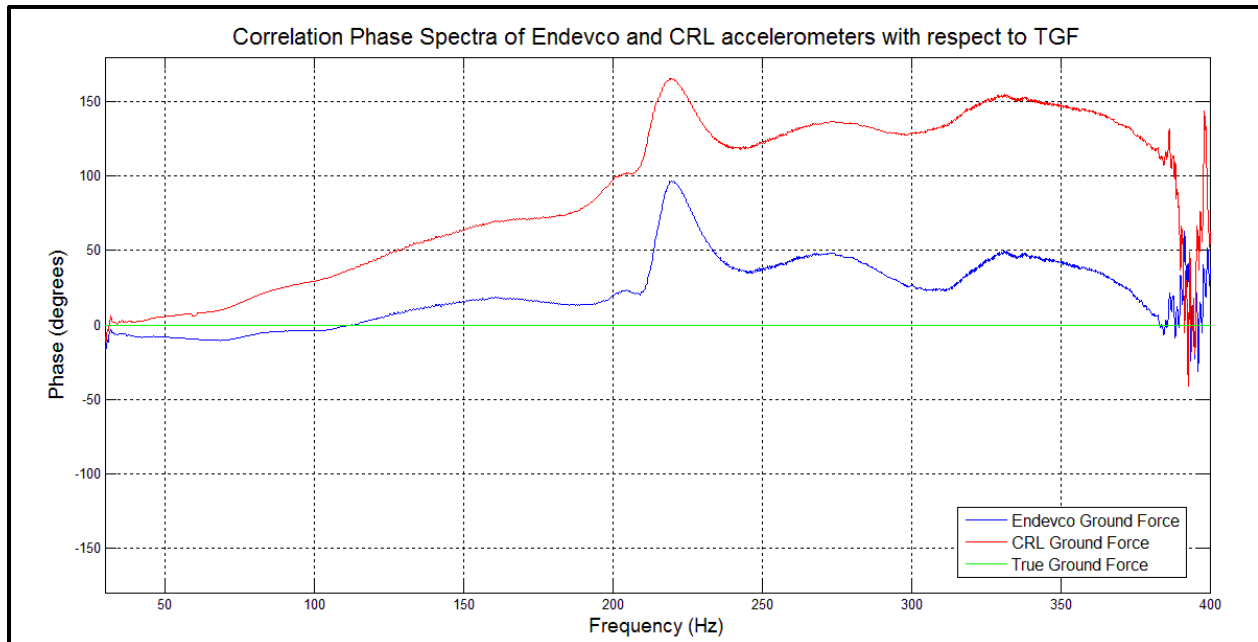


Figure 8.9. Phase spectra of the Endevco and CRL ground force correlated with the true ground force.

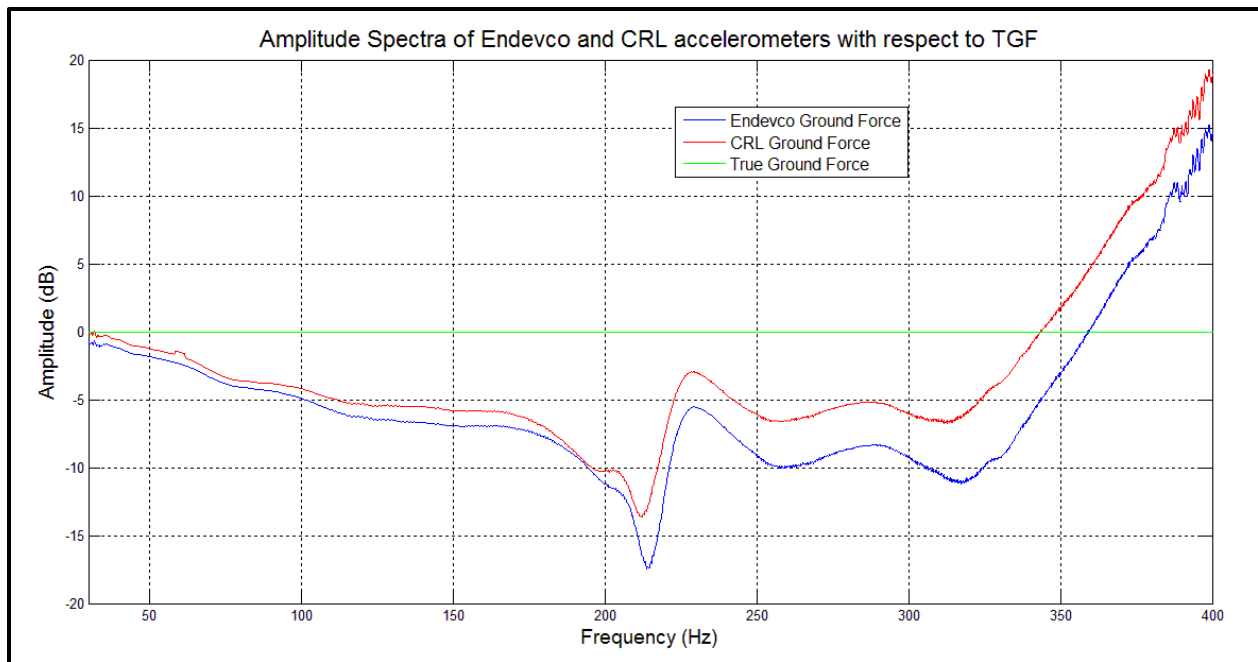


Figure 8.10. Amplitude difference between calculated Endevco and CRL ground force from the true ground force displayed in dB.

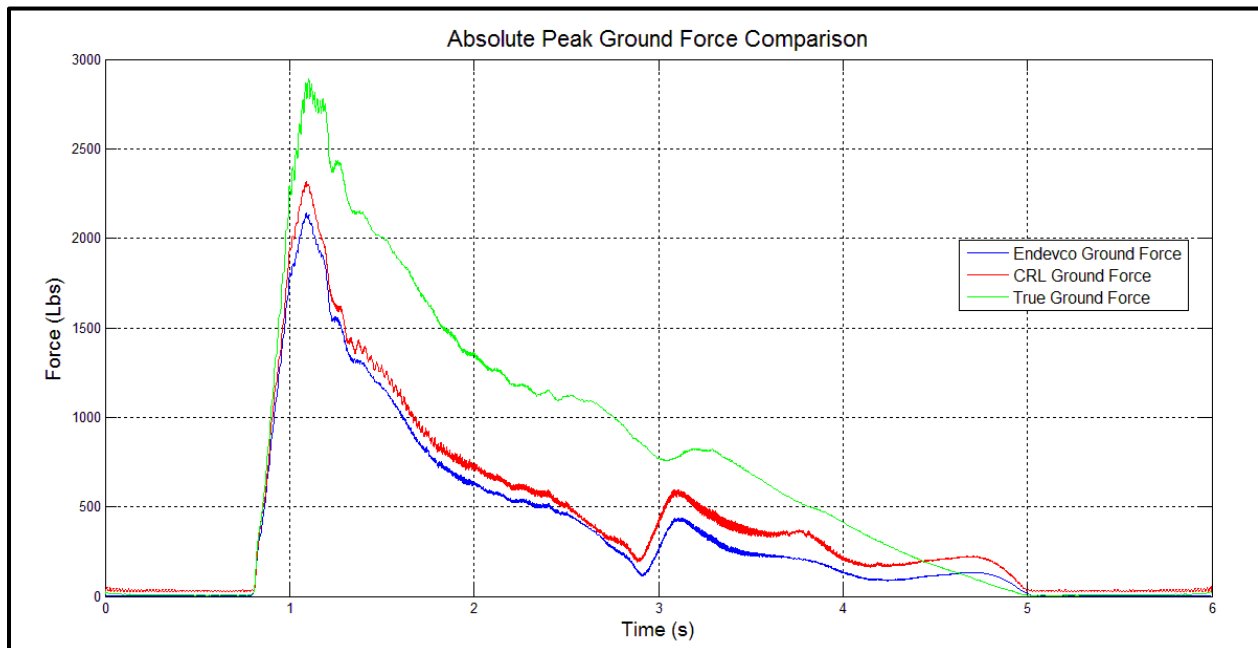


Figure 8.11. Absolute peak force comparison of the Endevco and CRL ground force to the true ground force.

8.3.4. Optimal Accelerometer Baseplate Combination

The CRL accelerometers were magnetically mounted and were easily moved around the baseplate. As described in *Methods: Part 2*, fifteen different ground force calculations were tested that varied both the number of accelerometers used and the location of accelerometers on the baseplate (Figure 8.2). For each of the fifteen different accelerometer locations, the CRL calculated ground force trace was cross-correlated with the true ground force to establish a quantitative measure of similarity between the two signals. The mean and standard deviation of the maximum correlation coefficients was computed for each accelerometer combination (Figure 8.12).

The most representative approximation for true ground force calculated with one baseplate accelerometer occurred when the CRL baseplate accelerometer was positioned adjacent to the Dytran accelerometer at approximately 17.75 cm (7 inches) away from the center of the baseplate. IVI positioned the Dytran baseplate accelerometer at this location because it was assessable and close to the center of the baseplate (E. Christensen, pers. comm.). The least representative approximation of true ground force occurred when the CRL baseplate accelerometer was located on a rib at radial location 3. Correlation phase spectrum (Figure 8.13) and amplitude spectrum (Figure 8.14) were calculated with respect to the corresponding true ground force to show the variations in phase and amplitude associated with these accelerometer locations. When using four baseplate accelerometers to approximate ground force (augmented weighted-sum), the most representative (accelerometer combination 2) and least representation (accelerometer combination 6) approximation of true ground force only varied from one another by $< 2\%$. The correlation phase spectrum (Figure 8.15) and amplitude spectrum (Figure 8.16) were calculated for each approximation with respect to true ground force.



Figure 8.12. Mean correlation of ground force approximation calculated by a) using a single baseplate accelerometer and b) using a combination of four accelerometers located on the baseplate to their respective true ground force calculated by the Load Cell System with corresponding standard deviation represented by error bars.

Absolute peak ground force was calculated for each of the four (Dytran accelerometer location, on rib 3, combination 2, and combination 6) accelerometer locations and compared to the absolute peak force of the true ground force signal. The true ground force for each of the four accelerometer combinations is very similar, which is expected because the true ground force measurements only varied by $\pm 1\%$. However, a qualitative measure of the differences between performance of the sensor configurations can be established by plotting the the most representative and least representative ground force signal using both one baseplate accelerometer (Figure 8.17) and a combination of four baseplate accelerometers (Figure 8.18).

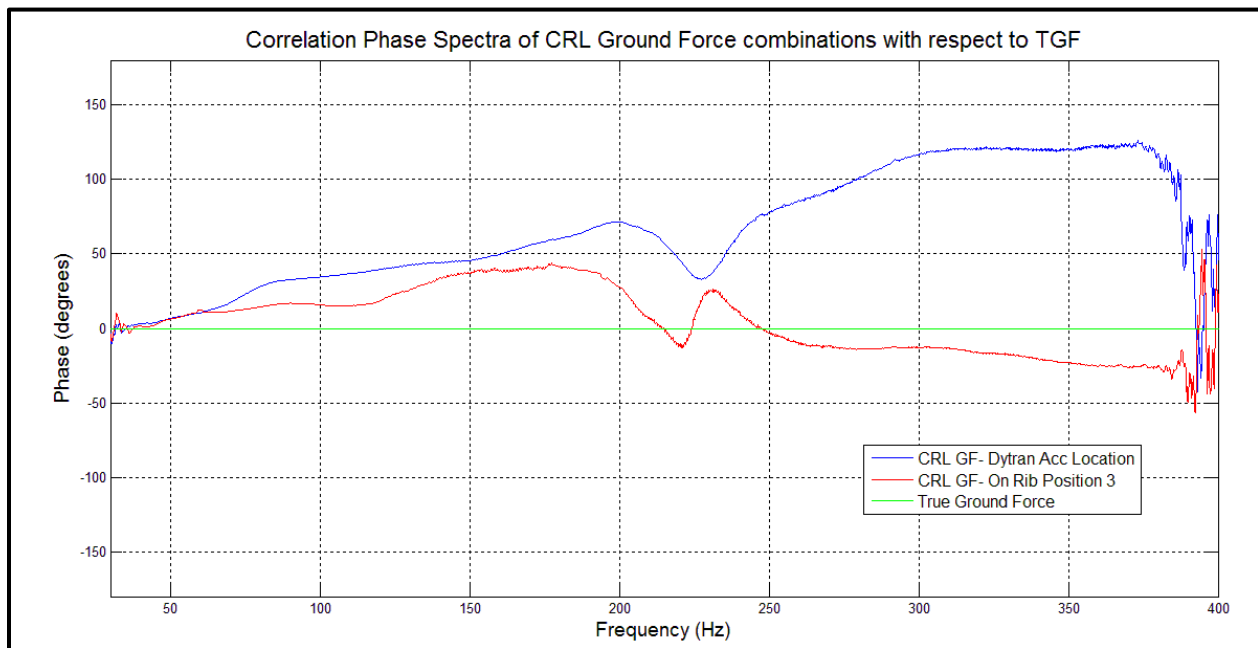


Figure 8.13. Phase spectra of the most representative ground force approximation and least representative ground force approximation using one CRL baseplate accelerometer correlated with respect to their respective true ground force.

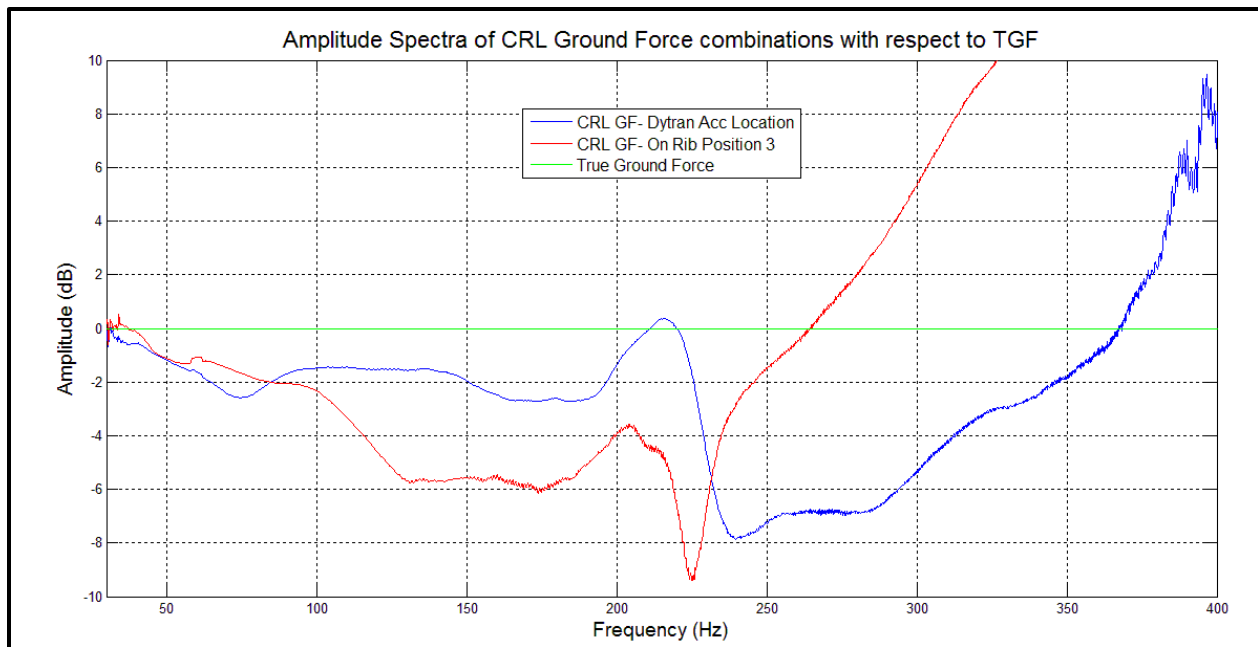


Figure 8.14. Amplitude spectra of the most representative ground force approximation and least representative ground force approximation using one CRL baseplate accelerometer with respect to the true ground force displayed in dB.

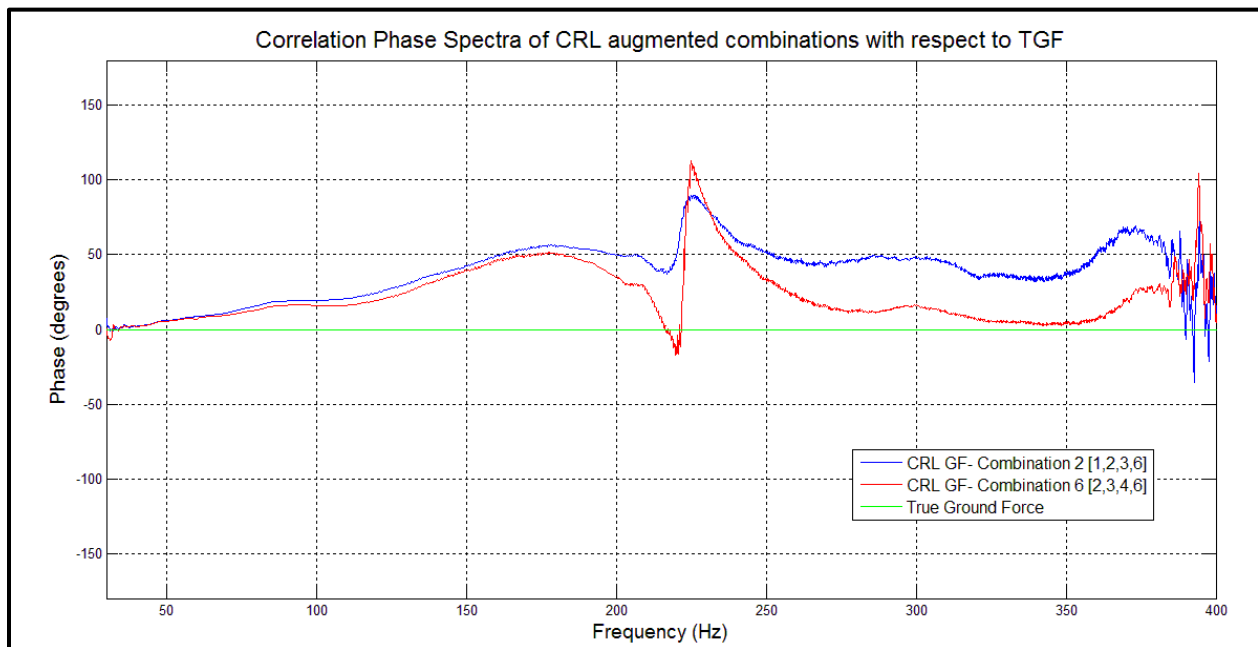


Figure 8.15. Phase spectra of the most representative ground force approximation and least representative ground force approximation using four CRL baseplate accelerometers correlated with the true ground force.

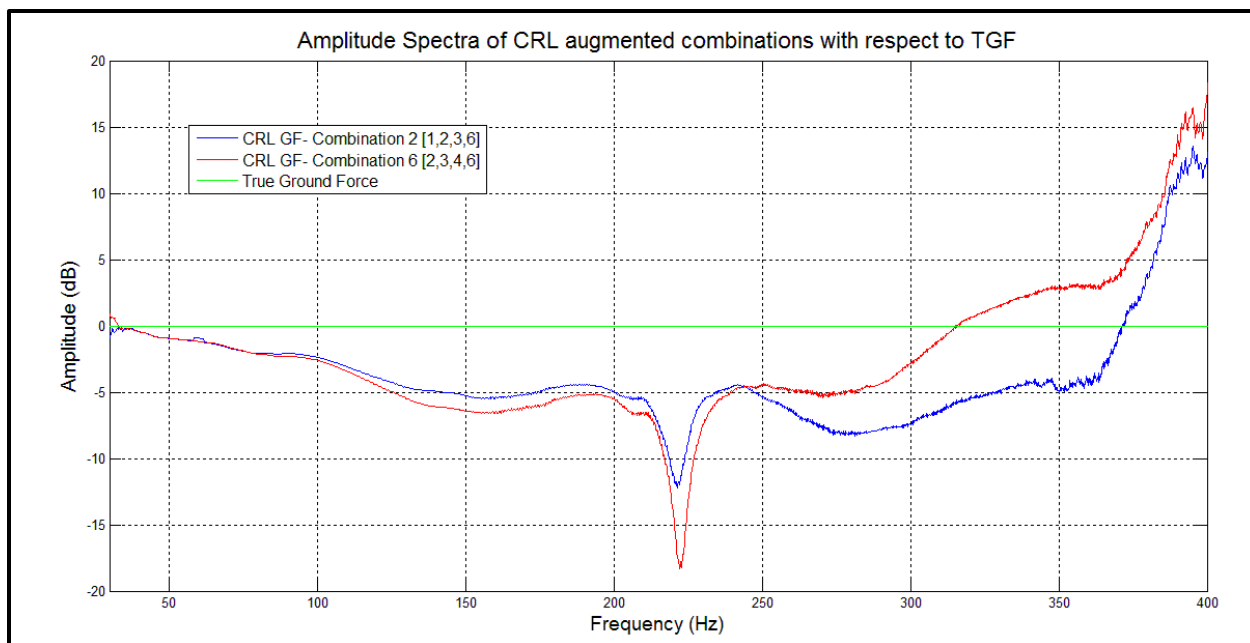


Figure 8.16. Amplitude spectra of the most representative ground force approximation and least representative ground force approximation using four CRL baseplate accelerometers with respect to the true ground force displayed in dB.

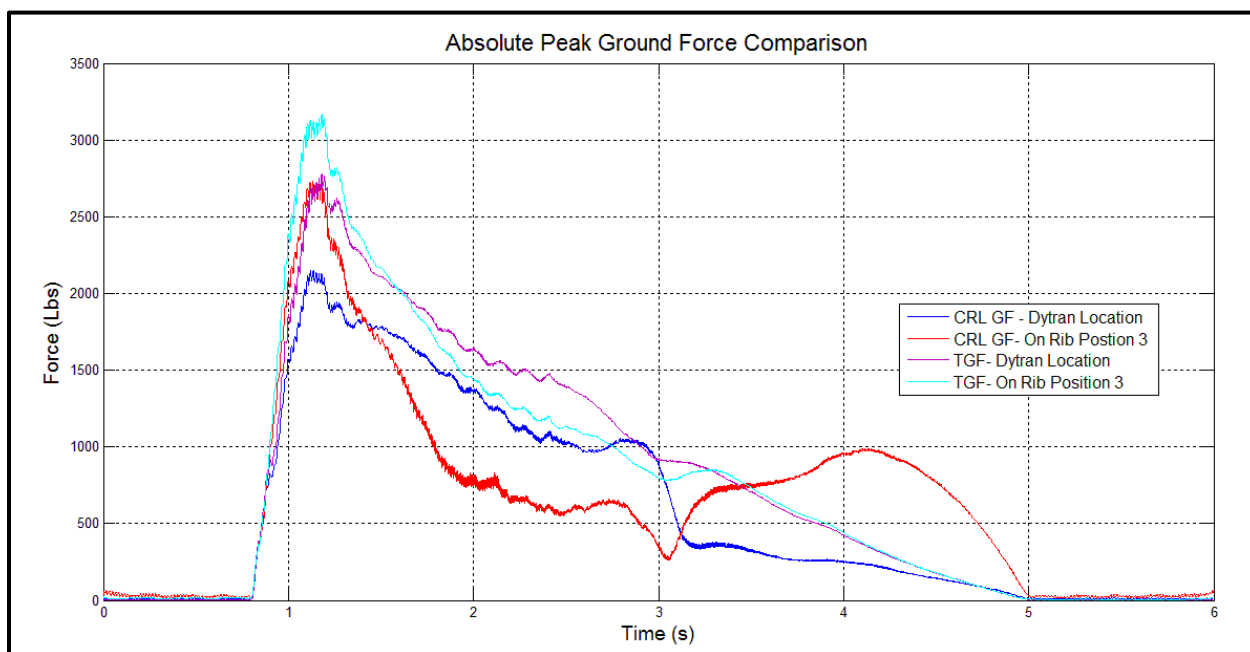


Figure 8.17. Absolute peak force comparison of the most and least representative ground force calculated using one CRL baseplate accelerometer to their respective true ground force.

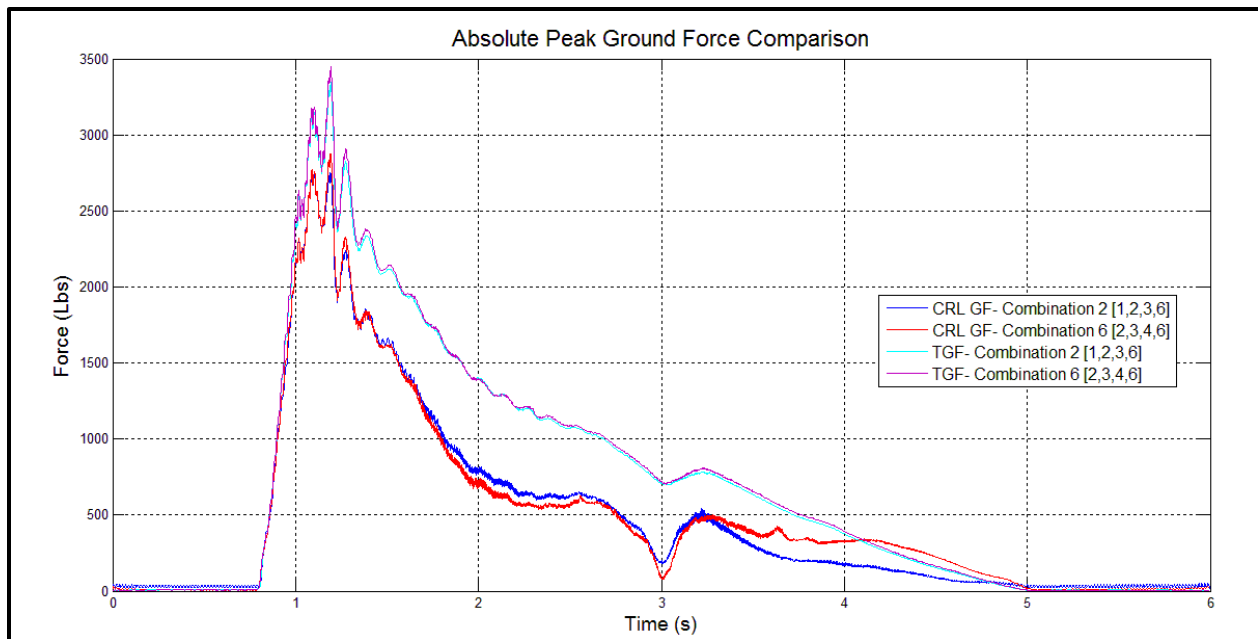


Figure 8.18. Absolute peak force comparison of the most and least representative ground force calculated using four CRL baseplate accelerometers to their respective true ground force.

9. Discussion: Part 2; Optimizing Ground Force Approximation

Examining the feedback signal with respect to true ground force revealed that the Dytran accelerometer model generates a poor approximation of the true ground force with significant variability from sweep to sweep compared to the CRL accelerometer model. The mean correlation between the Dytran ground force and the true ground force was 88.8% with a standard deviation of 4%, which was significantly less than the mean correlation between the CRL ground force and the true ground force (97.6% with a standard deviation of 0.3%), calculated at the same baseplate position. The phase spectrum of each model with respect to the true ground force was almost identical (Figure 8.6) across the bandwidth of the sweep, but the amplitude spectrum of each model with respect to the true ground force was significantly dissimilar (Figure 8.7). The Dytran ground force overestimated the force output of the seismic vibrator above ≈ 120 Hz by up to $\approx 50\%$ of the true ground force and underestimated the force output under ≈ 120 Hz by up to $\approx 33\%$ of the true ground force. It is evident that the Dytran ground force is not representative of the true ground force, whereas the CRL accelerometer is a more accurate approximation of ground force (Figure 8.8). Therefore, it is not advisable to use the feedback signal collected by the Dytran accelerometers to correlate raw vibroseis seismic data.

The mean correlation coefficients between the Endevco and the CRL ground force calculations and the true ground force were extremely similar. However, the Endevco model produced a more consistent measure of the motion. The standard deviation of Endevco correlations to the true ground force was 1.7%, while the CRL standard deviation was 2.8%. The difference in variability between the two ground force calculations may be attributed to the different mounting mechanisms. Since the CRL accelerometers were magnetically mounted, it is

likely that decoupling between the CRL accelerometers and the seismic vibrator occurred at high frequencies. Determination of the optimal accelerometer model could be established in spite of the fact the comparison between the Endevco accelerometer model and the CRL accelerometer model with respect to the true ground force was at less than optimal baseplate positions (near the edge of the baseplate).

Each ground force amplitude spectra with respect to the true ground force displayed similar trends. The CRL ground force amplitude spectrum was closer to that of the true ground force with a maximum amplitude difference of 13 dB at approximately 215 Hz (Figure 8.10). The Endevco ground force phase more closely matched the phase of the true ground force. The maximum phase difference between the CRL ground force phase and the true ground force phase was approximately 160 degrees at 225 Hz, while the maximum phase difference between the Endevco and true ground force was approximately 100 degrees at 225 Hz (Figure 8.9). Although the peak ground force of these two approximate ground forces compared to the true ground force are very similar (Figure 8.11), differences in both amplitude and phase are evident between the Endevco ground force and the CRL ground force.

The optimal accelerometer number and baseplate position(s) to generate the most representative ground force for the IVI Minivib I was determined by correlation with the CRL accelerometer model for the IVI Minivib I. When limited to only one baseplate accelerometer at a particular site, the best baseplate location is at approximately 17.75 cm (7 inches) away from the center of the baseplate. The greatest correlation between approximate ground force and true ground force (97.6%) occurred at the factory located Dytran baseplate accelerometer position, approximately 17.75 cm away from the center of the baseplate. Although this position produced the greatest correlation, no extensive testing was done by IVI to determine the optimal baseplate

accelerometer position to approximate ground force (E. Christensen, pers. comm.). The least representative ground force approximation using a single baseplate accelerometer occurred when the accelerometer was located at on rib radial position (88.7%). In general, the correlation between the approximate ground force and the true ground force decreased as the distance away from the center of the baseplate increased (Figure 8.12), which is consistent with the decreasing rigidity distribution towards the edge of the plate. Data for this experiment were collected at one source location and the optimum baseplate accelerometer placement may depend on near-surface conditions and therefore these results must be considered a signal sample.

As expected using one baseplate accelerometer, significant phase and amplitude differences were observed with respect to the true ground force signal between the most representative and least representative ground force approximation. After approximately 250 Hz, the phase difference between the ground force calculated using one accelerometer located at the factory Dytran accelerometer position and the ground force calculated using one accelerometer located at on rib radial position 3 were $> 100^\circ$. However, the ground force signal phase calculated with one accelerometer located at on rib radial position 3 was more consistent with the phase of the true ground force (Figure 8.13). Amplitude differences between the two ground force signals and the true ground force were much more pronounced and contributed to the low correlation coefficient between the true ground force and the approximate ground force using one accelerometer located at on rib radial positions 3. At approximately 260 Hz, the ground force amplitude using the baseplate accelerometer located at on rib radial position 3 was greater than that of the true ground force and doubled the ground force output at 300 Hz (Figure 8.14). Therefore at approximately 3.5 seconds, the true ground force is overestimated using this approximation (Figure 8.18).

The overall mean correlation between the 7 different approximations of ground force using 4 baseplate accelerometers and the true ground force was 96% with a standard deviation of 0.7%. Approximating ground force using an augmented weighted-sum (multiple baseplate accelerometers) provided a more consistent approximation of ground force compared to the ground force approximations using one baseplate accelerometer (Figure 8.12). Since the baseplate motion is dependent on the near-surface conditions, using multiple baseplate accelerometers to average the motion of the baseplate will lead to a more accurate approximation of ground force for varying near-surface conditions (Wei, 2009). Although each correlation between the 15 different accelerometer locations tested and the true ground force was $> 88\%$, increasing the accuracy of the ground force approximation will increase data resolution when deconvolving the recorded data with the ground force approximation.

Spectral analysis of the most and least representative ground force approximations, combination 2 and combination 6 respectively, using the 4 baseplate accelerometers with respect to the true ground force reiterated that the variations between the two ground force approximations are minimal (Figure 8.15 and 8.16). Consequently for frequencies > 250 Hz, the amplitude of the least representative ground force approximation using multiple accelerometers is up to 3 dB closer to the true ground force compared to using one baseplate accelerometer (Figure 8.14 and 8.16). To optimize the approximation of the vibrator output for high frequency data, it is necessary to average the motion of the baseplate by using multiple baseplate accelerometers (Sallas, 2010; Wei, 2010).

At approximately 225 Hz for all analyzed records, the correlated phase spectrum of the approximate ground force with respect to the true ground force experiences an abrupt local maximum or local minimum depending on the location of the baseplate accelerometers. For

ground force approximations calculated with an accelerometer located at the factory Dytran accelerometer position, the correlated phase spectrum with respect to the true ground force experiences a local minimum at 225 Hz. For all other approximations, the accelerometers were placed on the opposite side of the baseplate and the correlated phase spectrum with respect to the true ground force experiences a local maximum at 225 Hz. At approximately 225 Hz, the amplitude spectrum for all records analyzed with respect to true ground force experience an abrupt decrease in amplitude. Since the amplitude and frequency anomalies shift at approximately the same frequency while phase changes are opposite on opposite sides of the baseplate, it can be concluded that 225 Hz is a resonant frequency or natural frequency of the baseplate and load cells at this particular source location (Wei et al., 2010; Wei and Phillips, 2011). Resonance effects increase for high frequency vibroseis data due to increased baseplate flexure. This flexure adversely affects the ground force approximation by introducing increased levels of harmonic distortion and thereby reducing the amount of useable signal energy (Wei, 2008a; Wei, 2008b). Furthermore, resonance frequencies of the baseplate are dependent on the near-surface conditions and difficult to obtain or estimate analytically (Sallas, 2010).

10. Conclusions: Part 2; Optimizing Ground Force Approximation

The vibrator output could significantly be improved by upgrading the Dytran accelerometers used for the feedback signal to higher-quality accelerometers. The Dytran accelerometers resulted in the poorest ground force approximation out of the three accelerometers tested. When directly compared to the CRL accelerometer position, the Endevco accelerometer model provided the most accurate ground force approximation with the smallest measurement variability. Although ideal for this survey, magnetic mounts have the potential of decoupling from the baseplate generating unwanted harmonic distortion within the source signature approximation. Therefore, the Endevco accelerometer model should be used when the most accurate measure of ground force is the goal. However, if the CRL accelerometer model could be mounted directly to the baseplate, it will provide a better estimation of ground force than the Dytran model.

Optimizing the location and number of baseplate accelerometers provided increased accuracy of the true ground force collected by the Load Cell System. When limited to one baseplate accelerometer, the optimum location for the particular near-surface conditions tested was approximately 17.75 cm away from the center of the baseplate. However, it is possible that a better approximation can be achieved closer to the center of the baseplate since the closest accelerometer position tested was only 17.75 cm away from the baseplate center. A decrease in approximation accuracy occurred with increased distance away from the center of the baseplate increased. Collecting acceleration from a single point on the baseplate can vary considerably due to the inherent non-rigidity of the driven structure (Wei, 2009; Sallas, 2010). Multiple accelerometers should be positioned and evaluated on the baseplate at various radial positions both on and off rib reinforcement to optimize the ground force approximation for multiple source

locations. Since the mean correlation between all 7 accelerometer combinations tested using 4 accelerometers and the true ground force was approximately $96\% \pm 1\%$, any combination would provide an accurate estimation of the true ground force. Furthermore since baseplate resonance increases at locations with less rigidity (i.e. towards the outside edge of the plate), it may be advantageous to limit the number of accelerometers located at the edge of the baseplate when approximating ground force (Sallas, 2010; Wei, 2010).

Although using multiple accelerometers increased the precision of the source signature approximation, it failed to accurately approximate the true ground force above 200 Hz. The Load Cell System measured approximately twice the amount of energy being transferred to the ground above 200 Hz compared to the weighted-sum approximation (Figure 8.18). This may explain why synthetic sweep cross-correlation of the raw vibroseis data has recovered more high frequency energy than ground force deconvolution using the current IVI Minivib system. However, the energy recorded by the Load Cell System decreases to less than $1/3^{\text{rd}}$ of the maximum vibrator output above 200 Hz because the phase reversal between the baseplate and the reaction mass.

The baseplate on the IVI Minivib I must be modified to obtain its advertised broadband frequency range. Increasing the baseplate weight by 100% could resolve or at least remediate the problematic phase reversal, which would result in a higher energy output for frequencies over 200 Hz. Additionally, reducing the size of the vibrator baseplate by 50% would decrease baseplate flexure and provide a source that more closely represents a point source of propagation. This would also increase the accuracy of the ground force approximation by decreasing harmonic energy in the approximation and therefore allow for improved ground force deconvolution.

Alternatively for the current IVI Minivib I baseplate configuration, improvements in the ground force approximation, especially for frequencies > 200 Hz, may be achieved by drilling holes through the external shell of the baseplate and placing baseplate accelerometers directly on top of the baseplate surface. Placement of accelerometers directly on top of the baseplate surface would more closely represent measurements collected from the load cell system resulting in increased energy recorded for frequencies above 200 Hz. A more conservative approach to attaining more energy above 200 Hz is the use of a nonlinear high-dwell sweep when acquiring data (Goupillaud, 1976). A nonlinear high-dwell sweep may alter the baseplate-reaction mass phase reversal and produce more energy for frequencies > 200 Hz.

11. Final Conclusions

Understanding the mechanical and geological limiting factors of producing an accurate ground force approximation is pivotal for fully optimizing source operations for high frequency vibroseis reflection data (Miller et al., 2009). Approximation of the source signature is difficult due to nonlinear complexities introduced within the vibrator mechanical system and nonlinear ground response to the vibrator output. Implementation of multiple baseplate accelerometers allowing averaging of the motion of the baseplate increased the precision of the weighted-sum approximation for the IVI Minivib I output by 2.8%. By directly comparing the ground force approximation to the true ground force collected by the Load Cell System, the optimum location of single as well as multiple baseplate accelerometers were determined to be around 7 inches from the center of the baseplate. When compared to the current location of the Endevco baseplate accelerometer, using multiple accelerometers in the optimum baseplate positions increased the approximation accuracy by 5% for the IVI Minivib I at the tested source location.

Mechanically, the driven structure inherently flexes generating harmonic distortion within the approximate ground force signal. The amount of harmonic energy present within the approximate source signature is dependent on near-surface conditions, source coupling, and baseplate resonance caused by baseplate flexure (Schrodt, 1987; Baetan and Ziolkowski, 1990; Wei, 2008a). Varying degrees of asymmetric baseplate motion were encountered depending on the near-surface conditions underneath the baseplate. Although the internal baseplate structure is symmetric, the IVI Minivib I baseplate did not respond symmetrically at each of the three source locations tested. It was confirmed that when driven at high frequencies the baseplate flexure is most severe at the edge of the plate, where the baseplate is least rigid, an observation consistent with previous studies (Sallas, 2010; Wei, 2010). Since harmonic distortion of a signal is not

repeatable from sweep to sweep, placement of baseplate accelerometers at locations which suffer least from baseplate flexure remediated this problem in the IVI system. To further improve the vibrator output of the IVI Minivib I, a more uniform distribution of rigidity across the baseplate is optimal. This can be achieved by manufacturing a baseplate that is uniformly thick.

At each of the three source locations tested, this study discovered that the IVI Minivib I is incapable of measuring ground force energy using the weighted-sum approximation over approximately 200 Hz because the baseplate and reaction mass become 180 degrees out of phase. To collect broadband high frequency data with the IVI Minivib I, this baseplate must be modified by increasing its weight by 100 % assuming the reaction mass weight is able to drive the baseplate at low frequencies (> 50 Hz). Additionally, increasing the baseplate rigidity by designing a new uniformly thick baseplate that is half the diameter of the current baseplate will decrease harmonic distortion caused by baseplate flexure and therefore improve the accuracy of the ground force approximation. Increased accuracy of the ground force approximation could allow for significant gains in deconvolution of raw vibroseis data.

References

- Aki K. and Richards P.G., 1980. *Quantitative Seismology*. W.H. Freeman.
- Allen, K.P., 1996. High fidelity vibratory source seismic method: U.S Patent 5 550 786.
- Allen, K.P, M.L. Johnson, and J.S. May, 1998. High fidelity vibratory seismic (HFVS) method for acquiring seismic data: 68th Annual International Meeting, SEG, *Expanded Abstracts*, p. 140-143.
- Anstey, N.A., 1964. Correlation techniques- a review, *Geophysical Prospecting*, **12**, 355-382.
- Anstey, N.A., 1991. *Vibroseis*. Prentice Hall.
- Baeten, G.J.M., 1989. *Theoretical and practical aspects of the vibroseis method*. PhD thesis, Delft University of Technology, The Netherlands.
- Baeten, G.J.M. and Ziolkowski, A. M., 1990. *The Vibroseis Source*. Elsevier.
- Bickel, S., 1982. The effects of noise on Vibroseis deconvolution. *Geophysics*, **47**, p.1174-1184.
- Brigham, E.O., and Morrow, R. E. 1967. The Fast Fourier Transform. *IEEE Spectrum*, vol. 6 no. 7, p. 41-52.
- Brittle K.F., Lines L.R., and Dey A.K., 2001. Vibroseis deconvolution: a comparison of cross correlation and frequency domain sweep deconvolution. *Geophysical Prospecting*, **49**, p. 675-686.
- Chapman, W.L., G.L. Brown, and D.W. Fair, 1981. The Vibroseis system: A high frequency tool. *Geophysics*, **46**, p. 1657-1666.
- Chakraverty, S., 2009. *Vibration of Plates*. CRC Press, Boca Raton, FL.
- Chassaing, R. and Reay, D., 2011. *Digital Signal Processing and Application with the TMS320C6713 and TMS320C6416 DSK*, 2nd Ed, John Wiley & Sons, Inc., Hoboken, NJ.
- Costain, J.K and Çoruh, C., 2004. *Basic theory of exploration seismology*. Handbook of Geophysical Exploration, Seismic Exploration, New York, Elsevier Ltd.
- Crawford, J.M., Doty, W.E., and Lee, M.R., 1960. Continuous signal seismograph, *Geophysics*, **25**, p. 95-105.
- Dickey, H.P., Zimmerman, J.L., Plinsky, R.O., and Davis, R.O., 1977. Soil Survey of Douglas County, Kansas: United States Department of Agriculture Soil Conservation Service, 73 p.

- Duffy, D.G., 2001. *Green's Functions with Applications*, CRC Press, Boca Raton, FL.
- Espey, H.R., 1998. Attenuation of Harmonic Ghosts. ASEG/SEG Conference Abstracts., **19(2)**, p 61-63.
- Ghose, R., 2002. High-frequency shear wave reflections from shallow subsoil layers using a vibrator source: sweep cross-correlation versus deconvolution with ground force derivative. *SEG Int'l Exposition and 72nd Annual Meeting*.
- Goupillaud, P.L., 1976. Signal design in the 'Vibroseis' technique. *Geophysics*, **41**, 1291-1304.
- Kay, S.M. and Marple, S.L., 1981. Spectrum Analysis- A Modern Perspective. *Proceedings of the IEEE*, **69**, p.1390-1419.
- Krohn, C., 2008. Shaped high frequency vibratory source: U.S Patent 7 436 734
- Lebedev, A.V and Beresnev, I. A., 2004. Nonlinear distortion of signals radiated by vibroseis sources. *Geophysics*, **69**, p. 968-977.
- Lebedev, A.V and Beresnev, I. A., 2005. Radiation from flexural vibrations of the baseplate and their effect on the accuracy of travel-time measurements. *Geophysical Prospecting*, **53**, p. 543-555.
- Lerwill, W. E., 1981. The amplitude and phase response of a seismic vibrator. *Geophysical Prospecting*, **29**, 503-528.
- Li, X.-P., Söllner, W., and Hubral, P., 1995. Elimination of harmonic distortion in Vibroseis data. *Geophysics*, **60**, 503-516.
- Li, X.-P., 1997. Elimination of ghost noise in vibroseis data by deconvolution. *Geophysical Prospecting*. **45**, 909-929.
- Liner, C.L., 2004. *Elements of 3D Seismology*, PennWell Corp., Tulsa, Okla.
- Mewhort, L., Bezdan, S., and Jones, M. 2002. Does it matter what kind of vibroseis deconvolution is used? *CSEG Geophysics 2002 Conference Extended Abstracts*: 1-4.
- Miller, G.F. and Pursey, H., 1954. The field and radiation impedance of mechanical radiators on the free surface of a semi-infinite isotropic solid. *Proc. Roy. Society, ser. A.*, v. 223, p 521-540.
- Miller, R., Rademacker, T.R. and Lambrecht, J.L., 2004. Field test of two high frequency vibrators with two high frequency servovalues at two sites in Kansas with near-surface emphasis. *SEG Expanded Abstracts*, **23**.

- Miller, R., Xia, J., Rice, D., Walters, S.L., and Rademacker, T. R., 2009. Near- surface utility of vibroseis. *SEG Expanded Abstracts*, p. 1330-1333.
- O'Conner, H.F., 1960. *Geology and Ground-water Resources of Douglas County, Kansas*: Kansas Geological Survey, Bulletin 148, 200 p.
- Pugin, A. J.-M., Pullan, S.E., and Hunter, J. A., 2009. Multicomponent high-resolution seismic reflection profiling. *The Leading Edge*, **28**, p. 1248-1261.
- Rademacker, T.R., 2006. *Optimizing High-Frequency Vibroseis Data*. Master's Thesis, The University of Kansas.
- Rao, S. S., 2007. *Vibration of continuous systems*, John Wiley & Sons, Inc., Hoboken, NJ.
- Reust, D.K., 1995. Vibrator force control: How simple can it get?: *The Leading Edge*, **14**, 1129-1133.
- Rice, D., 2009. *Applicability of 2-D Time-Lapse High Resolution Seismic Reflection Approach to Image Natural Salt-Dissolution and Subsidence in Central Kansas and Improved Post- Processed Vibroseis Data Characteristics*. Master's Thesis, The University of Kansas.
- Sallas, J.J. and Weber, R.M, 1982. Comments on "The amplitude and phase response of a seismic vibrator" by W.E. Lerwill. *Geophysical Prospecting*, **30**, p. 935-938.
- Sallas, J.J., 1984. Seismic vibrator control and the downgoing P-wave. *Geophysics*, **49**, p.732-740.
- Sallas, J.J., Amiot, E.A., and Alvi, H.I., 1985. Ground force control of a P-wave vibrator, *SEG field techniques workshop*, August 13-16, 1985, Monterey, California.
- Sallas, J.J., 2010. How do hydraulic vibrators work? A look inside the black box. *Geophysical Prospecting*, **58**, no. 1, p 3- 18.
- Saragiotis, C., Scholtz, P. and Bagaini, C., 2010. On the accuracy of the ground force estimated in vibroseis acquisition. *Geophysical Prospecting*, **58**, p. 69-80.
- Schrodt, Joseph K., 1987. Techniques for improving Vibroseis data. *Geophysics*, **52**, p. 469-482.
- Seriff, A.J. and Kim, W.H., 1970. The effect of harmonic distortion in the use of vibratory surface sources. *Geophysics*, **35**, p. 234- 246.
- Shan, S., Eick, P.M., Brewer, J.D., Zhu, X., and Shaw, S.A., 2009. Load cell system test experience: Measuring the vibrator ground force on land seismic acquisition. *SEG Expanded Abstracts*, **28**, p. 16-20.

- Sill, R. D and Seller, E.J., 2006. Accelerometer Transverse Sensitivity Measurement Using Planar Orbital Motion. *77th Shock and Vibration Symposium*, November 2006, Monterey, California.
- Solodov, I. Y., 1998. Ultrasonic of non-linear contacts: Propagation, reflection and NDE-applications: *Ultrasonics*, **36**, p. 383–390.
- Steeple, D.W. and Miller, R., 1998. Avoiding pitfalls in seismic reflection surveys. *Geophysics*, **63**, p. 1213-1224.
- Szilar, R., 2004. *Theories and Applications of Plate Analysis: classical, numerical, and engineering methods*, John Wiley & Sons, Inc., Hoboken, NJ.
- Timoshenko, S. and Woinowsky-Kreiger, S., 1959. *Theory of Plates and Shells*. 2nd edition, McGraw-Hill, New York.
- van der Veen, Michiel, J. Brouwer, and K. Helbig, 1999. Weighted-sum method for calculating ground force: an evaluation by using a portable vibrator system. *Geophysical Prospecting*, **47**, p. 251-267.
- Ventsel, E. and Krauthammer, T., 2001. *Thin Plates and Shells: theory, analysis, and applications*. Marcel Dekker, Inc., New York.
- Walker, D., 1995. Harmonic resonance structure and chaotic dynamics in the earth-vibrator system. *Geophysical Prospecting*, **43**, 487-507.
- Walters, S.L., 2009. *Coupling: Impact and Implications for High-Resolution Time-Lapse Seismic Surveying*. Master's Thesis, The University of Kansas.
- Wei, Z., 2008a. Design of a P-wave seismic vibrator with advanced performance. *GeoArabia*, **13**, p. 123-136.
- Wei Z., 2008b. Pushing the vibrator envelope: extending low and high frequency limits. *First Break*, **26**, p. 37-43.
- Wei Z., 2009. How good is the weighted-sum estimate of vibrator ground force?. *The Leading Edge*, **28**, p. 960-965.
- Wei, Z., Phillips, T.F., and Hall, M.A., 2010. Fundamental discussions on seismic vibrators. *Geophysics*, **75**, p. w13-w25.

- Wei, Z., 2010. Modelling and modal analysis of seismic vibrator baseplate. *Geophysical Prospecting*, **58**, p. 19-32.
- Wei, Z., Phillips, T.F., and Hall, M.A., 2011. Geophysical benefits from an improved seismic vibrator. *Geophysical Prospecting*, **60**, p. 1-14.
- Witteaman, W. J., 2006. *Detection and signal processing: technical realization*, Springer, Berlin.
- Yilmaz, O., 2001. Seismic data analysis: Procssing, Inversion and Interpretations of Seismic Data, Volume 1. 2nd ed. Soc. Expl. Geophys.
- Zeller, D. E., ed., 1968. The stratigraphic succession in Kansas: Kansas Geological Survey Bulletin 189, 81 p.
- Ziolkowski, A. M., 2010. Review of vibroseis data acquisition and processing for better amplitudes: adjusting the sweep and deconvolving for time derivative of true ground force. *Geophysical Prospecting*, **58**, p. 41-53.

Appendix A

From Figure 2.1, the equations of motion are described as (Sallas, 1984):

$$-F_a = M_r \ddot{x}_r + D_a (\dot{x}_r - \dot{x}_b) + K_a (x_r - x_b), \quad (A.1)$$

$$F_a + F_t - F_g = M_b \ddot{x}_b - D_a (\dot{x}_r - \dot{x}_b) - K_a (x_r - x_b). \quad (A.2)$$

Summing up the equation of motions (equations (A.1) and (A.2)), gives

$$F_t - F_g = M_b \ddot{x}_b + M_r \ddot{x}_r \quad (A.3)$$

where the force due to vehicle vibration, F_t $\begin{cases} = 0 \text{ if vehicle is vibrationally isolated} \\ \neq 0 \text{ if vehicle is not vibrationally isolated} \end{cases}$

most seismic vibrators are vibrationally isolated, therefore, $F_t = 0$ in most instances.

Appendix B

Derivation of the Governing Differential Equation

From classical plate theory, a plate is a structural element with dimensions that are relatively large compared to its thickness and are subjected to loads that cause bending and stretching deformation. Consider the problem of an isotropic plate (uniformly thick plate with uniform elastic properties) under a static transverse load. To derive the differential equation of motion for the plate using classical plate theory, the following assumptions must be considered (Timoshenko and Woinowsky-Kreiger, 1959; Chakraverty, 2008):

- 1) The material of the plate is homogeneous, isotropic and linearly elastic. The plate, therefore, obeys Hooke's Law.
- 2) Straight lines perpendicular to the mid-surface before deformation remain straight after deformation. This assumption is valid if the deflections are small compared to the plate thickness.
- 3) The middle surface of the plate is a neutral surface and remains unstrained during bending. This assumption is valid if plate deflections are small compared to the plate thickness.
- 4) The transverse normals rotate such that they remain perpendicular to the middle surface after deformation and the effect of rotator inertia is negligible.
- 5) The thickness of the plate is small when compared to other dimensions.

It is important to note that the plate equations derived from classical plate theory are approximations, but appropriate for the purpose of this study because plate theory was derived from basic linear wave equations in an elastic medium and transverse motion applied to the

vibroiseis baseplate is negligible when compared to the vertical motion applied by the vibrator reaction mass.

The assumptions of classical plate theory make it possible to derive the plate equation in terms of displacement. The derivation of the plate equation can be solved by determining four different components (Baeten, 1989):

- 1) the strain components in terms of plate deflection;
- 2) the stress relationships, determined from Hooke's law;
- 3) the resulting forces and moments per unit length in the x and y direction; and
- 4) the equilibrium conditions of the forces and moments.

Using these four components, the governing differential equation for the deflection of a thin plate subjected to a static transverse load in Cartesian coordinates is (Timoshenko and Woinowsky-Kreiger, 1959; Ventsel and Krauthammer, 2001):

$$D \left\{ \frac{\partial^4 w(x,y)}{\partial x^4} + 2 \frac{\partial^4 w(x,y)}{\partial x^2 \partial y^2} + \frac{\partial^4 w(x,y)}{\partial y^4} \right\} = p(x, y) \quad (\text{B.1})$$

where D is the flexural rigidity of the plate, $w(x, y)$ is the normal displacement of the plate in the z direction with respect to a location (x, y) on the plate, and $p(x, y)$ is the distributed load acting on the plate at the location (x, y). Commonly, this equation is condensed to the form,

$$D \nabla^4 w(x, y) = p(x, y) \quad (\text{B.2})$$

where ∇^4 is called the biharmonic operator and is defined as:

$$\nabla^4() = \left\{ \frac{\partial^4}{\partial x^4} + 2 \frac{\partial^4}{\partial x^2 \partial y^2} + \frac{\partial^4}{\partial y^4} \right\} \quad (\text{B.3})$$

From equation (B.1), the equation for flexural rigidity, D, which represents the bending of the plate is (Szilard, 2004):

$$D = \frac{E h^3}{12(1-\nu^2)} \quad (\text{B.4})$$

where E is the modulus of elasticity for the plate, ν is the Poisson's ratio for the plate, and h is the plate thickness.

Dynamic terms for the plate equation

To solve the problem for a vibrating baseplate, the equation must include a time varying load acting on the baseplate. When calculating the force equilibrium in the z direction for a time varying load, a term must be introduced that takes into consideration the acceleration of the mass of the baseplate. The governing partial differential equation for the deflection of an isotropic, uniformly thick, plate under a dynamic transverse load is (Rao, 2007 ; Chakraverty, 2008):

$$D \left\{ \frac{\partial^4 w(x,y,t)}{\partial x^4} + 2 \frac{\partial^4 w(x,y,t)}{\partial x^2 \partial y^2} + \frac{\partial^4 w(x,y,t)}{\partial y^4} \right\} + \rho h \frac{\partial^2 w(x,y,t)}{\partial t^2} = p(x, y, t) \quad (B.5)$$

where h is the plate thickness, and ρ is the density of the baseplate. Similarly, equations (B.1-B.5) can be derived for circular plates by using polar coordinates.

The pressure applied, $p(x, y, t)$, to the vibrator baseplate consists of two terms denoted as:

$$p(x, y, t) = T_s(x, y, t) + p^{drive}(x, y, t) \quad (B.6)$$

The first term is the traction at the surface of the earth, T_s . The second term is the pressure applied by the drive system at the top of the baseplate, $p^{drive}(x, y, t)$, which is given by (Baeten, 1989):

$$p^{drive}(x, y, t) = \begin{cases} \frac{F^{applied}}{A^F} = \frac{m_r a_r}{A^F}, & x, y \in S^F \\ 0, & x, y \notin S^F \end{cases} \quad (B.7)$$

where m_r is the mass of the reaction mass, a_r is the reaction mass acceleration, and A^F is the area of the surface, S^F , where the force is exerted upon.

Boundary Conditions

A solution to the governing plate equation (B.5) must simultaneously satisfy the differential equation as well as prescribed boundary conditions for the specific plate problem at hand (Szilard, 2004). The boundary conditions must be established to solve equation (B.5). Equation (B.5) is a fourth-order partial differential equation and requires two conditions at each boundary. Since the baseplate is vibrating freely on the earth's surface, the free edge boundary condition applies to all boundaries of the problem. It implies that there is no bending and twisting moments, and no vertical shearing forces acting on the plate boundaries (Baeten, 1989):

$$\begin{cases} x = 0 \text{ or } x = x^{edge}: M_x = F_{xz} = 0 \\ y = 0 \text{ or } y = y^{edge}: M_y = F_{yz} = 0 \end{cases} \quad (\text{B.8})$$

Solution to governing partial differential equation

Equation (B.5), subjected to the boundary conditions (B.8), cannot be solved analytically. For that reason, Baeten (1989) approximates the solution to this problem by considering an infinite plate of uniform thickness, h , subjected to a point force in the Fourier domain. The Fourier domain equivalent to equation (B.5) is:

$$D \left\{ \frac{\partial^4 W(k_x, k_y, \omega)}{\partial k_x^4} + 2 \frac{\partial^4 W(k_x, k_y, \omega)}{\partial k_x^2 \partial k_y^2} + \frac{\partial^4 W(k_x, k_y, \omega)}{\partial k_y^4} \right\} - \sigma \omega^2 W(k_x, k_y, \omega) = P(k_x, k_y, \omega) \quad (\text{B.9})$$

where $W(k_x, k_y, \omega)$ is the displacement function in the frequency domain, $P(k_x, k_y, \omega)$ is the dynamic load applied to the baseplate in the frequency domain, $\sigma = \rho h$ and denotes the surface density of the mass of the baseplate (assumed constant), and $-\sigma \omega^2 W(k_x, k_y, \omega)$ is the Fourier domain equivalent to the dynamic term in equation (B.5).

By replacing $P(k_x, k_y, \omega)$ with the representation of a point force in the Fourier domain, an approximate solution can be derived, denoted by the Green's Function, $G^{plate}(k_x, k_y, \omega)$:

$$D \left\{ \frac{\partial^4 G^{plate}(k_x, k_y, \omega)}{\partial k_x^4} + 2 \frac{\partial^4 G^{plate}(k_x, k_y, \omega)}{\partial k_x^2 \partial k_y^2} + \frac{\partial^4 G^{plate}(k_x, k_y, \omega)}{\partial k_y^4} \right\} - \sigma \omega^2 G^{plate}(k_x, k_y, \omega) = \delta(k_x - k'_x, k_y - k'_y) \quad (B.10)$$

The solution to this differential equation can be obtained by solving for $G^{plate}(k_x, k_y, \omega)$.

Baeten (1989) formulates the solution to equation (B.10) given by:

$$G^{plate}(r) = - \frac{1}{8i\omega\sqrt{\sigma D}} \left[H_0^{(1)}(ar) - H_0^{(1)}(iar) \right] \quad (B.11)$$

where $H_0^{(1)}$ denotes the Hankel function of order zero, D is the flexural rigidity of the baseplate,

σ is the surface density of mass of the baseplate, and a is:

$$a = \left(\frac{\sigma \omega^2}{D} \right)^{\frac{1}{4}} \quad (B.12)$$

and r is the distance from the observation point, x_o , to the integration point, x'_o , given by:

$$r = [(x_o - x'_o)(x_o - x'_o)]^{\frac{1}{2}} \quad (B.13)$$

Baeten (1989), furthermore, shows that the limiting value for $G^{plate}(r)$ as r approaches zero exists and is approximately equal to:

$$G^{plate}(r \approx 0) = - \frac{1}{8i\omega\sqrt{\sigma D}} \quad (B.14)$$

The displacement of the baseplate can be solved by spatially convolving the Green's Function (Equation B. 11) with the pressure applied to the baseplate (Equation B.7) (Baeten, 1989; Duffy, 2001):

$$W(k_x, k_y) = \iint_{SF} \{ P^{applied}(k'_x, k'_y) + T_s(k'_x, k'_y) \} G^{plate}(k_x - k'_x, k_y - k'_y) dk'_x dk'_y \quad (B.15)$$

where (k_x, k_y) is the observation position in the Fourier domain and (k'_x, k'_y) is the position of integration in the Fourier domain.

Assuming the Green's Function is constant across the baseplate, the term containing the Hankel functions must be constant (Baeten, 1989). As a result,

$$ar = \left(\frac{\sigma\omega^2}{D}\right)^{1/4} r \approx \text{constant} \quad (\text{B.16})$$

The value $r = 0$ is always attained in the spatial convolution integration, thus,

$$\left(\frac{\sigma\omega^2}{D}\right)^{1/4} r \approx 0 \quad (\text{B.17})$$

The constant Green's function assumption is true when (Baeten, 1989):

- 1 the frequency of vibration and mass densities of the baseplate are low;
2. the flexural rigidity of the plate is large;

$$D \gg \sigma\omega^2 r^4, \quad (\text{B.18})$$

where σ is the mass density of the baseplate, ω is the angular frequency, and r is the baseplate radius. Since the vibrator baseplate is designed to be extremely stiff, the Green's function for displacement is approximately constant across the baseplate. This assumption is not valid for the IVI Minivib baseplate especially when driven at high frequencies (> 200 Hz). Using this assumption, equation (B.15) can be simplified (Baeten, 1989) to:

$$W(k_x, k_y) = W = -\frac{1}{8i\omega\sqrt{\sigma D}} \iint_{S^F} \{T_s(k'_x, k'_y) + P^{applied}(k'_x, k'_y)\} dk'_x dk'_y \quad (\text{B.19})$$

To approximate the ground force with the flexural rigidity baseplate model, the baseplate motion must be described in terms of acceleration. Taking the second derivative of equation (B.19) at the center of the baseplate yields (Baeten, 1989):

$$A_b^c(k_x, k_y) = -\frac{i\omega}{8\sqrt{\sigma D}} \left\{ \iint_{S^F} T_s(k'_x, k'_y) - M_r A_r \right\} \quad (\text{B.20})$$

where $A_b^c(k_x, k_y)$ is the measured acceleration at the center of the baseplate, M_r is the mass of the reaction mass, A_r is the measured acceleration of the reaction mass.

Solving for the traction underneath the baseplate in equation (B.20), the flexural rigidity method approximates the ground force signal with the expression:

$$F^G = - \iint_{S^F} T_s(k_x, k_y) dk_x dk_y = \left[\frac{8\sqrt{\sigma D}}{i\omega} A_b(k_x^c, k_y^c) - M_r A_r \right] \quad (\text{B.21})$$

where F^G is the approximated ground force, and $A_b(k_x^c, k_y^c)$ is the acceleration measured at the center of the baseplate.

Appendix C

Part 1: Additional Figures

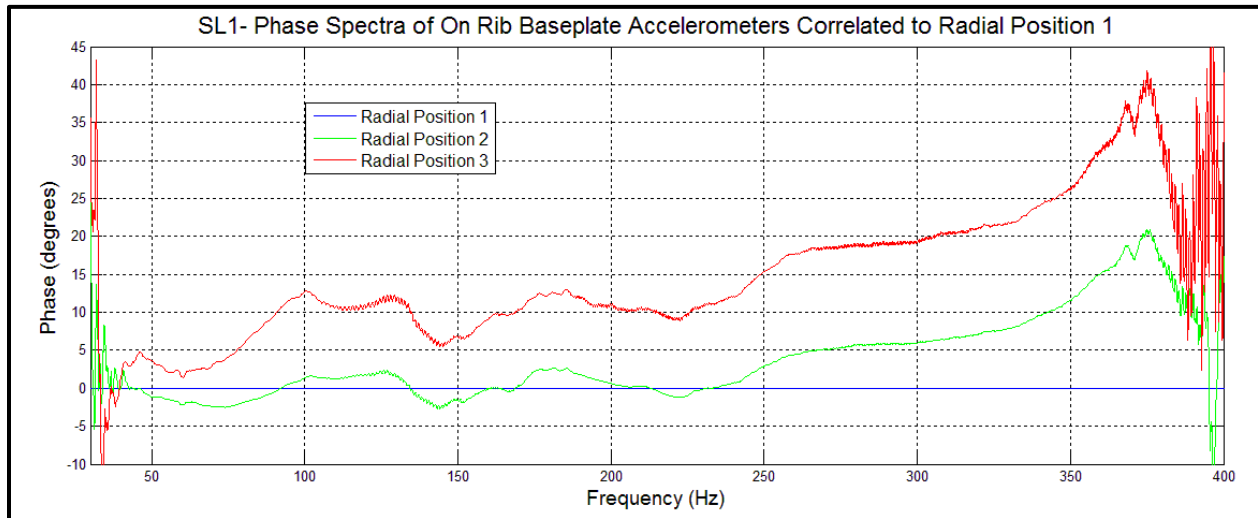


Figure C.1. Correlation phase plot of three on rib radial positions at source location 1.

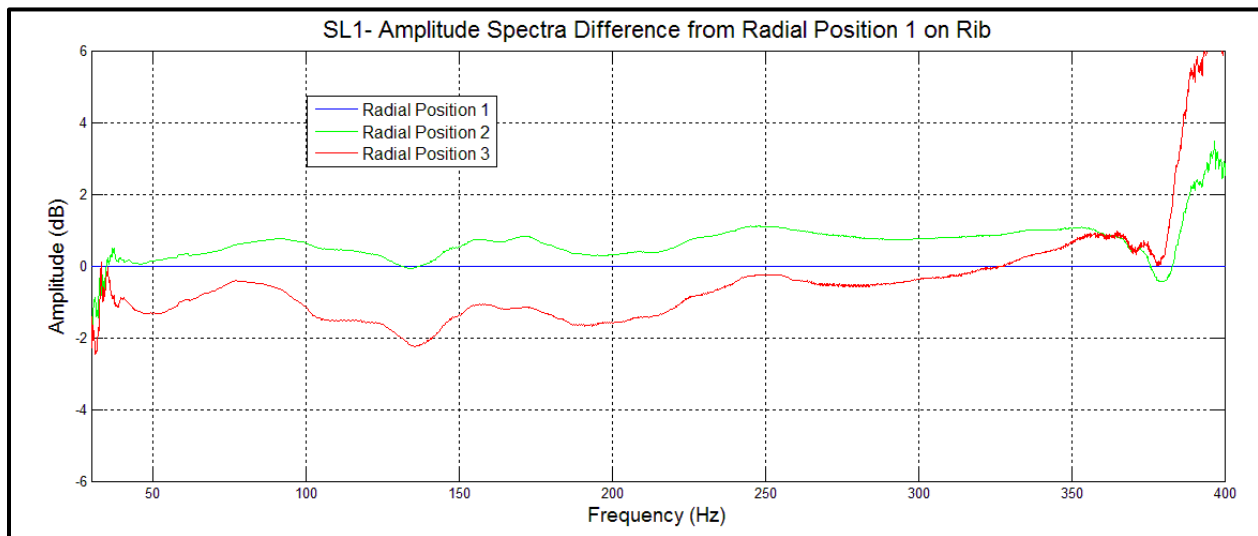


Figure C.2. Amplitude ratio of three radial positions with respect to radial position 1 located on rib reinforcement for source location 1.

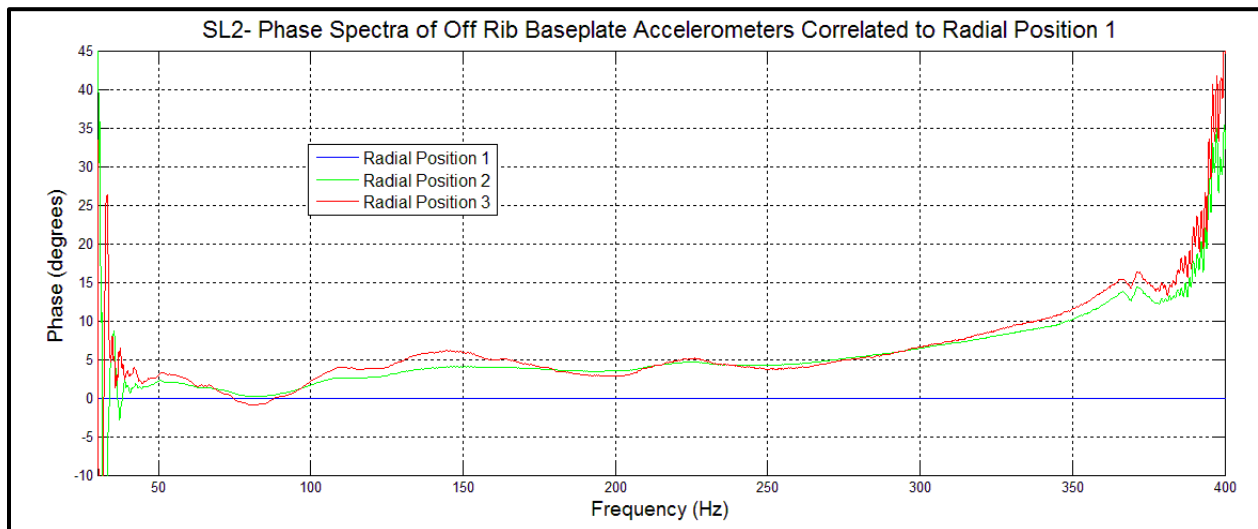


Figure C.3. Correlation phase plot of three off rib radial positions at source location 2.

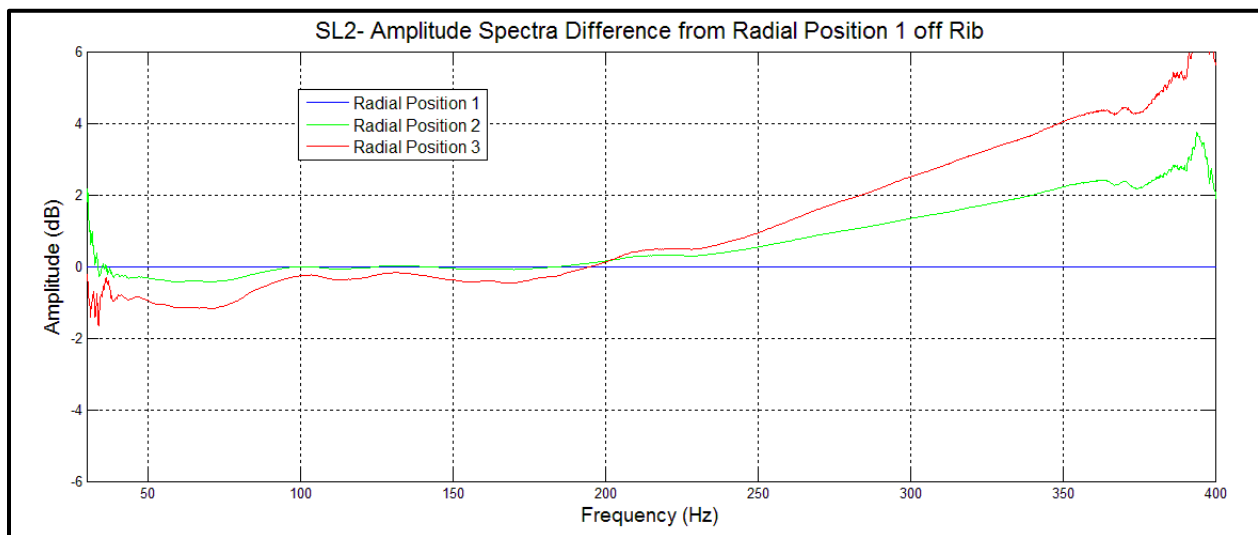


Figure C.4. Amplitude ratio of three radial positions with respect to radial position 1 located off rib reinforcement for source location 2.

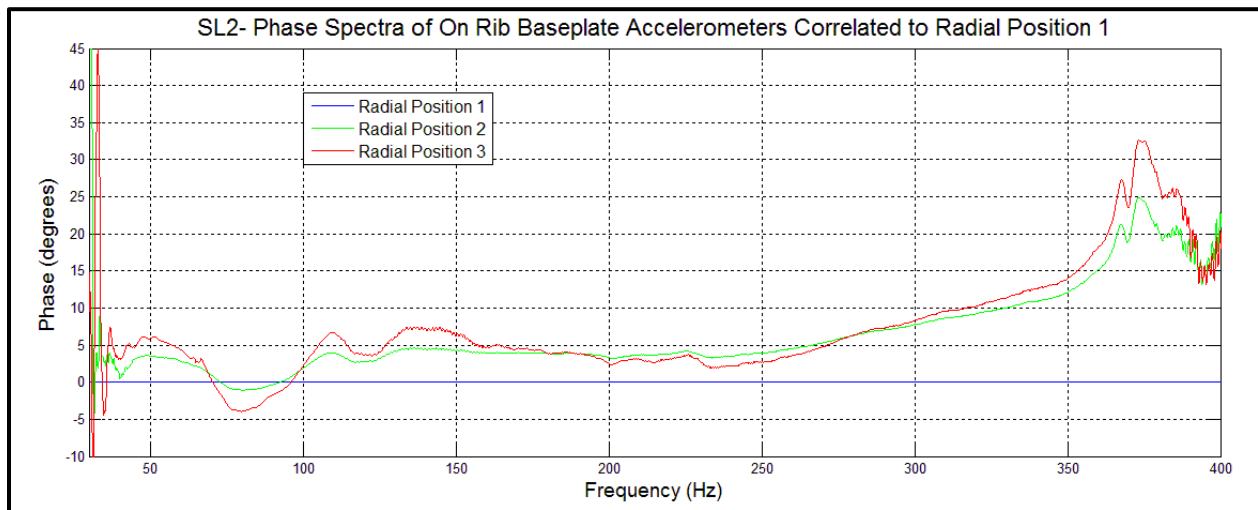


Figure C.5. Correlation phase plot of three on rib radial positions at source location 2.

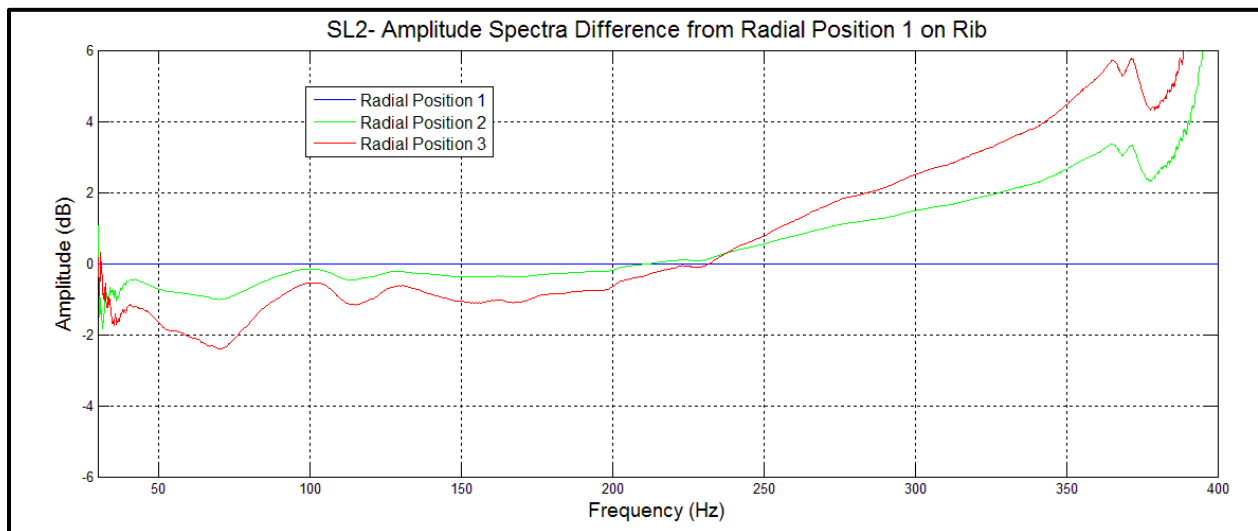


Figure C.6. Amplitude ratio of three radial positions with respect to radial position 1 located on rib reinforcement for source location 2.

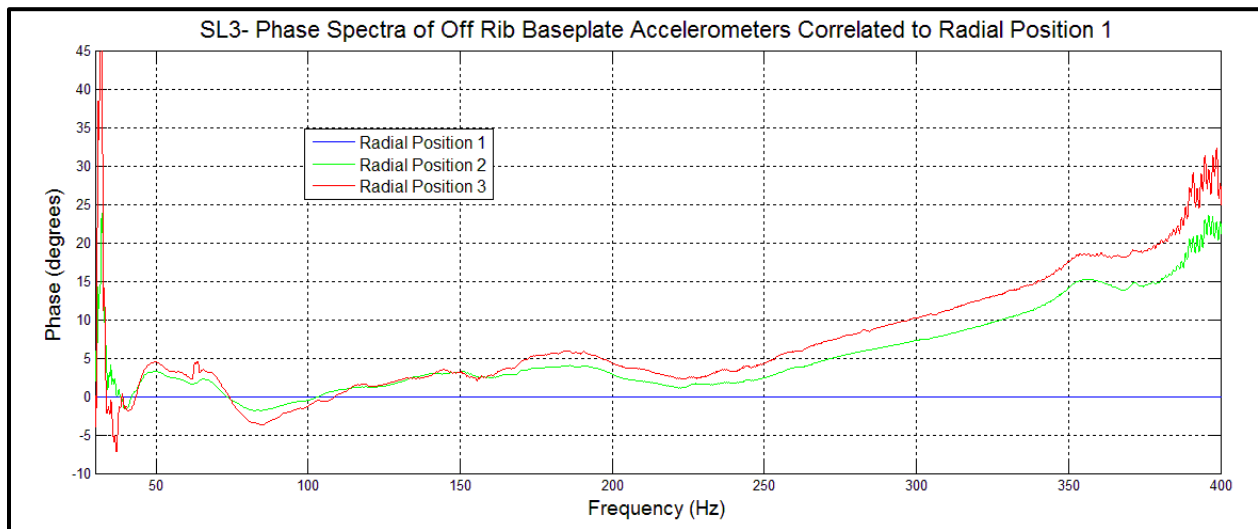


Figure C.7. Correlation phase plot of three off rib radial positions at source location 3.

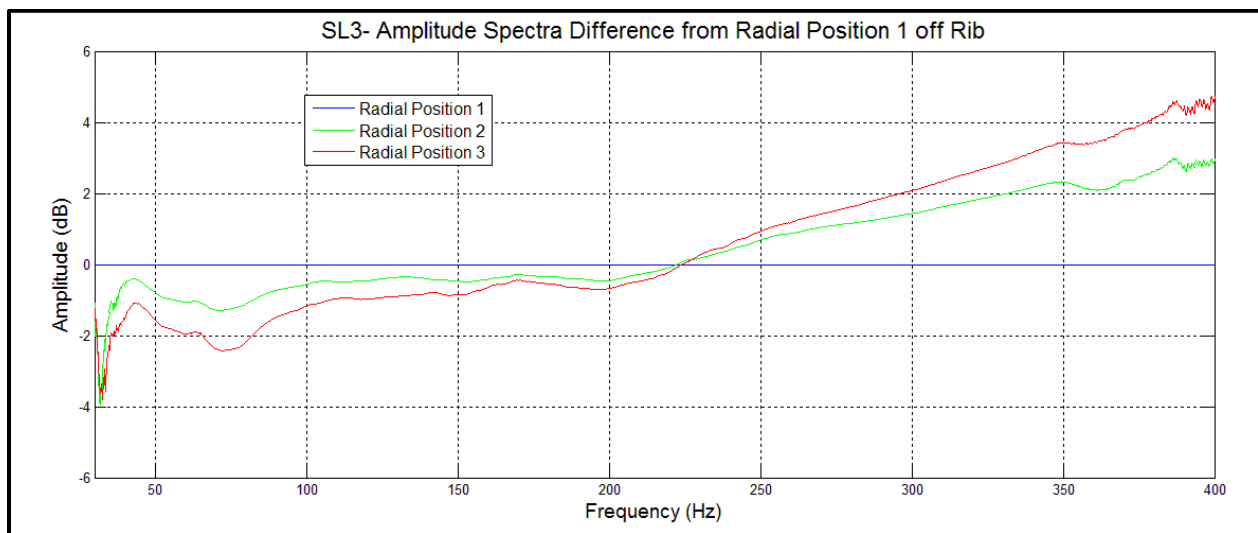


Figure C.8. Amplitude ratio of three radial positions with respect to radial position 1 located off rib reinforcement for source location 3.

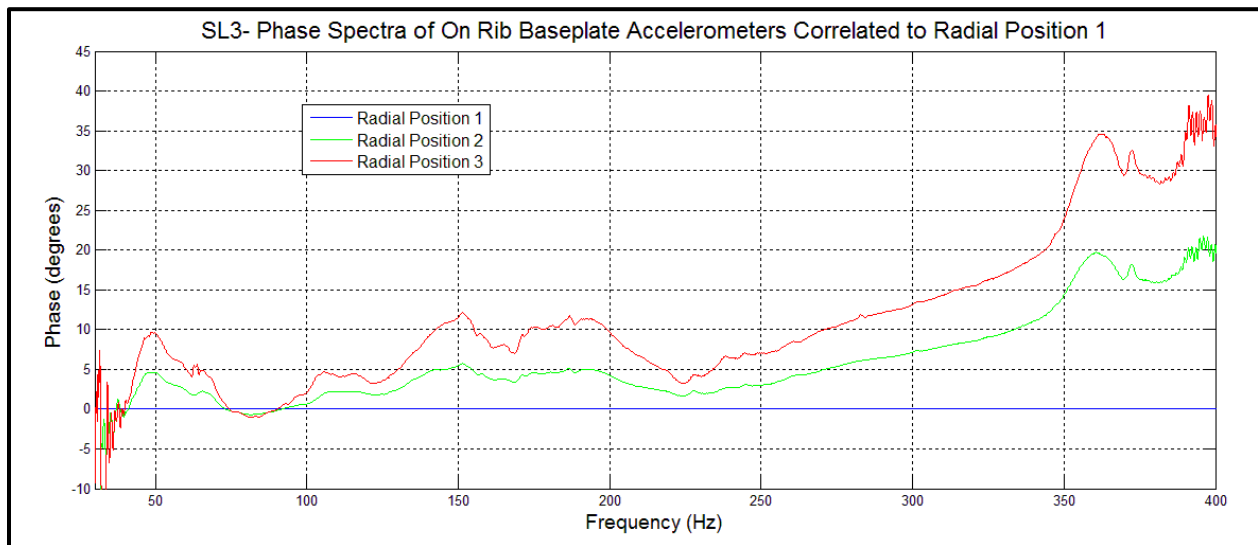


Figure C.9. Correlation phase plot of three on rib radial positions at source location 3.

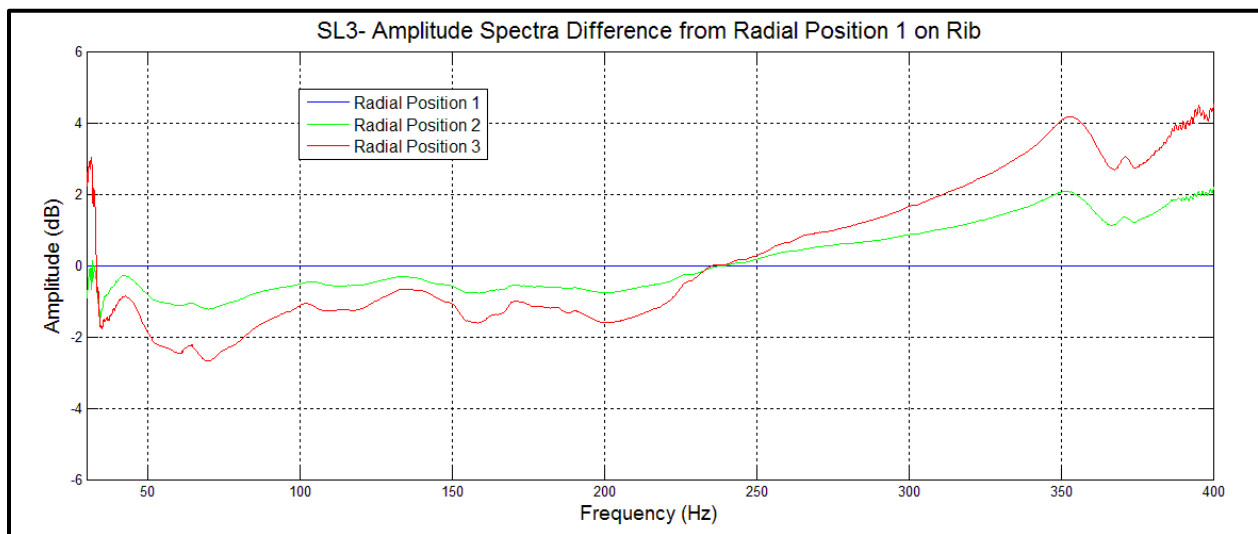


Figure C.10. Amplitude ratio of three radial positions with respect to radial position 1 located on rib reinforcement for source location 3.

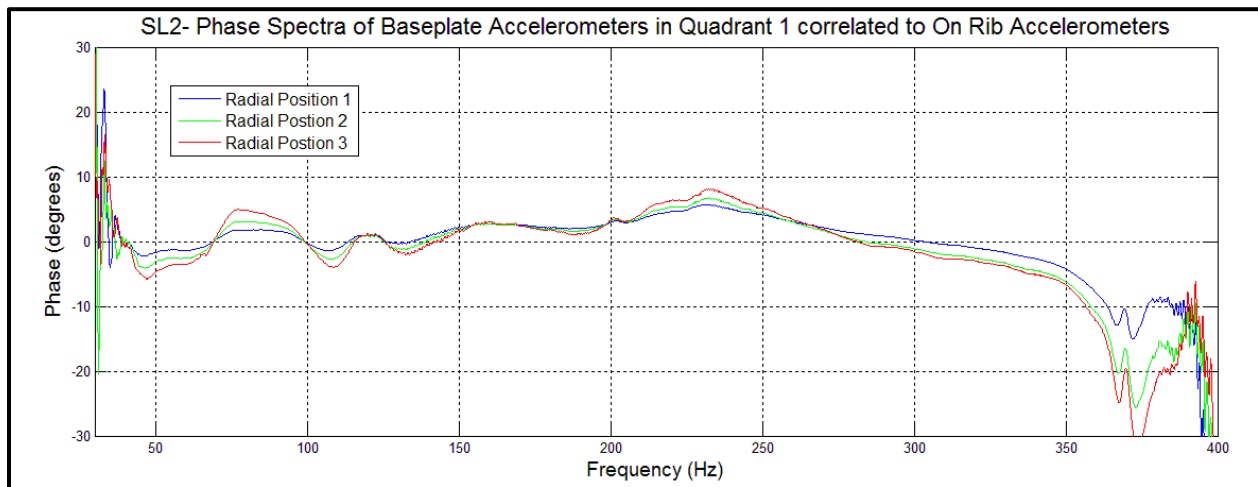


Figure C.11. Phase difference between on and off rib accelerometers for each of the three radial positions at source location 2.

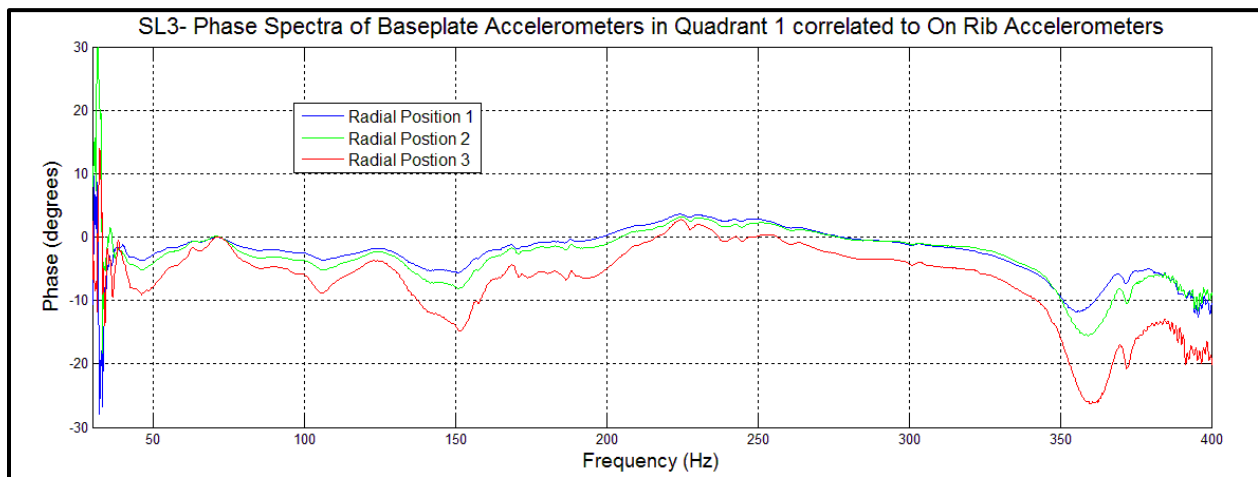


Figure C.12. Phase difference between on and off rib accelerometers for each of the three radial positions at source location 3.

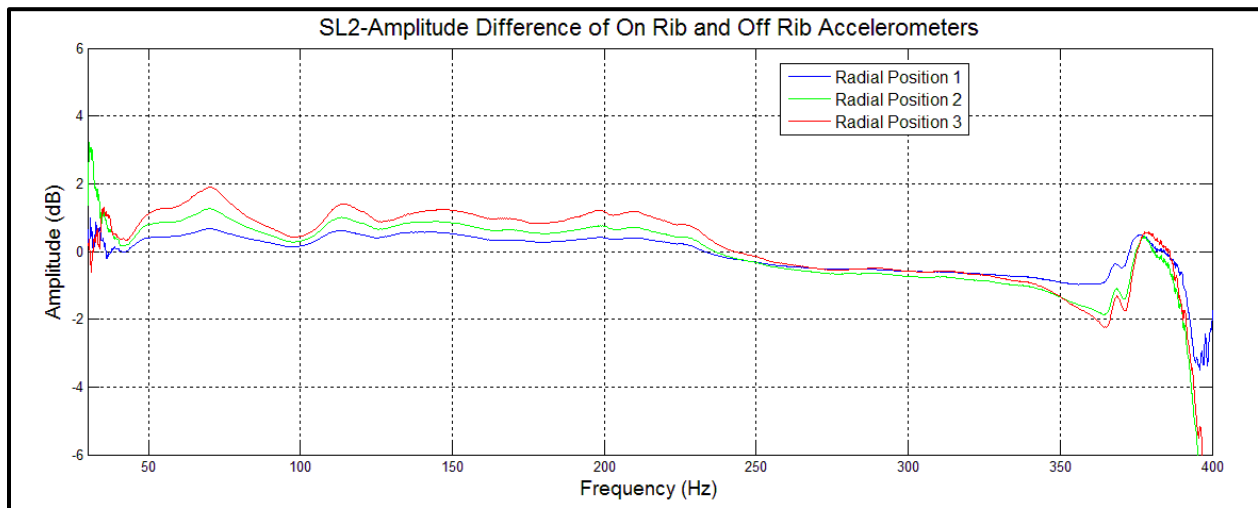


Figure C.13. Amplitude difference between on and off rib accelerometers for each of the three radial positions at source location 2 displayed in dB.

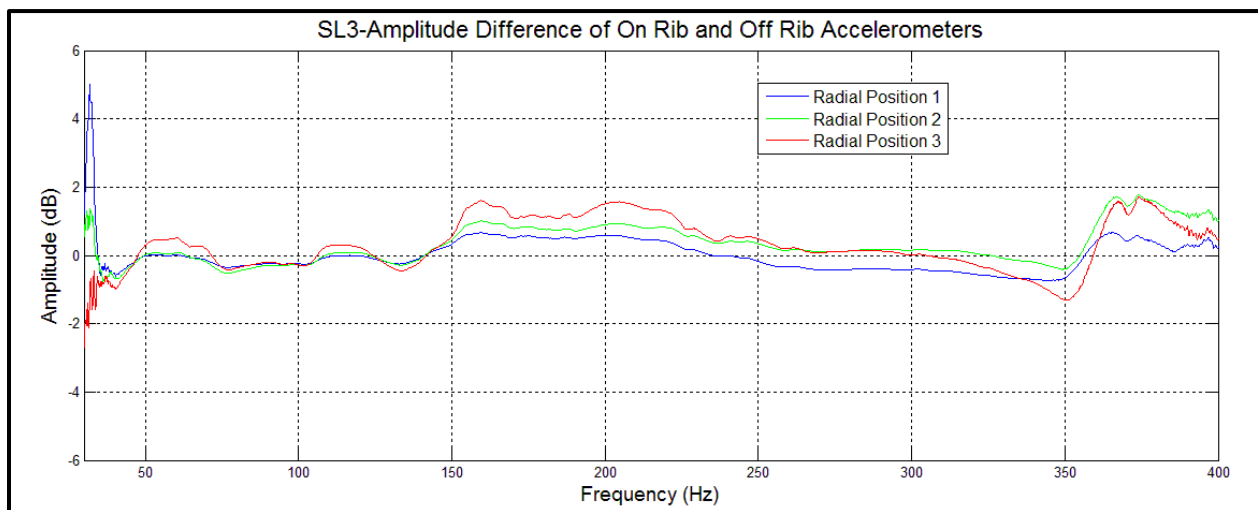


Figure C.14. Amplitude difference between on and off rib accelerometers for each of the three radial positions at source location 3 displayed in dB.

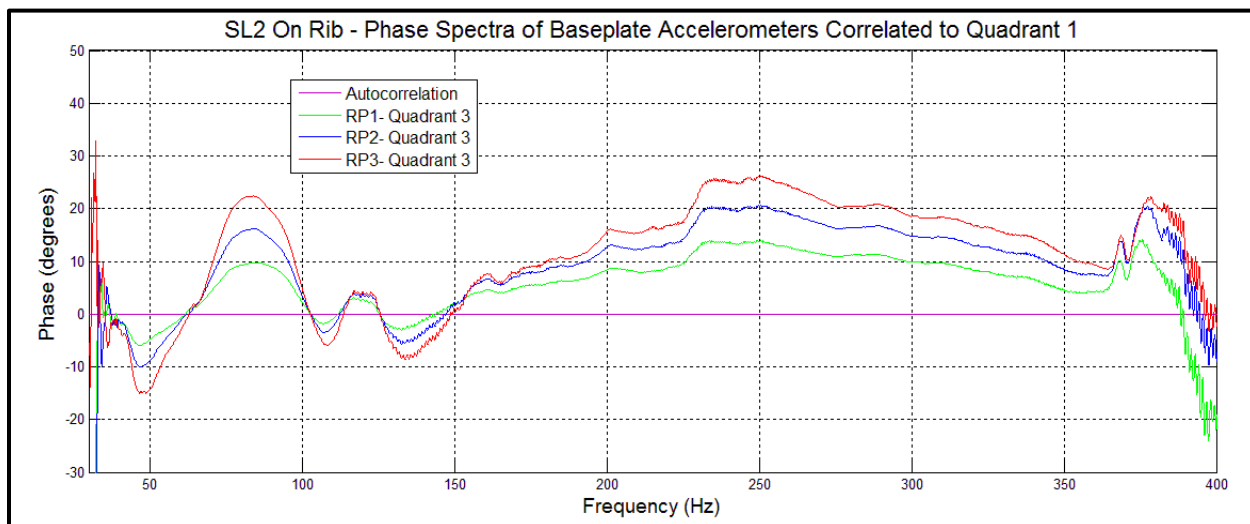


Figure C.15. Phase spectra of quadrant 3 correlated with quadrant 1 for each radial position located on rib at source location 2.

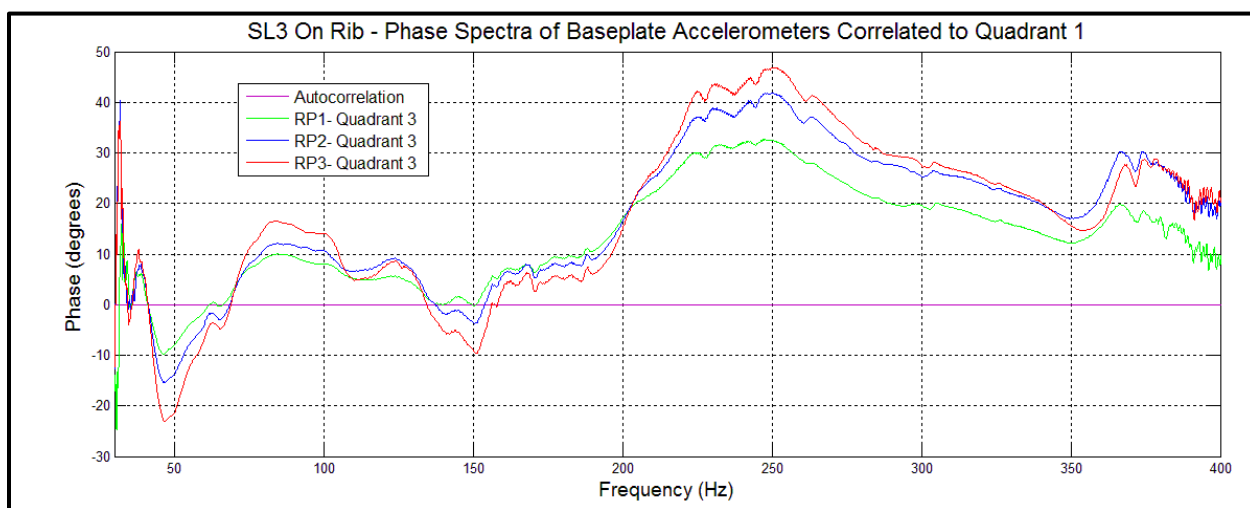


Figure C.16. Phase spectra of quadrant 3 correlated with quadrant 1 for each radial position located on rib at source location 3.

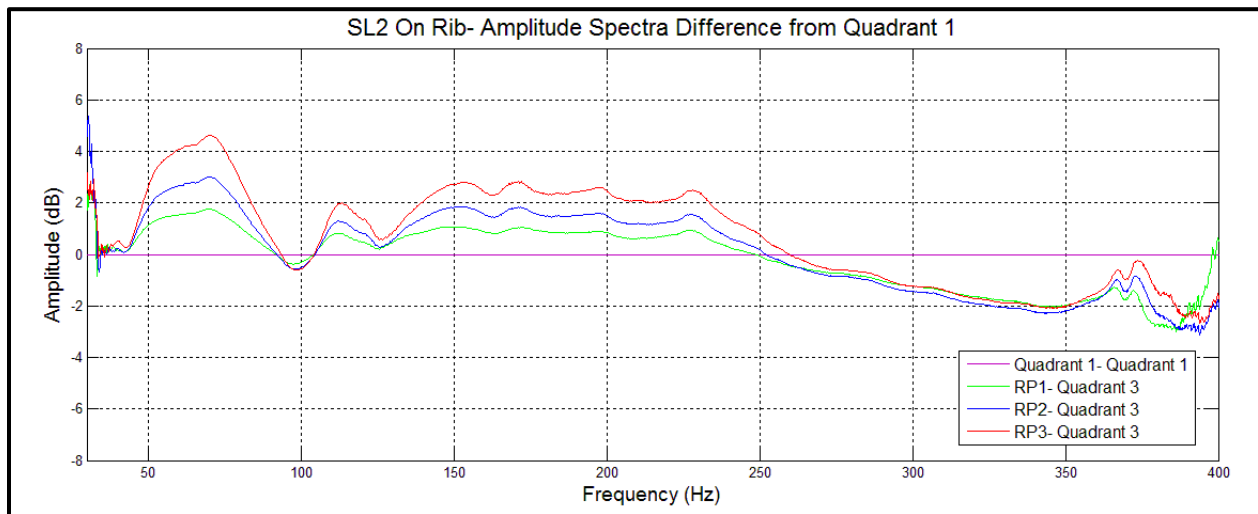


Figure C.17. Amplitude spectrum difference plot of quadrant 3 from the amplitude spectrum of quadrant 1 for each radial position located on rib at source location 2.

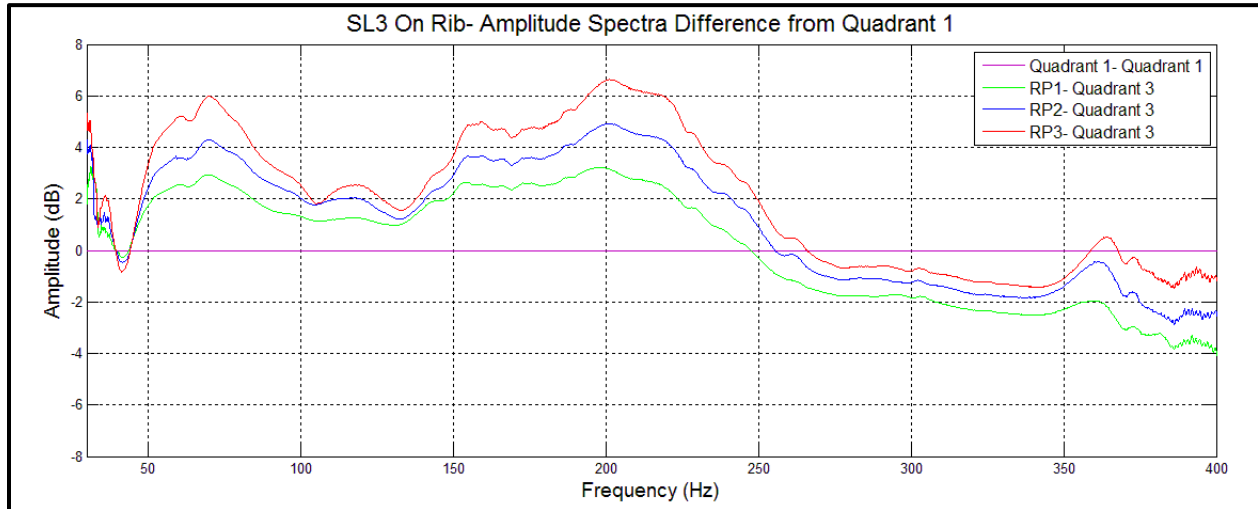


Figure C.18. Amplitude spectrum difference plot of quadrant 3 from the amplitude spectrum of quadrant 1 for each radial position located on rib at source location 3.